Oil & Natural Gas Technology

Detection and Production of Methane Hydrate

Final Report

Reporting Period: July, 2006 -December, 2011

Submitted by:
Rice University, University of Texas, and Oklahoma State University

George J. Hirasaki and Walter Chapman, Chemical and Biomolecular Engineering
Gerald R. Dickens, Colin A. Zelt, and Brandon E. Dugan, Earth Science
Kishore K. Mohanty, University of Texas
Priyank Jaiswal, Oklahoma State University

May, 2012

DOE Award No.: DE-FC26-06NT42960
John Terneus, Program Officer

Rice University – MS 362
6100 Main St.
Houston, TX 77251-1892
Phone: 713-348-5416; FAX: 713-348-5478; Email: gjh@rice.edu

Prepared for:
United States Department of Energy
National Energy Technology Laboratory

Office of Fossil Energy

Table of Contents

Disclaimer

Executive Summary

Task 5: Carbon Inputs and Outputs to Gas Hydrate Systems Accumulations

The upward flux of methane from gas hydrate systems to the seafloor is a fundamental parameter in our modeling effort. At the start of this DOE-sponsored research project, we assumed (given the literature and our initial work) that upward fluxing methane could be constrained from pore water sulfate and alkalinity profiles. We built and assessed our models accordingly. Unexpectedly, however, several articles challenged this assumption. It was virtually impossible to progress without understanding how and why interpretations of the same data diverged significantly. We have spent much of the last three years integrating, assessing and modeling pore water and sediment data from "gas hydrate" sites toward this effort. We believe that we now fully appreciate the issue. Our initial assumptions remain correct. However, such examination challenges longstanding interpretations made by the geochemical community: our modeling in this regards has opened entirely new dimensions. The basic problem (in our view) is that most workers have not considered the total impact of fermentation and advection. More specifically, the generic framework had ^{13}C-depleted methane being produced at depth but without the accompanying ^{13}C-enriched bicarbonate, and both species can migrate over time. This means that a range of DIC and $\delta^{13}C$ of DIC should occur in shallow sediment above gas hydrate systems, even if AOM is the dominant reaction for net sulfate consumption. Our initial article on this topic was published (*Dickens and Snyder*, 2009). A far more detailed view, one taking full advantage of our models, has also been published recently (*Chatterjee et al*., 2011).

Gas hydrate may have played an important role in the global carbon cycling in the past. For example, Paleocene-Eocene Thermal Maximum (PETM) which happened at 55 Ma and lasted for 200 kyrs is a big climate event during which around ~2000 GtC was injected into ocean and atmosphere environment, however, the source of carbon is a mystery, because the seafloor temperature was ~6^{o}C warmer than present-day before PETM, which should have affected the hydrate amount greatly. However, our simulation showed that, due to higher organic carbon content deposited into sediment before PETM and faster methanogenic rate, the hydrate amount could be similar to present-day value. We summarized our results in a recent publication (*Gu et al.,* 2011).

Task 6: Numerical Models for Quantification of Hydrate and Free Gas Accumulations

Gas hydrates dominated by methane naturally occur in deep marine sediment along continental margins. These compounds form in pore space where favorable conditions prevail between the seafloor and a sub-bottom depth known as the gas hydrate stability zone (GHSZ). However, the amount and distribution of gas hydrate within this zone, and free gas below, can vary significantly at different locations. To understand this variability, we develop a one-dimensional (1-D) numerical model that simulates the accumulation of gas hydrates in marine sediments due to upward and downward fluxes of methane over time. The model contains rigorous thermodynamic and component

mass balance equations that are solved using expressions for fluid flow in compacting sediments. The simulations delineate basic modes of gas hydrate distribution in marine sediment, including systems with no gas hydrate, gas hydrate without underlying free gas, and gas hydrate with underlying free gas below the GHSZ, for various methane sources. Our model presents a unified picture of hydrate accumulations that can be used to understand well-characterized gas hydrate systems or to predict steady-state average gas hydrate saturation (AGHS) and distribution at locations for which seismic or core data are not available. To test and validate our model, we have evaluated known and well characterized gas hydrate systems such as Blake Ridge (offshore south-eastern USA), Peru Margin (offshore Peru), and Costa Rica.

A direct relationship is established between the sulfate-methane transition (SMT) and AGHS using a 1-D numerical model for systems dominated by methane migration from deeper sources. Higher methane fluxes result in shallow SMT depths and high AGHS, while lower methane fluxes result in deep SMTs and low AGHS. We also develop an analytical theory to relate gas hydrate saturation in marine sediments to the depth of the SMT for systems in which methane is transported into the GHSZ from deeper external sources (i.e., advective systems). This advective constraint causes anaerobic oxidation of methane (AOM) to be the only sulfate sink, allowing us to link SMT depth to net methane flux. We evaluate our model at four drill sites along the Cascadia Margin and our calculations compare favorably with measurements from resistivity log and chloride data. This technique provides a fast and convenient method to calculate gas hydrate saturation and first-order occurrence at a given geologic setting where vertically upward advection dominates the methane flux.

The depth of the SMT above gas hydrate systems is established as a direct proxy to interpret upward methane flux and hydrate saturation. However, two competing reaction pathways can potentially form the SMT. Moreover, the pore water profiles across the SMT in shallow sediment show broad variability leading to different interpretations for how carbon, including CH_4 cycles within gas-charged sediment sequences over time. The amount and distribution of marine gas hydrate impacts the chemistry of several other dissolved pore water species such as the dissolved inorganic carbon (DIC). A 1-D numerical model is developed to account for downhole changes in pore water constituents, and transient and steady-state profiles are generated for three distinct hydrate settings. The model explains how an upward flux of CH_4 consumes most SO_4^{2-} at a shallow SMT implying that AOM is the dominant SO_4^{2-} reduction pathway, and how a large flux of ^{13}C-enriched DIC enters the SMT from depth impacting chemical changes across the SMT. Crucially, neither the concentration nor the $\delta^{13}C$ of DIC can be used to interpret the chemical reaction causing the SMT.

Existing 1-D models can provide first-order insights on hydrate occurrence, but do not capture the complexity and heterogeneity observed in natural gas hydrate systems. To incorporate lithologic heterogeneity, we develop a two-dimensional (2-D) model to simulate the accumulation of gas hydrate and free gas in heterogeneous marine sediments over geologic timescales. Systems with lithologic structures (e.g., vertical fractures, dipping sand layers) show localized, elevated hydrate and free gas

saturations within these high permeability conduits due to focused fluid flow. These simulations emphasize the importance of local, vertical, fluid flux on local hydrate accumulation and distribution. Through analysis of the fluid fluxes in 2-D systems, it is shown that a local Peclet number characterizes the local hydrate and free gas saturations, just as the Peclet number characterizes hydrate saturations in 1-D, homogeneous systems.

Effects of salinity on phase equilibrium and co-existence of hydrate and gas phases can also be investigated using these models. Formation of gas hydrate and its further dissociation to free gas changes the pore water salinity, which in turn affects the phase equilibrium of the system. Salt transport is now coupled with the existing 2-D model to track salinity changes due to hydrate formation and dissociation. A flash calculation routine has been coupled with our 2-D code to simulate conditions for co-existence of gas hydrate and free gas within the GHSZ.

Gas hydrate is often characterized in remote detection by seismic profiles and bottom-simulating reflector (BSR), which is due to an abrupt acoustic impedance contrast between the base of the GHSZ and free gas layer below. However, in some cases, hydrate is present but BSR is not observed. We demonstrate that a small fraction of heavier hydrocarbon component (e.g., 5% water-free propane) can induce a gradual transition of hydrate/free gas saturations in sediment over a significant distance relative to acoustic wavelength, causing a gradual transition of acoustic impedance. Therefore, for a multi-hydrocarbon hydrate system, the reflection response is dependent on the thickness of transition zone and seismic wavelength. This provides a possible mechanism why in some places hydrate is present but BSR is not observed.

Seismic blanking has been reported and discussed in the existing literature. Due to hydrate accumulation, the velocity in different types of sediment layers can become similar with each other. We use simple models to demonstrate that seismic blanking is not ubiquitous in hydrate systems and cannot be regarded as a key indicator for hydrate detection. Seismic wipeout due to gas chimney is more useful than blanking due to hydrate accumulation.

Overpressure often characterizes marine gas hydrate systems; that is, pore water pressure exceeds hydrostatic expectations. The effect of overpressure on gas hydrate and free gas distribution in marine sediments is studied using a 1-D numerical model that couples sedimentation, fluid flow, and gas hydrate formation. We also assess stability in gas hydrate bearing sediment using an infinite slope stability analysis coupled with our geologic accumulation models (collaboration with Task 8). This technique is computationally inexpensive, applicable in geologic and reservoir models, and provides a quick look at stability to identify locations for detailed stability analysis.

Task 7: Analysis of Production Strategy

We participated in the NETL methane hydrate code comparison study (CCS) to evaluate the capabilities of the in-house (University of Houston) simulator with respect to other existing hydrate simulators. We used our in-house hydrate simulator and

completed simulations on the first four problems set up by the CCS group. Our results have been communicated to Prof. Brian Anderson, the coordinator of the CCS group.

Experimental data on multiphase flow properties of gas hydrate containing sediments is rarely available. Empirical correlations are often used for transport properties of sediments containing gas hydrates. We have developed mechanistic models for transport properties for hydrate bearing sediments. Hydrate deposition and dissociation is modeled in a single pore to develop pore-scale laws of hydrate occupancy. Pore size distributions are found for sediments containing different particle size distributions. Pore size distribution is modified due to hydrate deposition. Percolation theory is used to numerically calculate effective transport properties at different hydrate and water saturations. The transport properties calculated from these mechanistic models can replace the empirical correlations in reservoir simulations of hydrate reservoirs.

Gas production from a hydrate reservoir is studied through numerical simulation. We consider two strategies for production from confined Class 2 hydrate reservoirs: warm water injection and depressurization. The source of warm water could be a nearby oil reservoir or an underlying water aquifer. We consider reservoirs with a limited aquifer. We assume that the aquifer is unconfined not at the bottom but on one side of the aquifer. For the limited aquifer case, we study only horizontal wells, and that makes the reservoir translationally symmetric. In this study, the reservoir is simulated in two-dimensions keeping the total hydrate amount, hydrate to water ratio, initial conditions and the rock properties the same as in our unconfined reservoir base case simulations.

In earlier work, we had assumed that the hydrate reservoirs are homogeneous. In this study, we assume hydrate layers of different initial hydrate saturation and permeability. Warm water flooding is simulated and the gas production is computed.

We have shown that depressurization is ineffective in unconfined reservoirs; warm water injection is effective and horizontal wells are more effective than vertical wells. In this study, we consider CO_2 injection into methane hydrate reservoirs to release methane and sequester CO_2.

Task 8: Seafloor and Borehole Stability

To assess the seafloor and borehole stability, we completed three integrated subtasks that allowed us to use numerical models, laboratory data and experiments, logging and geophysical data, and field data. The three subtasks completed were: Subtask 8.1 – Sediment hydrate properties; Subtask 8.2 – Modeling (In)Stability; and Subtask 8.3 – Data Integration and Collaboration. The primary scientific accomplishments were the development of models on heterogeneous hydrate accumulation including fracture hosted hydrate in clays, the time-frames and mechanics of fracture genesis, and the preference for systems to allow fracture-dominated failure and hydrate accumulation over large-scale slope instability. This first order insight may help explain why hydrate-related slope failures are hard to find in nature – the fracturing process may release pressure prior to large-scale failure. Future research will continue to look at scenarios that generate large failure and/or systems that are primed for failure due to hydrates.

These model studies (Subtask 8.2) were largely fed through the collaboration and data gathering that occurred through Subtasks 8.1 and 8.2. We have published peer-reviewed papers and given national and international presentations on each subtask (see Publications and Presentations).

Task 9 Geophysical Imaging of Gas Hydrate and Free Gas Accumulations

We primarily focused on developing traveltime and waveform based method for detection of gas hydrate and a rock physics model for quantification of gas hydrate in fractured media.

1. Seismic data that is being used for Task 9 comes from Krishna-Godavari (K-G) Basin in the Indian east coast. The well data were collected during the NGHP drilling expedition in 2005. The PI is successfully collaborating with National Institute of Oceanography (NIO), India.

2. Prior to applying our imaging methodology we interpret existing seismic sections to obtain a generic idea about geo-thermal gradient, fault patterns, and BSR structure.

3. Subtask 9.1 involves preliminary processing and traveltime inversion of the data were accomplishes. A pre-stack depth migrated image is generated using velocity model from composite inversion/migration that agreed very well with the sonic log suggesting that the velocity model and the depth image were geologically accurate.

4. Subtask 9.2 involved 2-D acoustic and 1-D elastic waveform inversion. We realized that with the currently dataset was not suited for 1-D elastic inversion. Finally we performed 2D visco-elastic inversion.

5. Subtask 9.3 involves development of rock physics model for quantification of gas hydrate in fractured media. This work is done is association with Jack Dvorkin of Stanford University.

Background

A. Objective

This project seeks to understand regional differences in gas hydrate systems from the perspective of as an energy resource, geohazard, and long-term climate influence. Specifically, the effort will: (1) collect data and conceptual models that targets causes of gas hydrate variance, (2) construct numerical models that explain and predict regional-scale gas hydrate differences in 2-dimensions with minimal "free parameters", (3) simulate hydrocarbon production from various gas hydrate systems to establish promising resource characteristics, (4) perturb different gas hydrate systems to assess potential impacts of hot fluids on seafloor stability and well stability, and (5) develop geophysical approaches that enable remote quantification of gas hydrate heterogeneities so that they can be characterized with minimal costly drilling. Our integrated program takes advantage of the fact that we have a close working team comprised of experts in distinct disciplines.

The expected outcomes of this project are improved exploration and production technology for production of natural gas from methane hydrates and improved safety through understanding of seafloor and well bore stability in the presence of hydrates.

B. Scope of Work

The scope of this project was to more fully characterize, understand, and appreciate fundamental differences in the amount and distribution of gas hydrate and how this would affect the production potential of a hydrate accumulation in the marine environment. The effort combines existing information from locations in the ocean that are dominated by low permeability sediments with small amounts of high permeability sediments, one permafrost location where extensive hydrates exist in reservoir quality rocks and other locations deemed by mutual agreement of DOE and Rice to be appropriate. The initial ocean locations were Blake Ridge, Hydrate Ridge, Peru Margin and GOM. The permafrost location was Mallik. Although the ultimate goal of the project was to understand processes that control production potential of hydrates in marine settings, Mallik was included because of the extensive data collected in a producible hydrate accumulation. To date, such a location had not been studied in the oceanic environment. The project worked closely with ongoing projects (e.g. GOM JIP and offshore India) that are actively investigating potentially economic hydrate accumulations in marine settings.

The overall approach was fivefold: (1) collect key data concerning hydrocarbon fluxes which is currently missing at all locations to be included in the study, (2) use this and existing data to build numerical models that can explain gas hydrate variance at all four locations, (3) simulate how natural gas could be produced from each location with different production strategies, (4) collect new sediment property data at these locations that are required for constraining fluxes, production simulations and assessing sediment stability, and (5) develop a method for remotely quantifying heterogeneities in gas hydrate and free gas distributions. While we generally restricted our efforts to the locations where key parameters can be measured or constrained, our ultimate aim was to make our efforts universally applicable to any hydrate accumulation.

Task 5: Carbon Inputs and Outputs to Gas Hydrate Systems

The upward flux of methane from gas hydrate systems to the seafloor is a fundamental parameter in our modeling effort. At the start of this DOE-sponsored research project, we assumed, given the literature and our initial work (*Snyder et al*., 2007), that upward fluxing methane could be constrained from pore water sulfate and alkalinity profiles. We built and assessed our models accordingly (*Bhatnagar et al*., 2008). Unexpectedly, however, several articles (e.g., *Kastner et al*., 2008) challenged this assumption.

It was virtually impossible to progress without understanding how and why interpretations of the same data diverged significantly. We have spent much of the last three years integrating, assessing and modeling pore water and sediment data from "gas hydrate" sites toward this effort. We believe that we now fully appreciate the issue. Our initial assumptions remain correct. However, such examination challenges longstanding interpretations made by the geochemical community: our modeling in this regards has opened entirely new dimensions. The basic problem (in our view) is that most workers have not considered the total impact of fermentation and advection. More specifically, the generic framework had ^{13}C-depleted methane being produced at depth but without the accompanying ^{13}C-enriched bicarbonate, and both species can migrate over time. This means that a range of DIC and $\delta^{13}C$ of DIC should occur in shallow sediment above gas hydrate systems, even if AOM is the dominate reaction for net sulfate consumption. Our initial article on this topic was published (*Dickens and Snyder*, 2009). A far more detailed view, one taking full advantage of our models, has also been published recently (*Chatterjee et al*., 2011).

Subtask 5.3. Amount of carbon in hydrate systems and its role in natural carbon cycling (Guangsheng Gu)

We finished and published a paper on Nature Geoscience (*Gu et al.,* 2011). We also completed the study on carbon content and reaction rate constant model affecting hydrate abundance. This work is reported in the semi-annual report NT42960R16.

Task 6: Numerical Models for Quantification of Hydrate and Free Gas Accumulations

Subtask 6.1: Model development (Gaurav Bhatnagar) **AND**

Subtask 6.2: Conditions for existence of gas hydrate (Gaurav Bhatnagar)

Gas hydrates dominated by methane naturally occur in deep marine sediment along continental margins. These compounds form in pore space between the seafloor and a sub-bottom depth where appropriate stability conditions prevail. However, the amount and distribution of gas hydrate within this zone, and free gas below, can vary significantly at different locations. To understand this variability, we develop a one-dimensional numerical model that simulates the accumulation of gas hydrates in marine sediments due to upward and downward fluxes of methane over time. The model contains rigorous thermodynamic and component mass balance equations that are solved using expressions for fluid flow in compacting sediments. The effect of salinity on gas hydrate distribution is also included. The simulations delineate basic modes of gas hydrate distribution in marine sediment, including systems with no gas hydrate, gas hydrate without underlying free gas, and gas hydrate with underlying free gas below the gas hydrate stability zone, for various methane sources. The results are scaled using combinations of dimensionless variables, particularly the Peclet number and Damkohler number, such that the dependence of average hydrate saturation on numerous parameters can be summarized using two contour maps, one for a biogenic source and one for upward flux from a deeper source. Simulations also predict that for systems at steady state, large differences in parameters like seafloor depth, seafloor temperature and geothermal gradient cause only small differences in average hydrate saturation when examined with scaled variables, although important caveats exist. Our model presents a unified picture of hydrate accumulations that can be used to understand well-characterized gas hydrate systems or to predict steady-state average hydrate saturation and distribution at locations for which seismic or core data are not available.

Models for quantifying methane hydrate saturation in marine sediment have previously been developed for specific locations and are valid only for the numerous parameters characteristic of these sites. We use results from a one-dimensional numerical model with dimensionless scalings to generate an average gas hydrate saturation plot that is valid over a wide range of transport parameters. This single contour plot suffices in explaining different gas hydrate distributions resulting from methane generated via in-situ methanogenic reactions. The contour plot is also relatively insensitive to changes in seafloor properties (like seafloor depth, bottom water temperature and geothermal gradient), making it applicable to different geologic settings. To test and validate our model, we have evaluated where known and well characterized gas hydrate systems such as Blake Ridge (offshore south-eastern USA), Peru Margin (offshore Peru), and Costa Rica Margin lie on this simulated saturation plot. Average gas hydrate saturations at these locations are predicted to be about 1.5%,

4% and <1%, respectively, which are in agreement with values inferred from proxy data or other numerical models.

Effect of methane supplied from deeper sources, in addition to in-situ generated methane, is also discussed through specific simulations. A possible mechanism for the heterogeneous distribution at Blake Ridge (Ocean Drilling Program Leg 164), with no hydrate/free gas contact at Site 994 and gas hydrate/free gas contact at the BSR at Sites 995/997, is explained by incorporating mixed methane sources in the simulations. General behavior of systems with in-situ biogenic as well as mixed sources of methane in response to changes in transport parameters is also discussed. Finally, conditions suitable for high average gas hydrate saturations for both systems are stated.

Subtask 6.3: Compositional effect on BSR (Guangsheng Gu)

Gas hydrate is often characterized in remote detection by seismic profiles and Bottom-Simulating Reflector (BSR), which is due to an abrupt acoustic impedance contrast between the base of gas hydrate stability zone (GHSZ) and free gas layer below. However, in some cases, hydrate is present but BSR is not observed. In this work, we demonstrate that a small fraction of heavier hydrocarbon component can induce a gradual transition of hydrate/free gas saturations in sediment over a significant distance relative to acoustic wavelength. If the thermogenic gas source from deeper sediment contains 5% (mol/mol) propane, a transition zone as thick as ~130 m can be formed, in which hydrate, gas, and aqueous phases can co-exist. The saturations of each phase change gradually, causing a gradual transition of acoustic impedance. Seismic waves with different dominant wavelengths are tested to generate synthetic seismic responses. Results show that, if the ratio of thickness of transition zone to the dominant wavelength (thickness ratio L_{stz}/λ) is larger than 0.5, then the reflection is very weak; if the ratio is much lower than 0.5, the reflection is very strong. This indicates that in the case of a multi-hydrocarbon hydrate system, the reflection response is dependent on the thickness of transition zone and seismic wavelength. This provides a possible mechanism why in some places hydrate is present but BSR is not observed.

Extensive research on gas hydrate has been done on gas hydrate distribution. However, most of them are discussing and thinking about pure methane hydrate system in natural marine sediments. In such a system, gas hydrate is often characterized in seismic detection by a special indicator known as a Bottom-Simulating Reflector (BSR), a strong reflector under seafloor, which is due to an abrupt acoustic impedance contrast between the base of gas hydrate stability zone (GHSZ) and free gas layer below. At current stage, the BSR is one of the key major signs in remote detection of hydrate. However, BSR is not a reliable sign for hydrate existence. In some cases, hydrate is present but BSR is not observed; while in other cases, BSR is due to carbonate deposit etc.

However, this scenario is mainly for pure-methane hydrate system. The effect of other gas components on hydrate distribution is not deeply considered. Here we report a study on a methane-propane hydrate system in which the hydrate distribution and seismic response are greatly affected by a small fraction of propane.

Natural gas from thermogenic sources may contain many hydrocarbon components other than methane (Sloan, 2007; C. Hadley, 2008; D. Shelander, 2009). Thus compositional effect should be considered when thermogenic natural gas is present. Here we focus on the CH_4-C_3H_8-H_2O hydrate system as an example. The effects of propane on the hydrate formation condition and on hydrate distribution are studied.

Phase Diagram

Assuming zero salinity, in P-T space, according to Gibbs phase rule, the degree of freedom of an equilibrium multi-phase system is:

$$F = C - P + 2 \qquad (1)$$

where F, C, and P are degree of freedom, number of components, number of co-existing phases, respectively. In the pure methane hydrate system, consider a 3-phase equilibrium condition, C = 2, P = 3, so F = 1, therefore the 3-phase equilibrium boundary is a single-valued curve. However, if one more gas component is included, C = 3, so F = 2. There are two important consequences.

Firstly, the 3-phase equilibrium boundary is not a single curve, but a family of curves. Phase diagrams of a pure methane hydrate system (Figure 1) and a system with both methane and propane (Figure 2 and 3) are shown below, assuming zero salinity. In Figure 2, the 3-phase equilibrium curves were shown marked with the water-free propane molar fractions. Denote the overall molar fraction of species i as:

$$x_i = \frac{n_i}{n_{CH4} + n_{C3H8} + n_{H2O}},\ i = CH_4,\ C_3H_8,\ H_2O \qquad (2)$$

where n_i is the amount of species i in the system (unit: mol), i = CH_4, C_3H_8, H_2O. The water free molar fraction of species i is denoted as:

$$x_i^{wf} = \frac{n_i}{n_{CH4} + n_{C3H8}} = \frac{x_i}{x_{CH4} + x_{C3H8}},\ i = C\,H_4,\ C_3H_8 \qquad (3)$$

The figure indicates that: (1) A small fraction of propane can induce a big change of 3-phase equilibrium boundary, i.e., the incipient formation pressure of hydrate. For example, at 276.15K, the incipient hydrate formation pressure in pure methane hydrate system is 3.49 MPa (sI hydrate), while that for a system with 1% propane is only 1.71 MPa (sII hydrate). (2) The higher the fraction of propane is, the lower the incipient formation pressure will be, and the bigger difference is between a methane-propane hydrate system and a pure methane hydrate system.

Secondly, in the methane-propane hydrate system, the P-T space will be divided into 3 regions. Figure 3 presents the phase regions of the CH_4-C_3H_8-H_2O System (set x_{C3H8}^{wf} = 0.05). In Region A, both sI and sII hydrates are stable, while in Region B and C, sI is

unstable. In Region B, sII is stable, while in Region C, it isn't. Therefore, in Region B, 3 phases can co-exist: Aq, H, and V.

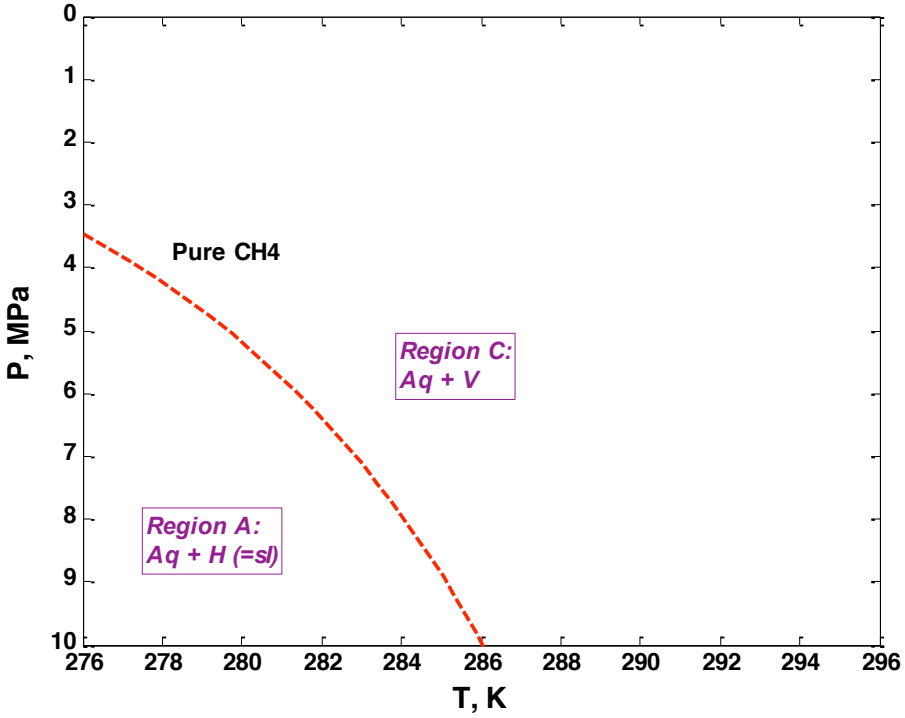

Figure 1. Pure methane hydrate phase diagram in P-T space

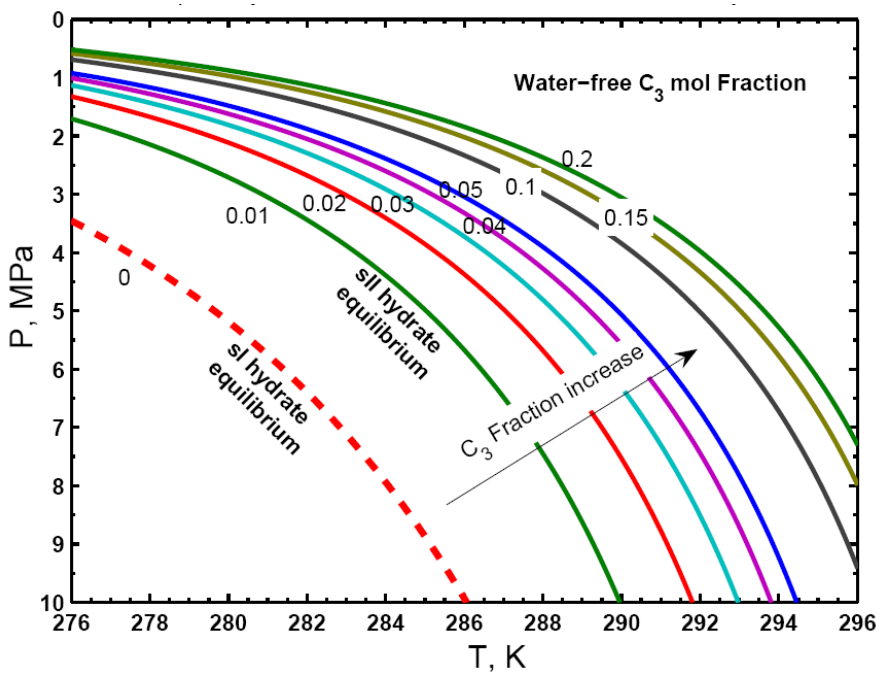

Figure 2. The Incipient Hydrate Formation Pressure of a CH_4-C_3H_8-H_2O System

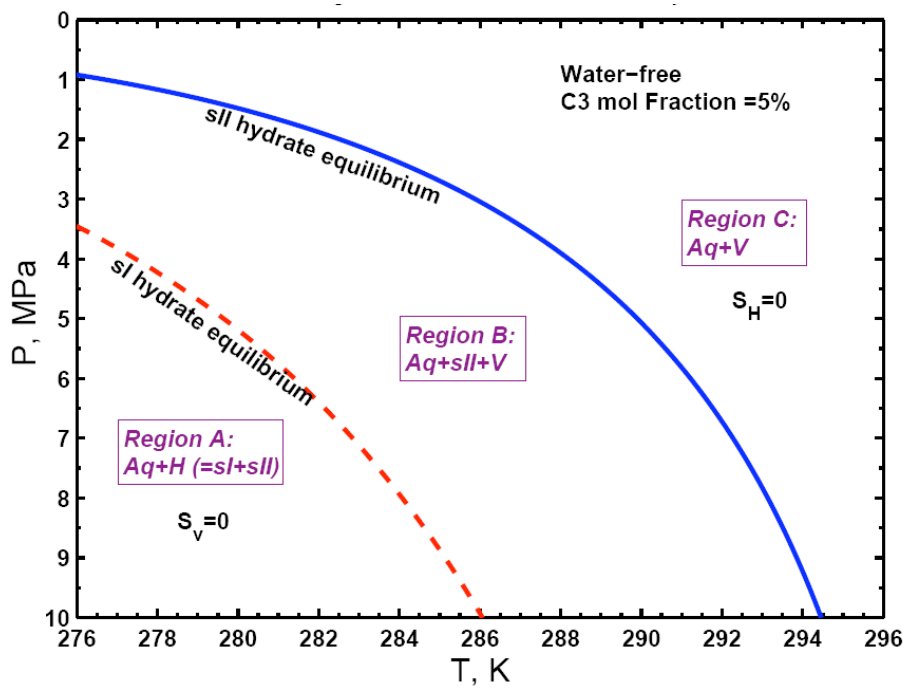

Figure 3. Phase Regions in a CH_4-C_3H_8-H_2O System

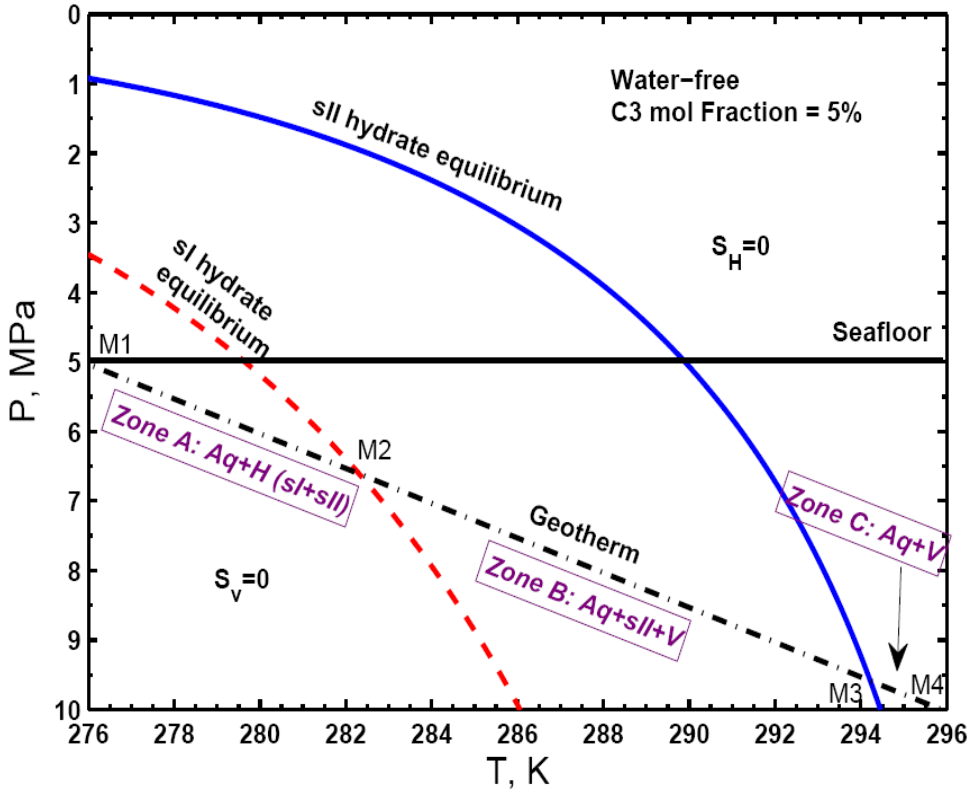

Figure 4. Sediment Zones in a CH_4-C_3H_8-H_2O System (an typical example)

In Figure 4, an example geothermal curve in sediment is considered. Three different zones may exist in the sediment along the geothermal curve, due to the 3 different phase regions described in Figure 3. Zone *B* is a special one: 3 phases, *Aq + H (sII) +V*, co-exist. The boundary for S_v=0 in the sediment is the point M_2 in Figure 4, while that for S_H=0 is the point M_3. It's obvious that Zone B (Line segment M_2M_3) is a phase-transition-zone corresponding to the boundary of S_v=0 to that of S_H=0. Line segment M_2M_3 in Figure 4, around 300 m in spatial distance, is longer than the thickness of gas hydrate stability zone (GHSZ).

To show how this will affect the hydrate/free gas distribution, hydrate / free gas saturation profiles have been calculated using a set of typical conditions. The following conditions and assumptions are applied: (1) Water-free propane molar fraction is 0.05. (2) Overall composition x_{CH4}=0.019, x_{C3H8}=0.001, x_{H2O}=0.98. Overall composition is constant in the spatial domain. (3) Seafloor temperature T_{sf} = 276.15 K. Geothermal gradient G= 0.04 K/m. (4) Seafloor Pressure P_{sf}=5.0 MPa. The results are obtained by using CSMGem v1.0 (Koh and Sloan, 2008), and are presented in Figure 5.

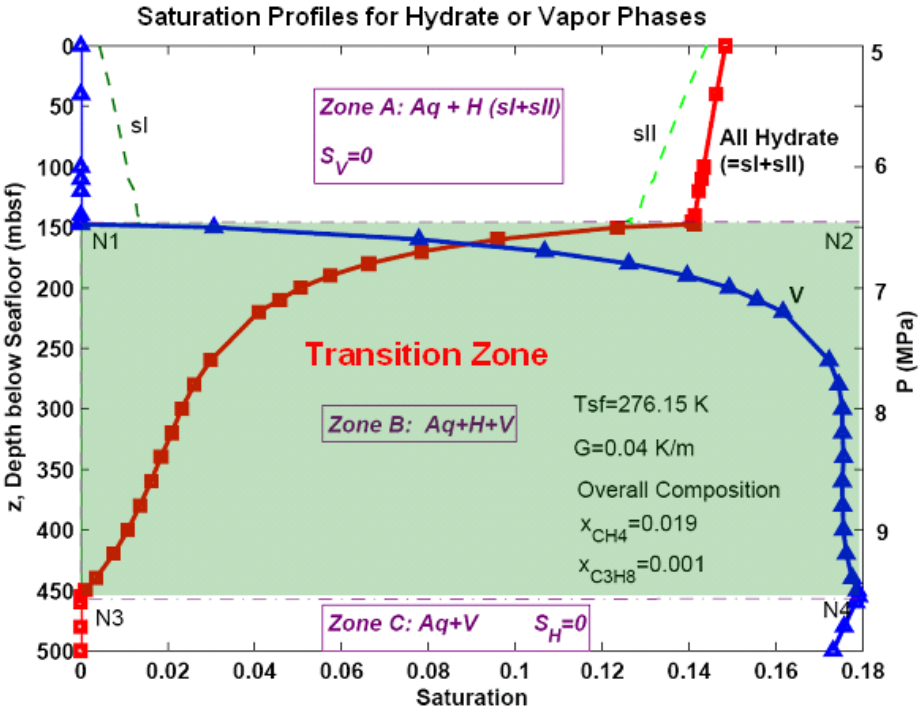

Figure 5. An example of the CH_4-C_3H_8-H_2O System (water-free propane molar fraction is 0.05; Overall composition x_{CH4}=0.019, x_{C3H8}=0.001, x_{H2O}=0.98). Assume: The overall composition is the same in the spatial domain. There are 3 zones of sediments in the domain. Zone A: *Aq + Hydrate* (= *sI + sII*); Zone B: *Aq + sII + V*; Zone C: *Aq + V*. Dash-dot line *AB* and *CD*, are boundaries for S_v=0 and S_H=0 in the sediment, respectively. Red solid curve and blue solid curve are saturation profiles for All Hydrate (=sI + sII), and for Vapor, respectively. Seafloor temperature T_{sf} = 276.15 K. Geothermal gradient G= 0.04 K/m. Pressure is marked on the right side.

Such a gradual change of saturations within a long spatial distance, may result in gradual change of sediment acoustic properties, and further induce weak BSR or even absence of BSR. So synthetic seismic response was also generated.

Acoustic Properties and Synthetic Seismic Response

In the previous section, the saturation profiles were calculated for a typical example system. Its acoustic property profiles containing hydrate/free gas are shown in Figure 4. The normalized density varies slightly from seafloor (at 150 mbsf) to deeper sediment till 500 mbsf, therefore it's not the major factor for acoustic impedance change. However, the normalized compressive velocity varies much, and thus the normalized acoustic impedance varies much too, due to this variation. The variation of acoustic impedance can be divided into two parts. One part, named as the steep transition zone (STZ), defined by the thickness in which 99% of impedance variation has been achieved, whose thickness is denoted as L_{stz} ~ 130 m, is a part which induces a more obvious seismic reflection than the second part; the second part is the rest of the transition zone, which is not as steep as the steep transition zone, and the seismic reflection due to this part is almost negligible for a typical range of seismic frequencies.

Average acoustic velocities are calculated via Time-average Equation (Pearson et al., 1983):

$$\frac{1}{V_p} = \frac{\phi(1 - S_h - S_g)}{V_{Aq}} + \frac{\phi S_h}{V_h} + \frac{(1-\phi)}{V_m} + \frac{\phi S_g}{V_g} \qquad (4)$$

where

V_p --- average compressive velocity of the sediment;

V_h --- compressive velocity of the pure hydrate;

V_{Aq} --- compressive velocity of the pore water (aqueous phase);

V_m --- compressive velocity of the mineral;

V_g --- compressive velocity of the gas phase;

S_h --- hydrate saturation;

S_g --- vapor (gas) saturation;

ϕ --- porosity;

and average densities via equation:

$$\bar{\rho} = (1-\phi)\rho_m + \phi \sum_i S_i \rho_i, \ \ phase\ i = Aq, h, g \quad (5).$$

The parameters are in Table 1.

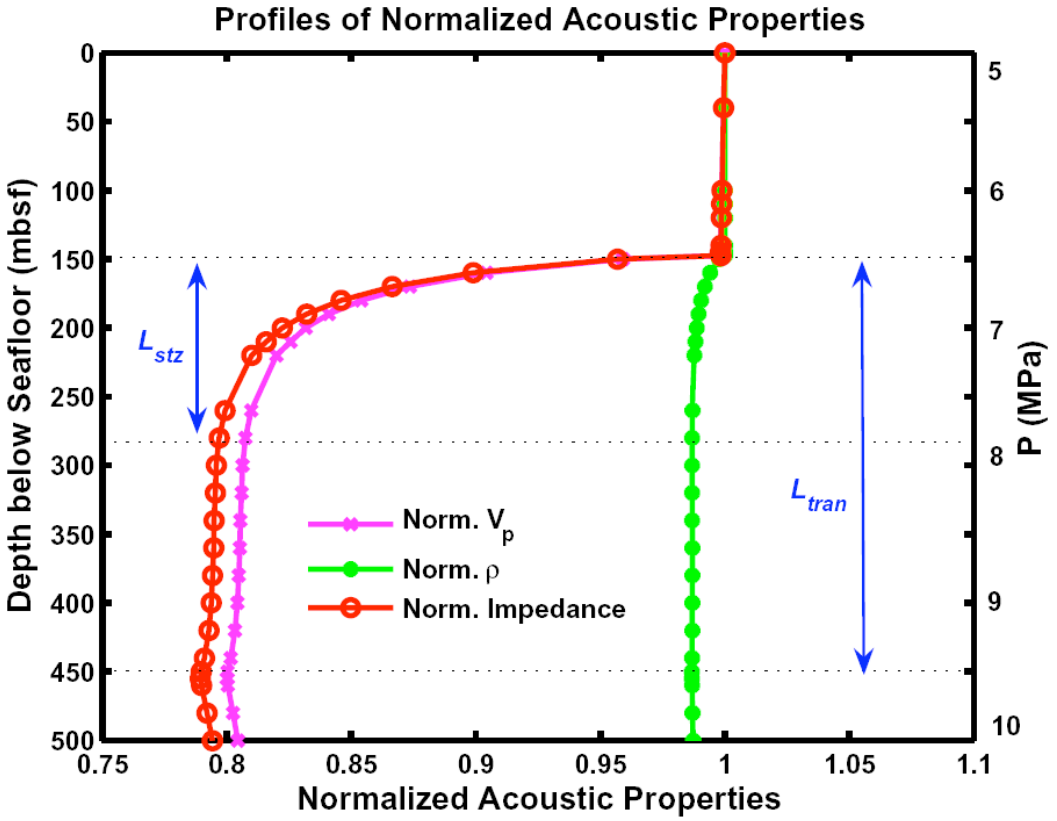

Figure 6. Profiles of normalized acoustic properties in an example CH_4-C_3H_8-H_2O System. Conditions are the same as Figure 3. Impedance $Z = \rho V_p$. Data are normalized to those at seafloor.

Table 1. Parameters for Acoustic Properties Estimation

Component	$V_{p,i}$ (m/s)	ρ_i (kg/m^3)
Sea Water (w)	1500	1030
Hydrate (H)	3300	900
Mineral (m)	2000	2600
Vapor (V, average)	~400	~ 50

For comparison purpose, two different types of Vp profiles from seafloor to deeper sediment are shown in Figure 7 – 8. The Vp profile and its impulse response for a pure methane hydrate system are shown in Figure 7, while those for a methane-propane hydrate system are shown in Figure 8. For a pure methane hydrate system, there is an abrupt decrease of Vp at Base of GHSZ, therefore, its impulse response at Base of GHSZ (BGHSZ) is in the similar order of magnitude of that at seafloor (Figure 7), which is also called a strong BSR.

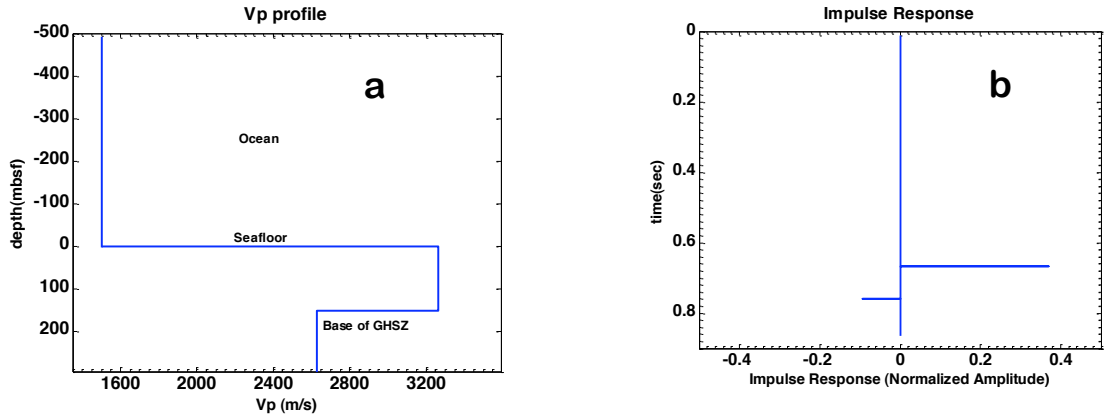

Figure 7. Impulse Response of a step change Vp system (BSR); (a) Vp profile; (b) Power spectrum in frequency domain

However, for a methane-propane hydrate system, the change of Vp at Base of GHSZ is gradual, therefore the amplitude of reflection at BGHSZ is much weaker than that at seafloor (Figure 8).

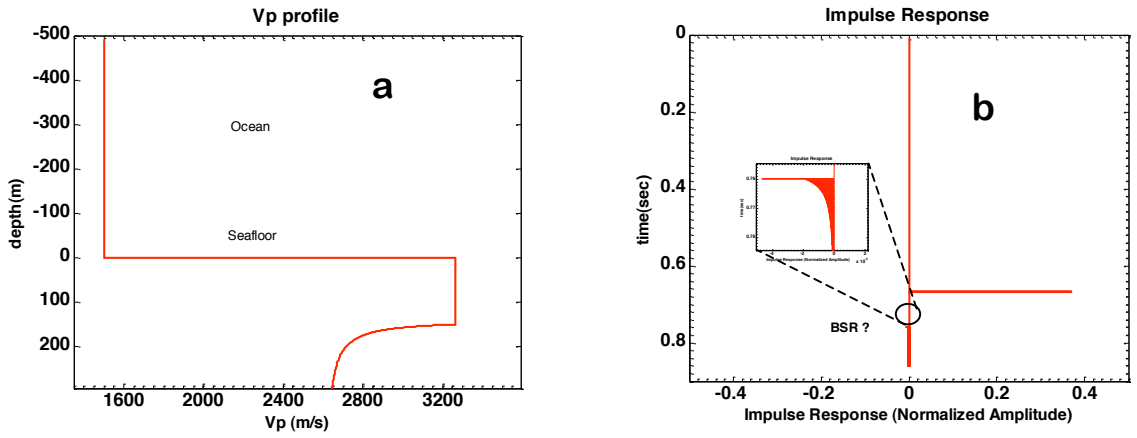

Figure 8. Impulse Response of a system with a transition zone; (a) Vp profile; (b) Impulse Response (the insert figure is the response at the transition zone)

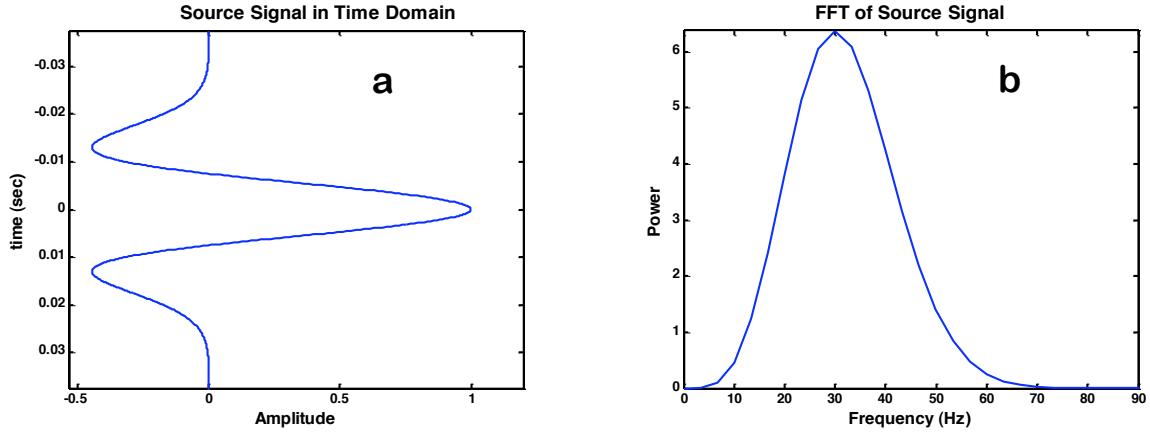

Figure 9. A sample Ricker wavelet, f_{peak}=30 Hz; (a) In time domain; (b) Power spectrum in frequency domain

Synthetic seismic responses are generated by using Ricker wavelets, which can be expressed as:

$$g(t) = (1 - 2\pi^2 f_p{}^2 t^2)\exp(-\pi^2 f_p{}^2 t^2) \qquad (4)$$

where f_p is the peak frequency. A sample is shown in Figure 9. A Ricker wavelet has a smooth power spectrum curve, with a peak frequency, f_p = 30 Hz (Figure 9). They are widely used in seismic simulators. In exploration seismic simulation, the peak frequency is mostly in a range from 10 to 100 Hz, and 30 Hz is a typical frequency.

The synthetic seismic response is generated by convolving the source wavelet (here is Ricker wavelet) and the system impulse response.

$$f_r(t) = I_r(t) * g(t) \qquad (5)$$

where $I_r(t)$ --- the Impulse Response of the hydrate system;

$f_r(t)$ --- the reflection of the hydrate system due to an input signal (e.g., a Ricker wavelet).

By using Ricker wavelets, with frequency from 10 to 100 Hz, we obtained the synthetic seismogram (Figure 10), both for that from a step change Vp profile (i.e., for pure methane hydrate system), and for that from a gradual transition zone. For the same thickness of the steep transition zone L_{stz}, different peak frequencies are used; for each wavelet with a certain peak frequency, the characteristic wavelength is denoted as λ. The thickness ratio L_{stz}/λ are calculated. The seismograms are shown in Figure 10.

To quantitatively understand the seismic response, the amplitude ratio, Ratio of Amplitude at Hydrate/Gas Transition, to that at Seafloor, A_{Hdr}/A_{sfl}, is defined. If $A_{Hdr}/A_{sfl} \leq 0.1$, the reflection will be called a "weak reflection" (i.e., weak BSR). The relationship between A_{Hdr}/A_{sfl} and thickness ratio L_{stz}/λ is plotted in Figure 11. We can find out both qualitatively (in Figure 10.) and quantitatively (in Figure 11.) that:

If $L_{stz}/\lambda > 0.5$, then $A_{Hdr}/A_{sfl} \leq 0.1$, i.e., a weak reflection will be observed.

In Figure 11, $A_{Hdr}/A_{sfl} \leq 0.1$ for peak frequencies higher than 30 Hz (roughly). But 30 Hz is a typical frequency. Therefore, if a mixed-hydrate transition zone exists, it's possible to observe a "weak BSR".

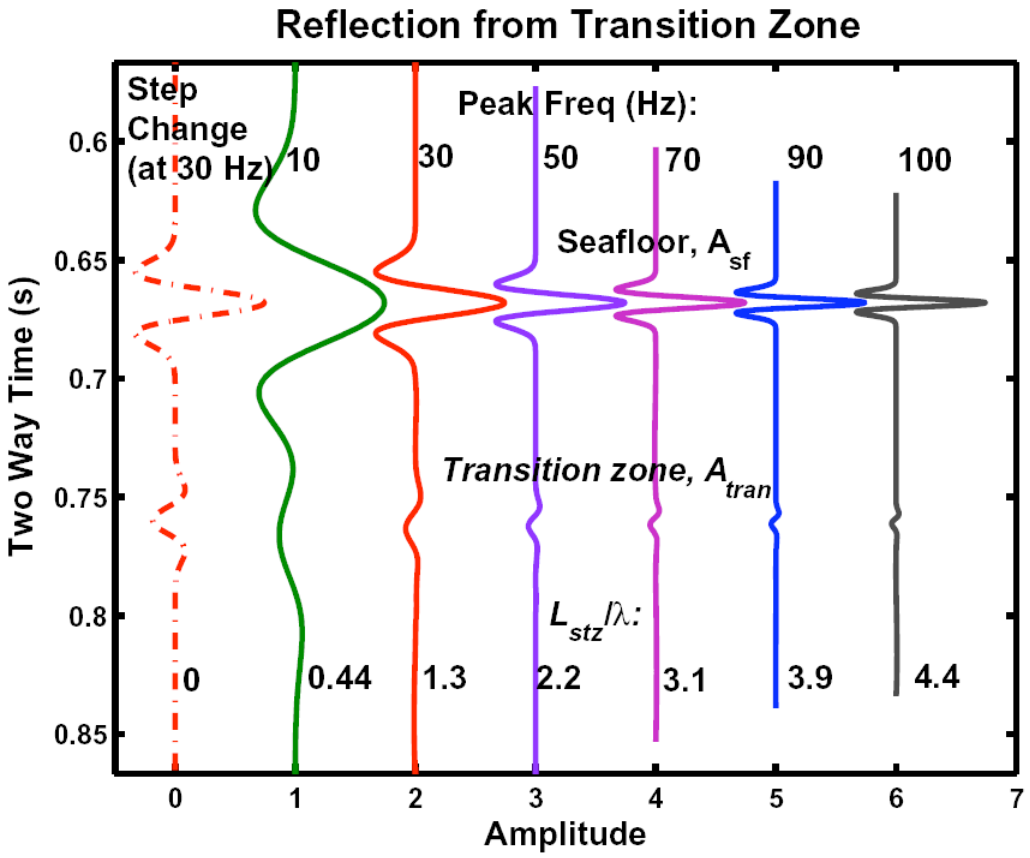

Figure 10. Seismic Response from Transition Zone.

The numbers in the bottom are L_{stz}/λ.

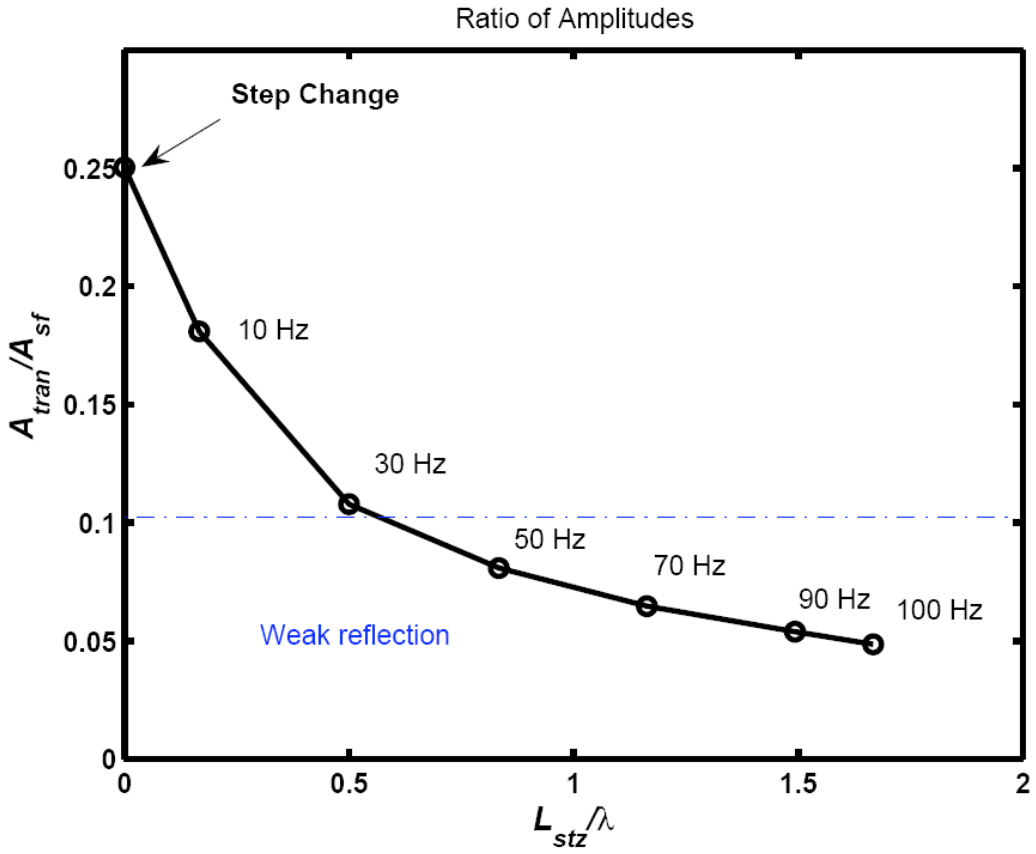

Figure 11. Amplitude Ratio as a Function of L_{stz}/λ.

(The Ratio of Amplitude at Hydrate/Gas Transition, to that at Seafloor, A_{tran}/A_{sf}). If $A_{tran}/A_{sf} \leq 0.1$, the reflection is called a "weak reflection", as shown in the shadowed region. The peak frequency for each point is also labeled.

Conclusions

For the CH_4-C_3H_8-H_2O hydrate system, the incipient hydrate formation conditions are presented. There is a big difference for the incipient hydrate formation condition of the CH_4-C_3H_8-H_2O hydrate system, from that of the CH_4- H_2O hydrate system, even when the water-free-propane molar fraction is only 0.01.

Three different phase regions are described for different *P-T* conditions. As shown in Figure 3. Region B is especially important, because Aq, H (sII), V can co-exist. Therefore, in the sediment, 3 zones can be present. Zone B, is the phase-transition-zone, because Aq, H (sII), V co-exist, and S_H and S_v change gradually.

The result of an example saturation calculation of the CH_4-C_3H_8-H_2O hydrate system in the sediment is presented. It successfully demonstrated that continuous change of S_H and S_v over a long spatial distance (~300 m) is possible. A gradual change of

saturations, may result in gradual change of acoustic properties, and induce weak BSR or even no BSR, depending on thickness ratio L_{stz}/λ.

Subtask 6.4: Amplitude Attenuation and chaotic zones due to hydrate distribution (Guangsheng Gu)

Sediment Acoustic impedance analysis:

Seismic blanking has been reported and discussed in many papers (Taylor, 1992; Lee, 2001). Due to hydrate accumulation, the velocity in different types of sediment layers can become similar with each other.

However, is seismic blanking ubiquitous in hydrate systems? Can blanking be regarded as a key indicator for hydrate detection? Here we have used some simple models to study this issue.

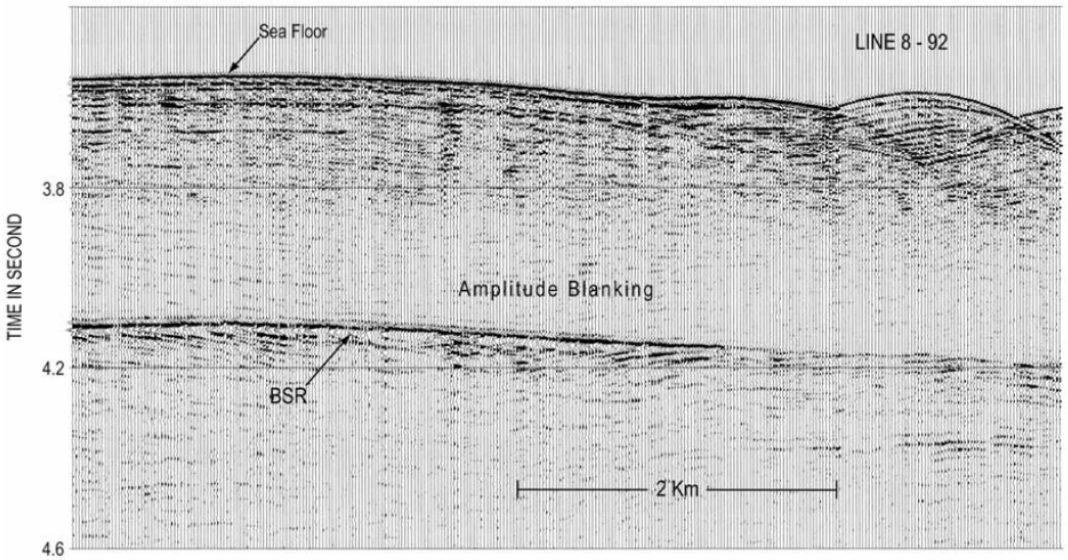

Figure 1. A single channel seismic profile showing the amplitude blanking and BSR. The data were acquired at the Blake Ridge using a single 160 in^3 air gun in 1992. (Taylor et al., 1992)

Figure 6.4.1. Seismic Profile in Blake Ridge; Amplitude Blanking in lateral strata is reported and discussed. (Lee, 2001)

Geological settings:

We set two horizontal layers with different properties, from seafloor to deeper sediment. Layer 1 (e.g., sand layer), with higher porosity (20%~30%); Layer 2, shale/clay layer. Assume hydrate saturation S_H can increase from 0 to 100% in Layer 1, and S_h in Layer 2 is always 0. Then the V_p, density, seismic impedance, and reflection coefficient are estimated.

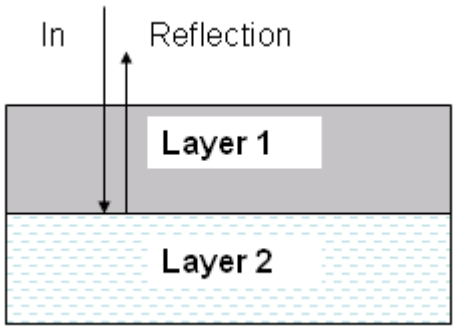

$\phi_1, V_1, S_{H,1}, S_{Aq,1}, S_{G,1}$

$\phi_2, V_2, S_{H,2}, S_{Aq,2}, S_{G,2}$

Figure 6.4.2. Geological setting

Two layers, with different acoustic properties and saturations. Assign Layer 2 as shale/clay layer; Layer 1 is to be assigned, typically as a sand layer.

Impedance is: $Z = \rho V_p$

Reflection coefficient:

$$R = \frac{Z_2 - Z_1}{Z_2 + Z_1}$$

Parameters are summarized in Table 6.4.1- 6.4.2:

Table 6.4.1: Acoustic properties of components

Component	***V*p (m/s)**	***r* (kg/m3)**
Sea Water (w)	1500	1030
Hydrate (H)	3300	900
Vapor (V)	400	50
Mineral1 (sand)	200 ~ 2000	2650
Mineral2 (diatomite)	2000	2000
Reference Mineral (shale/clay)	2000 ~ 2400	2600

Reference: W.J. Winters and W.F. Waite (2007). Acoustic velocities from W.J. Winters and W.F. Waite (2007); Sloan (2007). Nick Barton, Rock Quality, Seismic Velocity, Attenuation and anisotropy, Taylor & Francis Group, 2007, p. 12.

Table 6.4.2: Other parameters

Parameter	**Porosity**
Porosity1 (layer 1)	**0.2 ~ 0.3**
Porosity2 (in layer 2, shale/clay layer)	**0.2~0.7**

References: Jenyon (2006), Magara (1980).

Equations

Estimation of average velocity is via a revised form of the Time-average Equation (Pearson *et al.*, 1983).:

$$\frac{1}{V_p} = \frac{\phi(1 - S_H - S_V)}{V_w} + \frac{\phi S_H}{V_H} + \frac{(1-\phi)}{V_m} + \frac{\phi S_V}{V_V}$$

V_p --- average compressional velocity of the sediment;

V_H --- compressional velocity of the pure hydrate;

V_w --- compressional velocity of the fluid;

V_m --- compressional velocity of the mineral;

ϕ --- porosity (as a fraction);

S_H --- Hydrate saturation

S_V --- Vapor (Gas) saturation

Average density is estimated via:

$$\overline{\rho} = (1-\phi)\rho_m + \phi \sum_i S_i \rho_i$$

phase *i* =*w,H,V.*

Result

Our study indicates that hydrate accumulation does not guarantee a blanking zone, and the blanking zone does not mean hydrate accumulates, neither. Only in limited parameter space, the blanking zone can be regarded due to hydrate accumulation.

Figure 6.4.4 show an example where hydrate accumulation induces seismic blanking zone. The acoustic impedance of sand layer, at S_h=0, is possible to be lower than that of a shale layer; therefore when hydrate saturation S_h increases, it's possible for impedance of sand layer to increase to higher values than that of a shale layer. In these situations, it's possible that a blanking can be achieved during the hydrate accumulation process.

However, this situation is heavily dependent on the parameters applied. These parameters include but not limited to: the intrinsic (i.e., without hydrate, water, or gas) velocity in sand layer, V_{p_sand}, and that in shale (clay) layer, V_{p_clay}, and also the porosities in these layer will contribute much to the seismic impedance contrast.

For example, if the parameters change a little bit, from those listed in Figure 6.4.4, to those listed in Figure 6.4.3., the V_{p_sand}=1500 m/s changed to 1000 m/s, then the average impedance in sand layer, Z_{sand}, will be always much lower than that in shale (clay) layer , Z_{clay}. Therefore, the blanking won't happen. Similarly, in Figure 6.4.5, the V_{p_sand}=2000 m/s, then the average impedance in sand layer, Z_{sand}, will be always much higher than that in shale (clay) layer , Z_{clay}. Therefore, the blanking won't happen, neither.

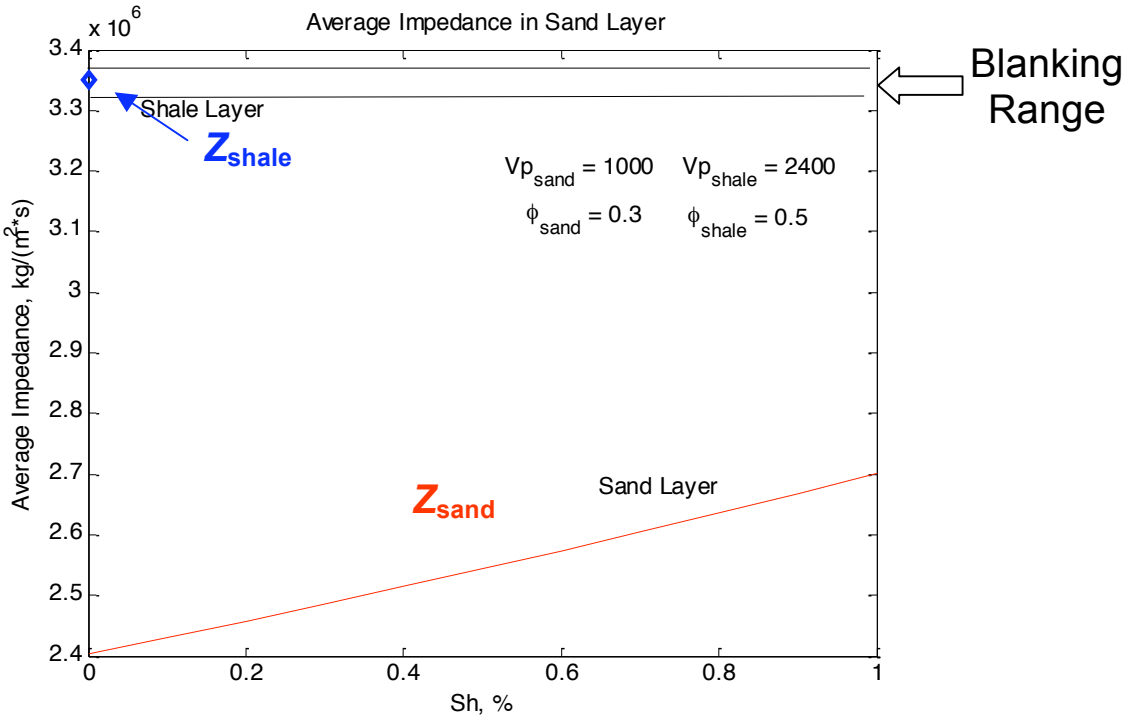

Figure 6.4.3: Impedance increase of sand layer due to S_h increase, where blanking is impossible. Parameters: ϕ_1=0.3; ϕ_2=0.5; intrinsic sand velocity V_{p_sand}=1000 m/s; intrinsic shale (or clay) velocit V_{p_clay}=2400 m/s. Assume S_{h_clay} = 0, since hydrate saturation in clay layer is often very close to 0. The blue diamond is the impedance in layer 2 (shale layer); the red curve is that in layer 1 (sand layer). The two horizontal lines indicate a blanking range in which seismic blanking is possible.

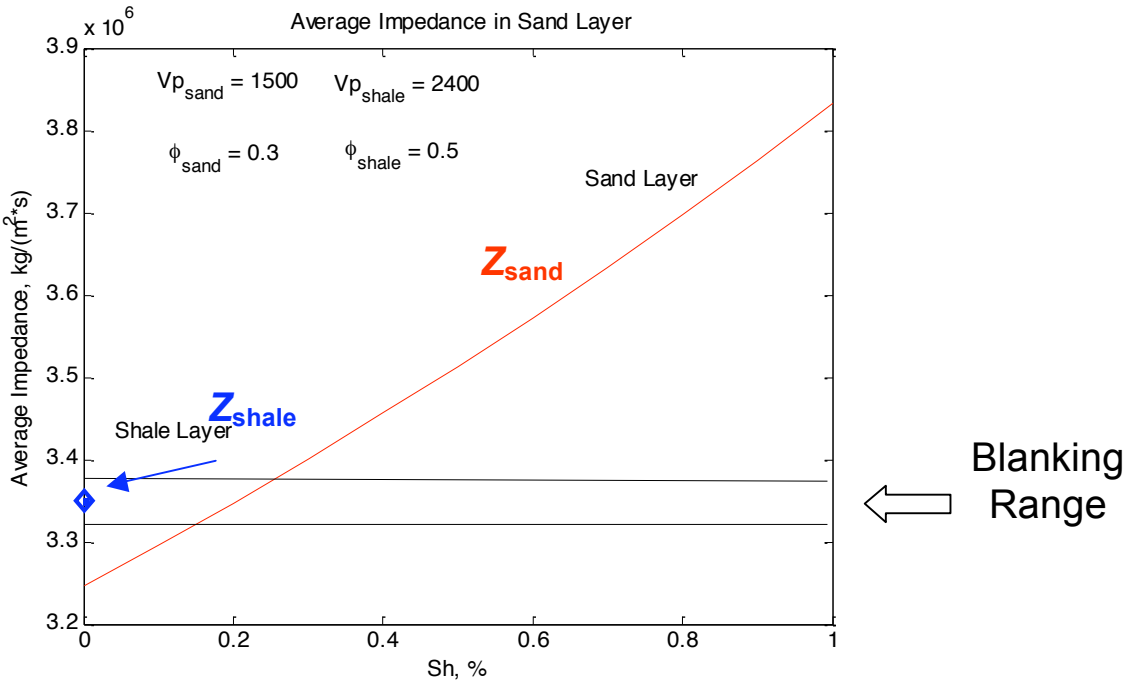

Figure 6.4.4: Impedance increase of sand layer due to S_h increase, where blanking is possible. Parameters: ϕ_1=0.3; ϕ_2=0.5; intrinsic sand velocity V_{p_sand}=1500 m/s; intrinsic shale (or clay) velocit V_{p_clay}=2400 m/s.

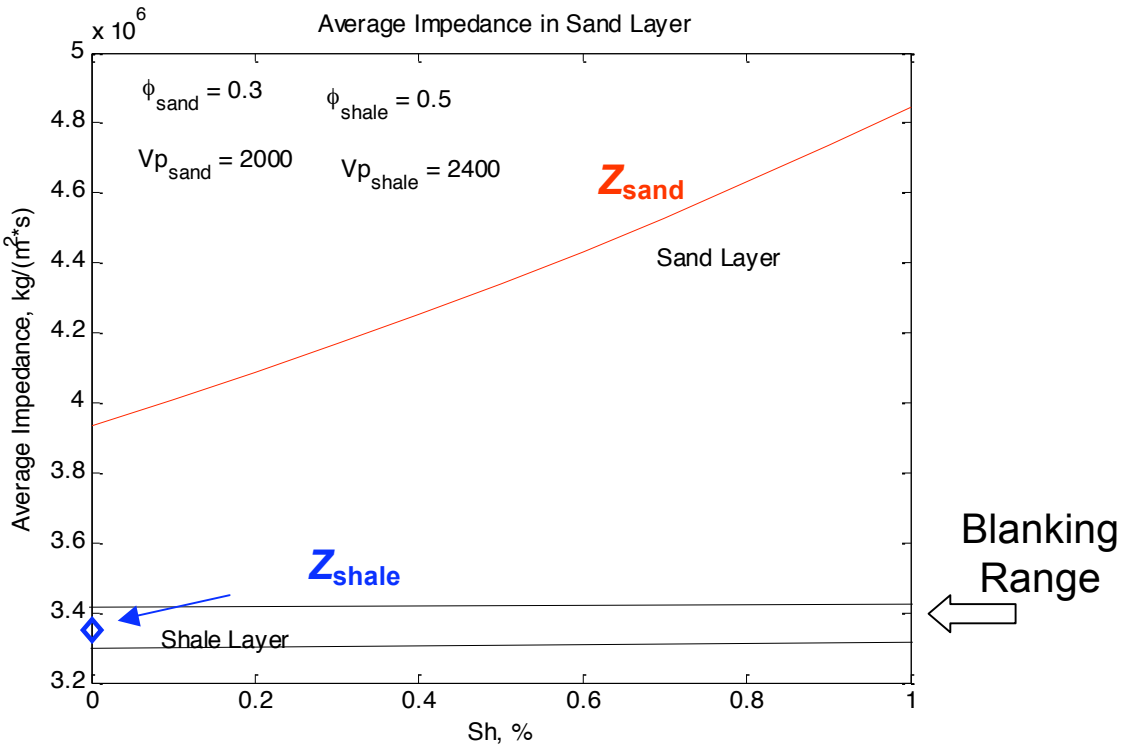

Figure 6.4.5: Impedance increase of sand layer due to S_h increase, where blanking is impossible. Parameters: ϕ_1=0.3; ϕ_2=0.5; intrinsic sand velocity V_{p_sand}=2000 m/s; intrinsic shale (or clay) velocit V_{p_clay}=2400 m/s.

Since the impedances and reflection coefficient are dependent on many parameters and variables, contour plots will better present the reflection coefficient than curves. Figure 6.4.6 shows an example of reflection coefficient in parameter space of S_h - ϕ_2, where S_h is the hydrate saturation in Layer 1 (sand layer), and ϕ_2 is the porosity in Layer 2 (shale/clay layer). Assume S_{h_clay} = 0. The box with blue dashed boundaries is the blanking region, with reflection coefficient less than 0.02. We can see that blanking region only occupies a small fraction of the parameter space, and almost close to boundary of the realistic parameter range of S_h - ϕ_2, or only when porosity ϕ_2 is higher than 0.65, it's possible to have blanking. So it's hard to have blanking.

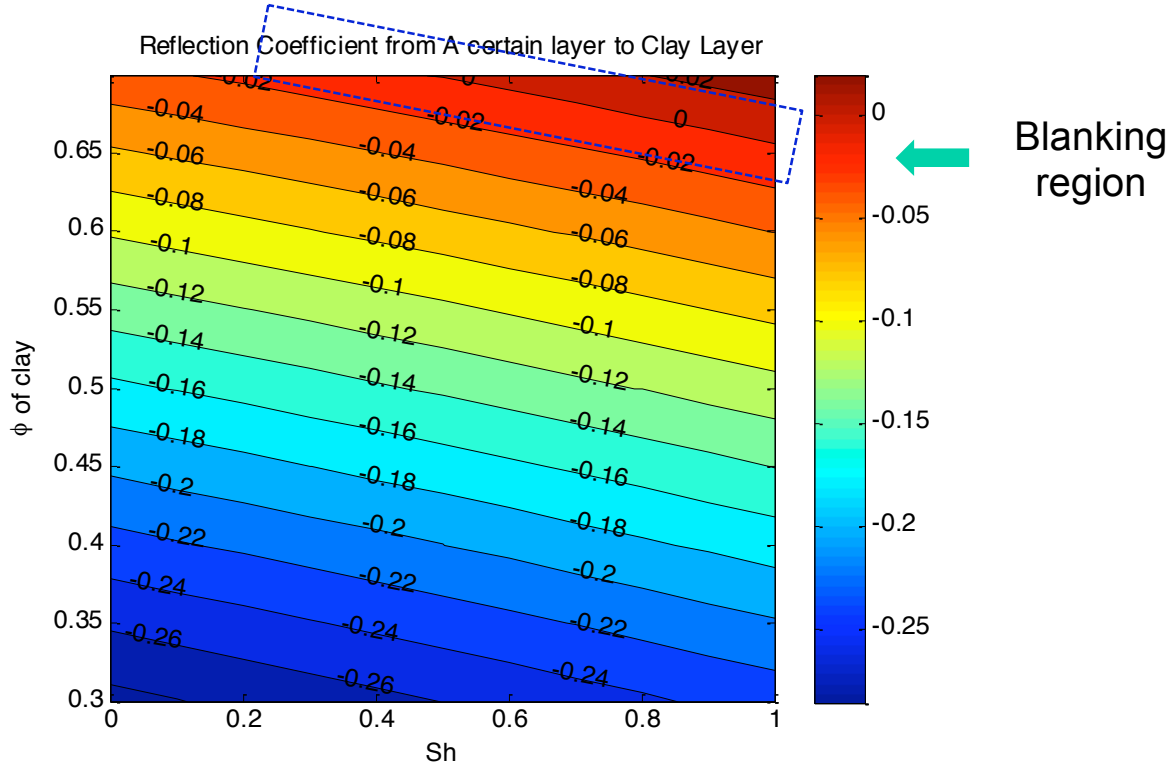

Figure 6.4.6: The reflection coefficient from Layer 1 to Layer 2, in the parameter space of S_h - ϕ_2, example I - hard to be blanking. Parameters: ϕ_1=0.3; intrinsic sand velocity V_{p_sand}=1000 m/s, density 2650 kg/m^3; intrinsic shale (or clay) velocit V_{p_clay}=2400 m/s, density 2600 kg/m^3. Assume S_{h_clay} = 0. Sh is the saturation of hydrate in Layer 1 (sand layer); $\boldsymbol{\phi_2}$ is the porosity in Layer 2 (shale/clay layer). The box with blue dashed boundaries is the blanking region, with reflection coefficient less than 0.02.

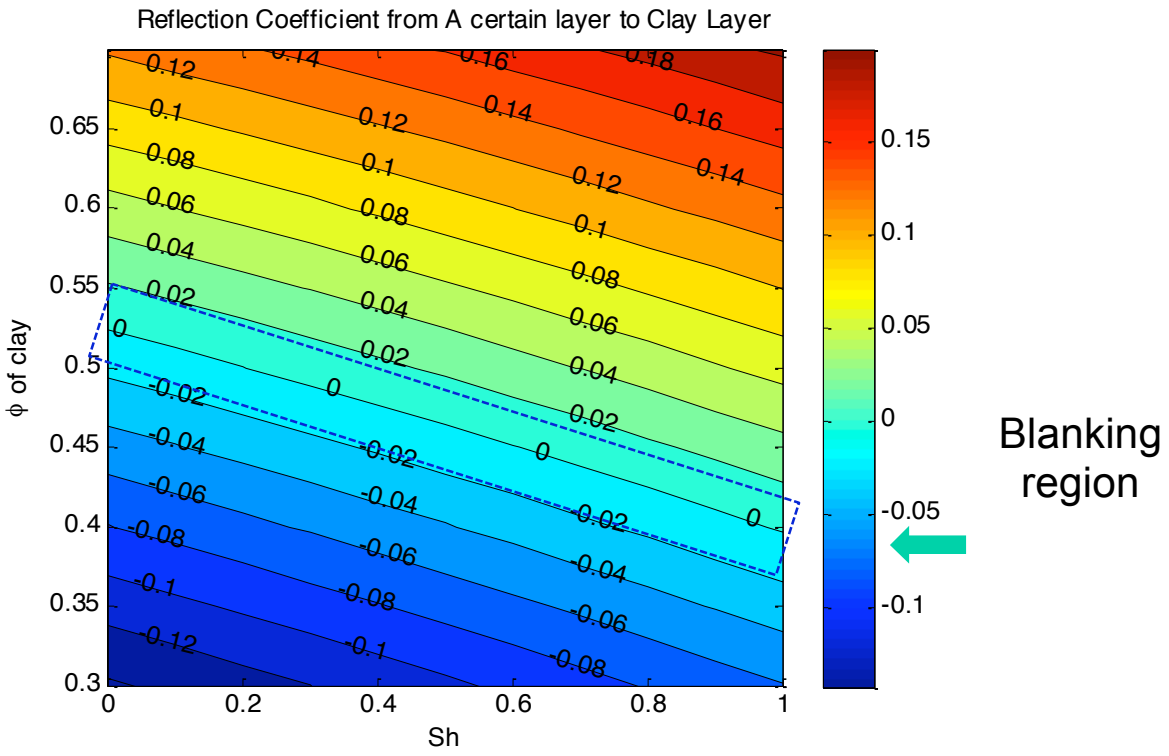

Figure 6.4.7: The reflection coefficient from Layer 1 to Layer 2, in the parameter space of S_h - ϕ_2, example II – easier to be blanking. Parameters: ϕ_1=0.3; intrinsic sand velocity V_{p_sand}=1500 m/s, density 2650 kg/m^3; intrinsic shale (or clay) velocit V_{p_clay}=2400 m/s, density 2600 kg/m^3. Assume S_{h_clay} = 0. Sh is the saturation of hydrate in Layer 1 (sand layer); $\boldsymbol{\phi_2}$ is the porosity in Layer 2 (shale/clay layer). The box with blue dashed boundaries is the blanking region, with reflection coefficient less than 0.02.

However, Figure 6.4.7 shows an example of reflection coefficient in parameter space of S_h - ϕ_2, which is easier to be blanking than Figure 6.4.6. Though the blanking region still only occupies a limited fraction of the parameter space, but the fraction is higher than that in Figure 6.4.6.

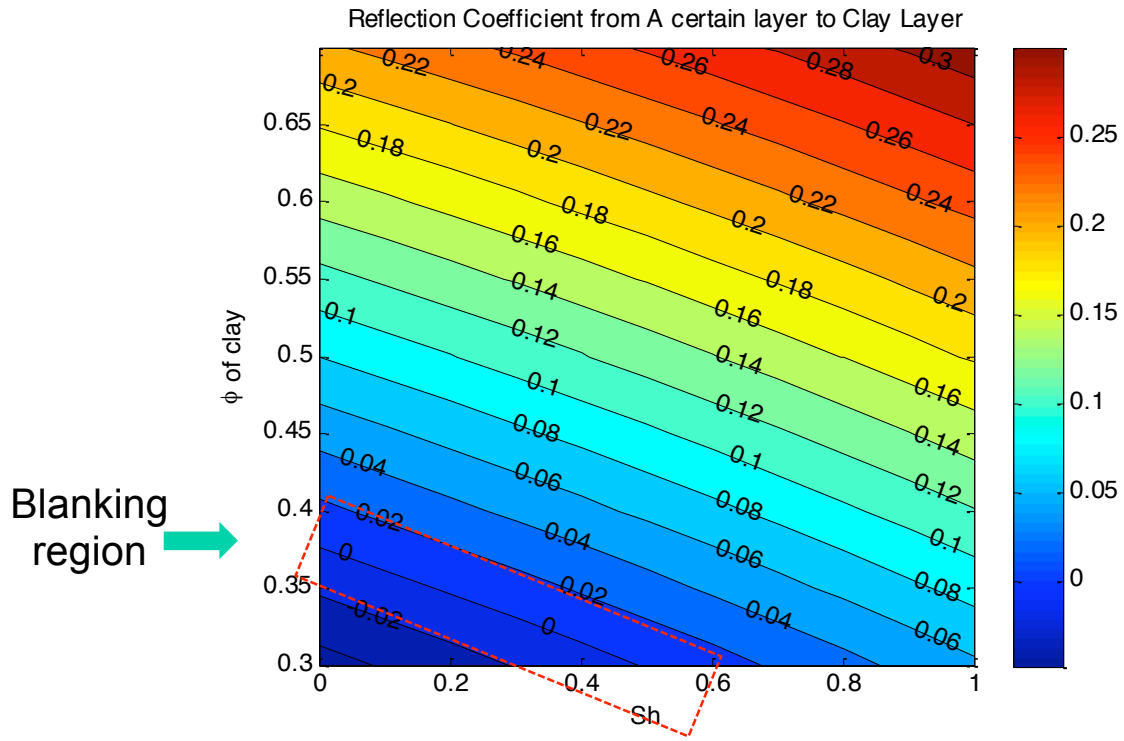

Figure 6.4.8: The reflection coefficient from Layer 1 to Layer 2, in the parameter space of S_h - ϕ_2, example III – hard to be blanking. Parameters: ϕ_1=0.3; intrinsic sand velocity V_{p_sand}=2000 m/s, density 2650 kg/m^3; intrinsic shale (or clay) velocit V_{p_clay}=2400 m/s, density 2600 kg/m^3. Assume S_{h_clay} = 0. Sh is the saturation of hydrate in Layer 1 (sand layer); $\boldsymbol{\phi_2}$ is the porosity in Layer 2 (shale/clay layer). The box with blue dashed boundaries is the blanking region, with reflection coefficient less than 0.02.

Similar to Figure 6.4.6, Figure 6.4.8 shows an example of reflection coefficient in parameter space of S_h - ϕ_2, which is hard to have blanking either. Assume S_{h_clay} = 0. We can see that blanking region only occupies a small fraction of the parameter space, and almost close to boundary of the realistic parameter range of S_h - ϕ_2, or only when porosity ϕ_2 is lower than 0.4, it's possible to have blanking. So it's hard to have blanking.

The same characteristics is that, in each of these examples, blanking region is always a small fraction of area of parameter space. Therefore, we can conclude that seismic blanking is hard to happen in hydrate systems.

Conclusions

(1) Hydrate accumulation in marine sediment is helpful for blanking;

(2) Sensitive to parameters and stratum lithology;

(3) Blanking in hydrate system isn't ubiquitous. Hydrate accumulation doesn't guarantee a blanking.

Subtask 6.5: Processes leading to overpressure (Gaurav Bhatnagar and Sayantan Chatterjee)

The effect of overpressure on gas hydrate and free gas distribution in marine sediments is studied using a one-dimensional numerical model that couples sedimentation, fluid flow, and gas hydrate formation. Natural gas hydrate systems are often characterized by high sedimentation rates and/or low permeability sediments, which can lead to pore pressure higher than hydrostatic (overpressure). To quantify the relative importance of these two factors, we define a dimensionless sedimentation-compaction group, N_{sc}, that compares the absolute permeability of the sediments to the sedimentation rate. Higher values of N_{sc} mean higher permeability or low sedimentation rate which generally yield hydrostatic pore pressure. Conversely, lower values of N_{sc} generally create pore pressure greater than hydrostatic. Simulation results show that decreasing N_{sc} not only increases pore pressure above hydrostatic values, but also lowers the lithostatic stress gradient and gas hydrate saturation. This occurs because overpressure results in lower effective stress, causing higher porosity and lower bulk density of the sediment. This leads to higher sediment velocity through the gas hydrate stability zone, thereby reducing the mass accumulation of methane and gas hydrate in the pore space. Effect of overpressure on depth of the gas hydrate stability zone is also studied.

We are also assessing sediment stability in gas hydrate bearing marine systems. We are using infinite slope stability analysis in our geologic accumulation models (in collaboration with Task 8). This is the first step in trying to address the evolution of geohazards related to hydrate systems. This technique is computationally inexpensive, applicable in geologic and reservoir models, and provides a quick look at stability to identify locations for detailed stability analysis.

Subtask 6.6: Concentrated hydrate and free gas (Sayantan Chatterjee and Hugh Daigle)

Fracture-hosted methane hydrate deposits exist at many sites worldwide. These sites often have hydrate present as vein and fracture fill, as well as disseminated through the pore space. We estimate that thousands to millions of years are required to form fracture systems by hydraulic fracturing driven by occlusion of the pore system by hydrate. This time scale is a function of rates of fluid flow and permeability loss. Low-permeability layers in a sedimentary column can reduce this time if the permeability contrast with respect to the surrounding sediments is of order 10 or greater. Additionally, we find that tensile fracturing produced by hydrate heave around hydrate lenses is a viable fracture mechanism over all but the lowermost part of the hydrate stability zone. With our coupled fluid flow-hydrate formation model we assess fracture formation at four well-studied hydrate provinces: Blake Ridge offshore South Carolina, Hydrate Ridge offshore Oregon, Keathley Canyon Block 151 offshore Louisiana, and the Krishna-Godavari Basin offshore India. We conclude that hydraulic fracturing due to pore pressure buildup is reasonable only at Hydrate Ridge and the Krishna-Godavari

Basin owing to sediment age constraints, and that hydrate-filled fractures observed at Blake Ridge and Keathley Canyon Block 151 are formed either by hydrate heave or in preexisting fractures. Our findings offer new insight into the processes and time scales associated with fracture-hosted hydrate deposits, which help further our understanding of hydrate systems.

We simulate gas hydrate and free gas accumulation in heterogeneous marine sediments over geologic time scales. Simulations with a vertical fracture network, which extends through the gas hydrate stability zone and has permeability 100 times greater than the surrounding shale formation, show that focused fluid flow causes higher hydrate (25-55%) and free gas saturation (30-45%) within the fracture network compared to the surrounding, lower permeability shale. Systems with high permeability, dipping sand layers also show localized, elevated saturations of hydrate (60%) and free gas (40%) within the sand layers due to focused fluid flow. Permeability anisotropy, with a vertical to horizontal permeability ratio on the order of 10^{-2}, enhances hydrate concentrations within high permeability conduits because anisotropy enhances transport of methane-charged fluid to high permeability conduits. Our two-dimensional (2-D), heterogeneous models quantify how focused fluid flow through high permeability zones affects local hydrate accumulation and saturation. We also show increased fluid flux and deep source methane input result in enhanced concentrations of hydrate and free gas, and also increase the flow focusing effects. From our 2-D results, we determine that the hydrate and free gas saturations can be characterized by the local Peclet number (localized, focused, advective flux relative to diffusion); which is consistent with Peclet number characterization in one-dimensional (1-D) systems. This characterization suggests that even in lithologically complex systems, local hydrate and free gas saturations can be characterized by basic parameters (local flux and diffusivity).

Subtask 6.7 Focused free gas, heat and salinity (Sayantan Chatterjee, Guangsheng Gu and Hugh Daigle)

We simulate methane hydrate formation with multiphase flow and free gas within the regional hydrate stability zone (RHSZ). We find that hydrate distribution and fracture behavior are largely determined by the phase of the methane supply. We allow free gas to enter the RHSZ when pore water salinity increases to the value required for three-phase equilibrium. Fractures nucleate when the excess pore pressure exceeds the vertical hydrostatic effective stress. At Hydrate Ridge, where methane supply is dominantly free gas, hydrate saturation increases upwards and fractures nucleate high within the RHSZ, eventually allowing gas to vent to the seafloor. At Blake Ridge, where methane supply is dominantly in the dissolved phase, hydrate saturation is greatest at the base of the RHSZ; fractures nucleate here and in some cases could propagate through the RHSZ, allowing methane-charged water to vent to the seafloor.

We simulate 1-D, steady, advective flow through a layered porous medium to investigate how capillary controls on solubility including the Gibbs-Thomson effect in fine-grained sediments affect methane hydrate distribution in marine sediments. We compute the increase in pore fluid pressure that results from hydrate occluding the pore space and allow fractures to form if the pore fluid pressure exceeds a fracture criterion.

We apply this model to Hydrate Ridge and northern Cascadia, two field sites where hydrates have been observed preferentially filling cm-scale, coarse-grained layers. We find that at Hydrate Ridge, hydrate forms in the coarse-grained layers reaching saturation of 90%, creating fractures through intervening fine-grained layers after 2000 years. At northern Cascadia, hydrate forms preferentially in the coarse-grained layers but 2×10^5 years are required to develop the observed hydrate saturations (~20%–60%), suggesting that hydrate formation rates may be enhanced by an additional source of methane such as in situ methanogenesis. We develop expressions to determine the combinations of sediment physical properties and methane supply rates that will result in hydrate-filled coarse-grained layers separated by hydrate-filled fine-grained layers, the conditions necessary to fracture the fine-grained layers, and the conditions that will lead to complete inhibition of hydrate formation as pore space is constricted. This work illustrates how sediment physical properties control hydrate distribution at the pore scale and how hydrate distribution affects fracturing behavior in marine sediments.

Gas hydrate formation and its dissociation to free gas alters the pore water salinity, which in turn affects the phase equilibrium of the system (e.g., *Zatsepina and Buffett*, 1998; *Egeberg and Dickens*, 1999; *Milkov et al*., 2004; *Liu and Flemings*, 2006). Moreover, high gas flux typical of specific sites have dominant salinity anomalies caused due to enormous hydrate formation (*Milkov et al*., 2004; *Liu and Flemings*, 2006, 2007). The salinity effects had been assumed to be negligible in the previous 1-D modeling (e.g., *Davie and Buffett*, 2001, 2003; *Bhatnagar et al*., 2007) since salt (NaCl, or equivalently, Cl^-) mass balance was not coupled with the phase equilibrium thermodynamics. In the 2-D model (subtask 6.6), salinity changes have been neglected as well. As a result, free gas migration into the GHSZ is restricted only till the first grid block. As soon as free gas invades the GHSZ, the CH_4 phase changes from free gas to hydrate due to thermodynamic equilibrium. This is not true in many geologic settings where free gas is observed to independently exist near the seafloor (*Trehu et al*., 2003; *Milkov et al*., 2004). Recently, several papers have shown coexistence of hydrate and free gas phases of CH_4 within the GHSZ due to salinity effects in 1-D (e.g., *Liu and Flemings*, 2007; *Daigle and Dugan*, 2010).

A 2-D chloride mass balance is incorporated and coupled with the benchmarked 2-D model developed in this study. During hydrate formation, the chlorides are released by the pore fluids when fresh water forms the cage structure during hydrate formation. This leads to local elevation of salinity where hydrates are formed. By contrast, the pore fluids become less saline due to local freshening during hydrate dissociation. The chloride concentrations are tracked in the model over space and time (same as the other dissolved constituents) as they move by advection and diffusion and the salinity is computed from these chloride profiles. The model is tested against the field data from Blake Ridge Site 997 where pore water chlorinity (and other geochemical datasets) exist.

The pore water chlorinity is often related to the pore water activity and salinity. The effect of salinity variation on CH_4 hydrate stability conditions is related to the pore water

activity (*Dickens and Quinby-Hunt*, 1994, 1997). In this study, the spatial Cl^- profiles are used to track space- and time-dependent salinity during hydrate formation and dissociation processes. In the existing 2-D model, CH_4 solubility curve is computed as a function of pressure and temperature, assuming constant seawater salinity. As ongoing work, CH_4 solubility is being coupled with salinity changes in the hydrate accumulation model. This leads to recomputing the phase equilibrium and CH_4 solubility with variations in salinity. This leads to a zone of three-phase coexistence, as opposed to a single point representing the triple-point of CH_4 in the salinity-independent model. In essence, this would enable coexistence of free gas and hydrate phase within the GHSZ over a depth horizon. This would allow free gas existence in the GHSZ and lead to focused free gas and enhanced hydrate saturations. A three-phase flash calculation is required to be set up to calculate the different phase fractions (aqueous, hydrate, and gas) present within a specific grid-block at each timestep depending on the thermodynamic conditions. The current 2-D multiphase transport model with the three-phase flash calculation should be capable of simulating conditions with three-phase co-existence within the GHSZ. This is not been modeled and has evolved as one of the future work arising from this study.

Subtask 6.8a Sulfate profile as indicator of methane flux (Gaurav Bhatnagar)

Numerical model

We develop a relationship between the sulfate-methane transition (SMT) and average gas hydrate saturation (AGHS) for systems dominated by methane migration from deeper sources. The relationship is explained by a one-dimensional numerical model that simulates gas hydrate accumulation in marine sediments. Higher methane fluxes result in shallow SMT depths and high AGHS, while lower methane fluxes result in deep SMTs and low AGHS. We also generalize the variation between AGHS and scaled SMT depth, a procedure that aids prediction of AGHS at different sites from observations of the SMT, such as along Cascadia Margin.

Analytical model

We develop a theory that relates gas hydrate saturation in marine sediments to the depth of the sulfate-methane transition (SMT) zone below the seafloor using steady state, analytical expressions. These expressions are valid for systems in which all methane transported into the gas hydrate stability zone (GHSZ) comes from deeper external sources (i.e., advective systems). This advective constraint causes anaerobic oxidation of methane to be the only sulfate sink, allowing us to link SMT depth to net methane flux. We also develop analytical expressions that define the gas hydrate saturation profile based on SMT depth and site-specific parameters such as sedimentation rate, methane solubility, and porosity. We evaluate our analytical model at four drill sites along the Cascadia Margin where methane sources from depth dominate. With our model, we calculate average gas hydrate saturations across GHSZ and the top occurrence of gas hydrate at these sites as 0.4% and 120 mbsf (Site 889), 1.9% and 70 mbsf (Site U1325), 4.7% and 40 mbsf (Site U1326), and 0% (Site U1329),

mbsf being meters below seafloor. These values compare favorably with average saturations and top occurrences computed from resistivity log and chloride data. The analytical expressions thus provide a fast and convenient method to calculate gas hydrate saturation and first-order occurrence at a given geologic setting where vertically upward advection dominates the methane flux.

Subtask 6.8b Carbon cycling across SMT above marine gas hydrate systems (Sayantan Chatterjee)

Both the concentration and the carbon isotope composition of dissolved inorganic carbon (DIC) vary considerably across the sulfate-methane transition (SMT) in shallow marine sediment at locations with gas hydrate. This variability has led to different interpretations for how carbon, including CH_4, cycles within gas-charged sediment sequences over time. We extend a one-dimensional model for the formation of gas hydrate to account for downhole changes in dissolved CH_4, SO_4^{2-}, DIC, and Ca^{2+}, and the $\delta^{13}C$ of DIC. The model includes advection, diffusion, and two reactions that consume SO_4^{2-}: degradation of particulate organic carbon (POC) and anaerobic oxidation of methane (AOM). Using our model and site-specific parameters, steady state pore water profiles are simulated for two sites containing gas hydrate but different carbon chemistry across the SMT: Site 1244 (Hydrate Ridge; DIC = 38 mM, $\delta^{13}C$ of DIC = –22.5‰ PDB) and Site Keathley Canyon (KC) 151-3 (Gulf of Mexico; DIC = 16 mM, $\delta^{13}C$ of DIC = −49.6‰ PDB). The simulated profiles for CH_4, SO_4^{2-}, DIC, Ca^{2+}, and $\delta^{13}C$ of DIC resemble those measured at the sites, and the model explains the similarities and differences in pore water chemistry. At both sites, an upward flux of CH_4 consumes most net SO_4^{2-} at a shallow SMT, and calcium carbonate removes a portion of DIC at this horizon. However, a large flux of ^{13}C-enriched HCO_3^- enters the SMT from depth at Site 1244 but not at Site KC151-3. This leads to a high concentration of DIC with a $\delta^{13}C$ much greater than that of CH_4, even though AOM causes the SMT. The addition of HCO_3^- from depth impacts the slope of certain concentration crossplots. Crucially, neither the DIC concentration nor its carbon isotope composition at the SMT can be used to discriminate between sulfate reduction pathways.

Task 7: Analysis of Production Strategy

K. K. Mohanty, University of Texas at Austin

Subtask 7.1a Code comparison

Introduction

We participated in the NETL methane hydrate code comparison study to evaluate the capabilities of the in-house (University of Houston) simulator with respect to other existing hydrate simulators participating in the code comparison study. We have completed simulation of the first four problems set up by the Code Comparison Study group by our in-house hydrate simulator. Our results have been communicated to Prof. Brian Anderson, the coordinator of the Code Comparison Study group.

Results and Discussion

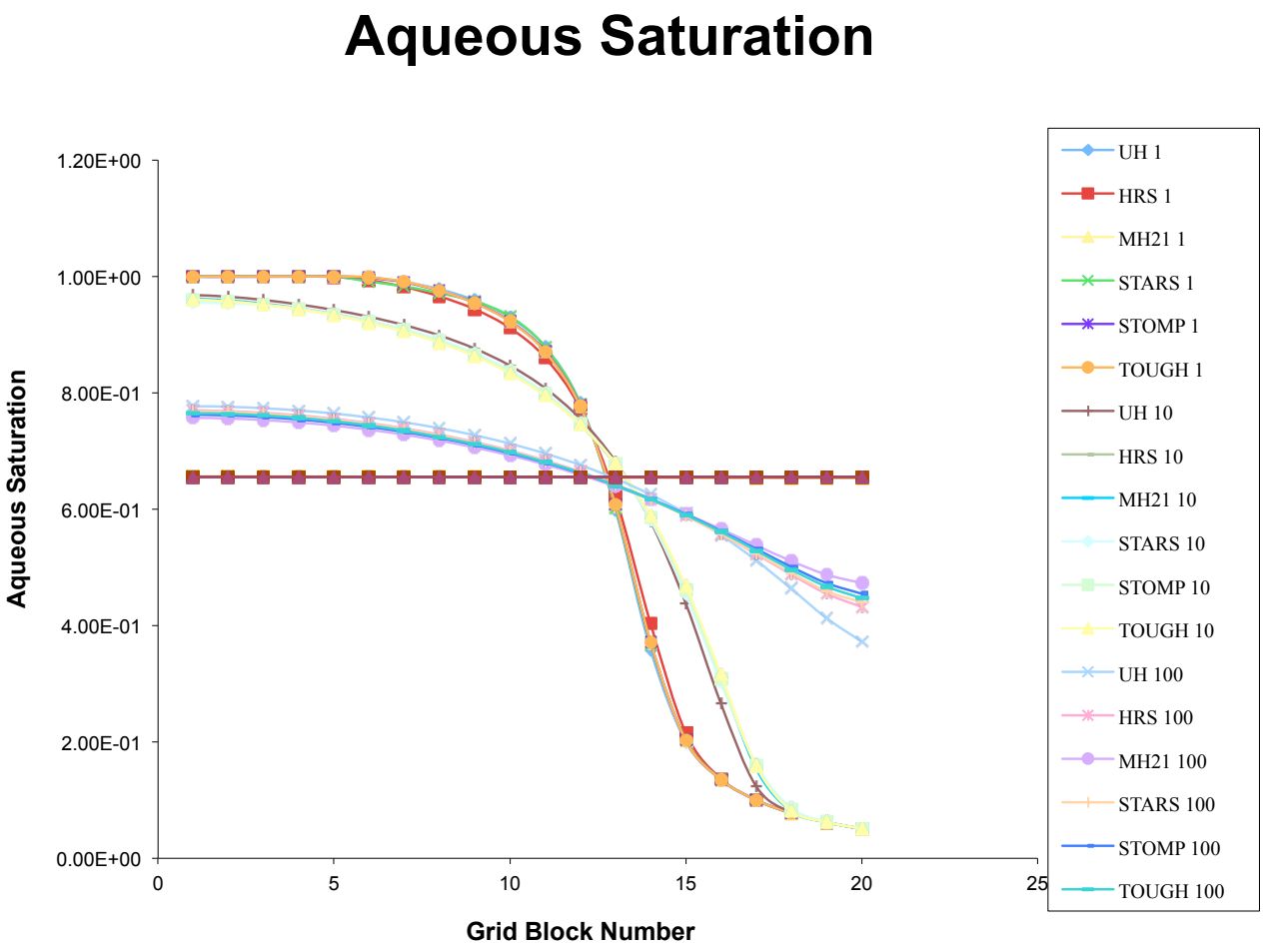

Figure 7.1.a.1. Water saturation (parameter is time in days) in Problem 1

Problem 1

This problem calculates transition to equilibrium in the absence of hydrates. The aqueous saturation, aqueous pressure and temperature calculated by our simulator are in complete agreement with the other results. There is a slight discrepancy in the mass fraction of methane in the aqueous phase. This may be due to different correlations used in different simulators for methane solubility. Our results are labeled UH in Figure 7.1.a.1.

Problem 2

This problem calculates transition to equilibrium in a closed domain with hydrate dissociation. There is a discrepancy in the position of the saturation front (Figure 7.1.a.2). We believe, that is due to the unspecified correlation of change of permeability with hydrate saturation. (This issue is present in all the problems except Problem 1). The sediment permeability changes with hydrate saturation; we have used a correlation. We do not know the correlations used by others. Heat conductivity of the hydrates is also not specified. It affects the heat flow and hence the slight deviation in the results. Our results are shown in yellow in the plots.

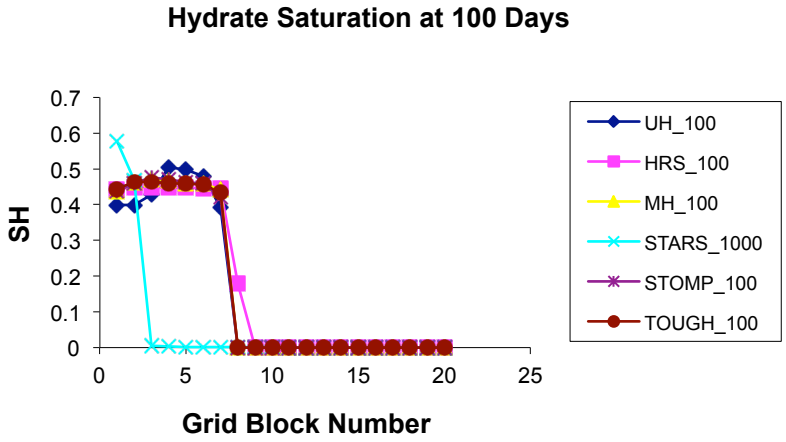

Figure 7.1.a.2. Comparison of hydrate saturation at 100 days in Problem 2

Problem 3

This problem calculates hydrate dissociation in an open 1D domain. In the first part, hydrate is dissociated by thermal stimulation. In the second part, hydrate is dissociated by depressurization without ice formation. In the third part, hydrate is dissociated by depressurization with ice formation for a very low pressure.

Thermal Stimulation (3_1)

Most of the results match except for the gas saturation (Figure 7.1.a.3), which is high because permeability is low. The aqueous saturation does not deviate much because

water is already present and gas is formed by dissociation of hydrates. The methane release curves are different because they depend on two processes: the increase in permeability due to hydrates melting and the amount of hydrates that melt.

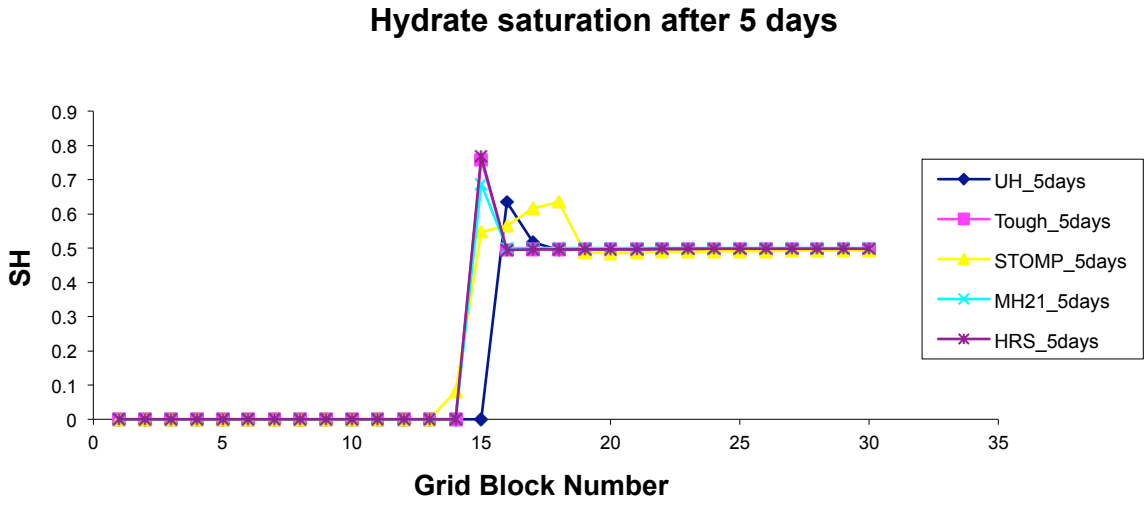

Figure 7.1.a.3. Comparison of hydrate saturation in Problem 3, part 1

Depressurization (3_2)

The results for all the simulators match except for a small difference in the shape of the hydrate front (Figure 7.1.a.4).

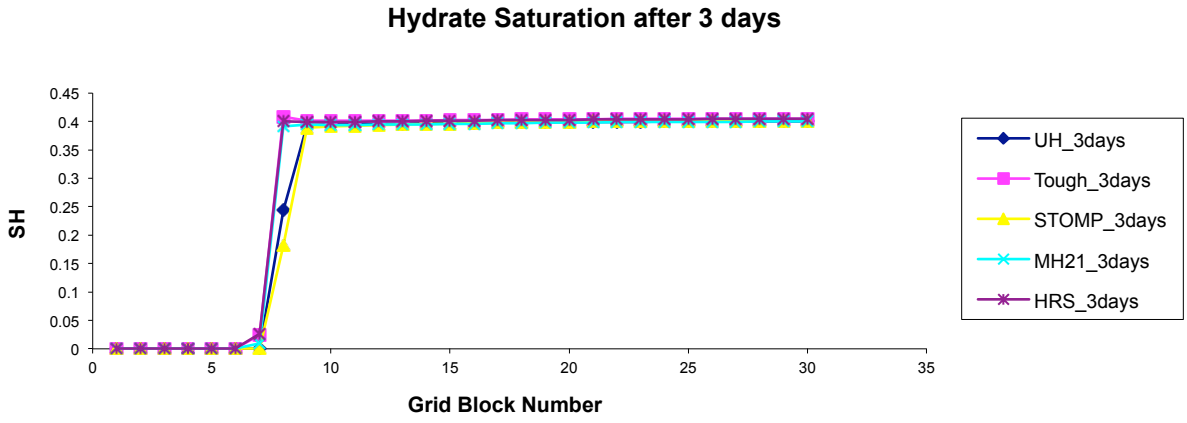

Figure 7.1.a.4. Comparison of hydrate saturation in Problem 3, part 2

Depressurization with ice formation (3_3)

Figure 7.1.a.5 shows the ice saturation at 5 days. Our, STOMP and MH21 results are stable, but the other results have oscillations.

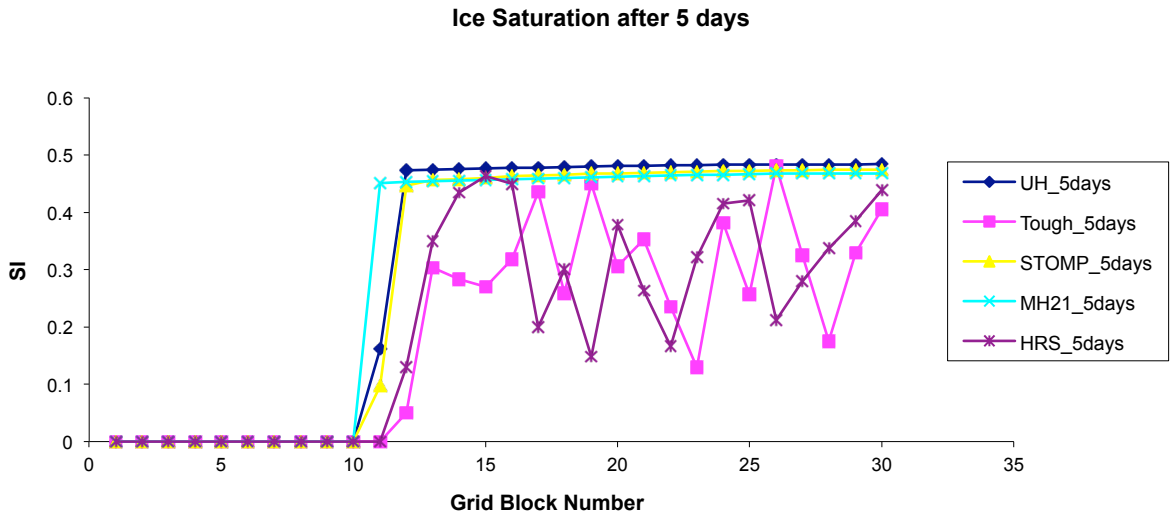

Figure 7.1.a.5. Comparison of hydrate saturation in Problem 3, part 3

Problem 4

Thermal Stimulation in Radial Coordinates

Problem 4 addresses thermal stimulation of a hydrate reservoir in 1D radial coordinates. The radial hydrate saturation distribution at several times show that all the plots almost fall on each when plotted against r^2/t. The results from our simulator matched with those from other simulators (not shown).

Conclusions

Our in-house simulator performs as well as the other simulators in the code comparison study. For Problem 3 with ice formation, our simulator, STOMP, and MH21 performed better than the other simulators.

Subtask 7.1b Transport property of hydrate bearing sediments

Introduction

Experimental data on multiphase flow properties of gas hydrate containing sediments is rarely available. Empirical correlations are often used for transport properties of sediments containing gas hydrates. In this work, we have developed mechanistic models for transport properties for hydrate bearing sediments. Hydrate deposition and dissociation is modeled in a single pore to develop pore-scale laws of hydrate occupancy. Pore size distributions are found for sediments containing different particle

size distributions. Pore size distribution is modified due to hydrate deposition. Percolation theory is used to numerically calculate effective transport properties at different hydrate and water saturations. The transport properties calculated from these mechanistic models can replace the empirical correlations in reservoir simulations of hydrate reservoirs.

Methodology

Porous medium generation

Shallow marine sediments are unconsolidated structures of sand, silt, and clays. We consider spherical particles with a Gaussian radius distribution. To generate the porous medium, particles are initially placed randomly in space confined by a rectangular cuboid of specific length, width and height. The dimensions of the cuboid are chosen such that about 30,000 particles can be conveniently placed inside. The particles are initially non-overlapping with zero initial velocity and are allowed to settle under gravity using discrete element method (DEM) (Cundall and Strack, 1979). The simulation is performed until all the particles have equilibrated with each other and their velocities are close to zero. The simulation gives the final position of the particles along with their respective radii. The pore throat and pore body size distributions and coordination numbers are calculated by Delaunay triangulation (Cignoni et al., 1998).

Transport property calculation

Percolation theory was used to calculate the transport properties (permeability, and relative permeabilities of wetting and non-wetting fluids) of the medium (Heiba et al. 1992, Heiba et al. 1984). We assume a Bethe network of pore throats. All the resistance to flow and the volume of the pore structure are assumed to be in pore throats. A coordination number of 5 is assumed for the present case. The flow rate through a single pore segment is given by:

$$q=g(\Delta P/\mu) \quad (1)$$

where q is the flow rate, g is the conductance, ΔP is the pressure drop and μ is the viscosity of the fluid flowing. The conductance distribution of the network is given by:

$$G(g)=(1-Q)\delta(g)+QG'(g) \quad (2)$$

where Q is the fraction of pores allowed and $G'(g)$ the probability that conductance of an allowed pore lies between g and $g+dg$. For phase j the conductance distribution is given by:

$$G(g)=(1-Q_j)\delta(g)+Q_jG_j'(g) \quad (3)$$

where Q_j is the fraction of pores allowed and $G_j'(g)$ the probability that conductance of an allowed pore lies between g and $g+dg$.

The relative permeability k_{rj} of phase *j* is calculated as:

$$k_{rj} = g_j / g0 \qquad (4)$$

where g_j is conductance of phase *j* and g0 absolute conductance of the network. Conductance for Bethe network for phase *j* is defined as:

$$g_j = -nC'(0) \qquad (5)$$

where *n* is coordination number of the Bethe network used. Function C(x) is solution of the following equation in Laplace form:

$$\int_0^\infty e^{-tx} C(x)dx = \frac{1-Q_j}{t} + Q_j \int_0^\infty \alpha_j^A \left|\frac{dr}{dg}\right| dg \left\{ \frac{1}{t+g} + \frac{g^2}{(t+g)^2} \int_0^\infty \exp\left(\frac{-gt}{g+t} x \right) [c(x)]^{n-1} dx \right\} \qquad (6)$$

where, Q_j is allowed fraction of pores for phase *j*, *g* is the conductivity of the pore structure, and α_j^A is the radius distribution of allowed pores for phase *j*. Absolute permeability is obtained when allowed fraction of pore is 1 and allowed radius distribution is the same as radius distribution of the network. The algebraic solution of the above equation to find *C'(0)* is given by Heiba et al. (1984). The relative permeabilities and the absolute permeability are calculated for the pore network.

Effect of Hydrate Saturation on Pore Structure: Hydrate deposition from flow of methane-saturated water was simulated in several cylindrical pores. This simulation showed that the hydrate saturation in a particular pore is independent of the size of the pore. The thickness of hydrate deposited on the wall is given by:

$$t_s = r\left(1 + \sqrt{1 - SH}\right) \qquad (7)$$

where, t_s is thickness of hydrate layer, *r* is the original radius of the pore and *SH* is hydrate saturation. New radius distributions are calculated for different hydrate saturations. Percolation theory is used with the new radius distribution to calculate the transport properties for a given hydrates saturation. A correlation dependent on hydrate saturation, wetting fluid (water) saturation and non wetting fluid (gas) saturation is developed for a particular radius distribution.

Results

Spherical particles of Gaussian radius distributions were packed using the DEM method. The pore throat radius distribution was determined after Delaunay triangulation. The pore throat distribution of the porous medium formed by the particles having Gaussian particle radius distribution is given by Rayleigh distribution. Table 1 shows the different distributions studied.

Particle size distribution		Radius distribution
Mean (μm)	Variance (μm)	σ (μm)
200	50	33.71
200	75	58.46
200	100	157.4
100	50	88.1
50	50	13.86

Figure 7.1.b.1 shows the water and gas relative permeabilities from percolation theory for the base case porous medium with zero hydrate saturation when σ for Rayleigh distribution is 157.

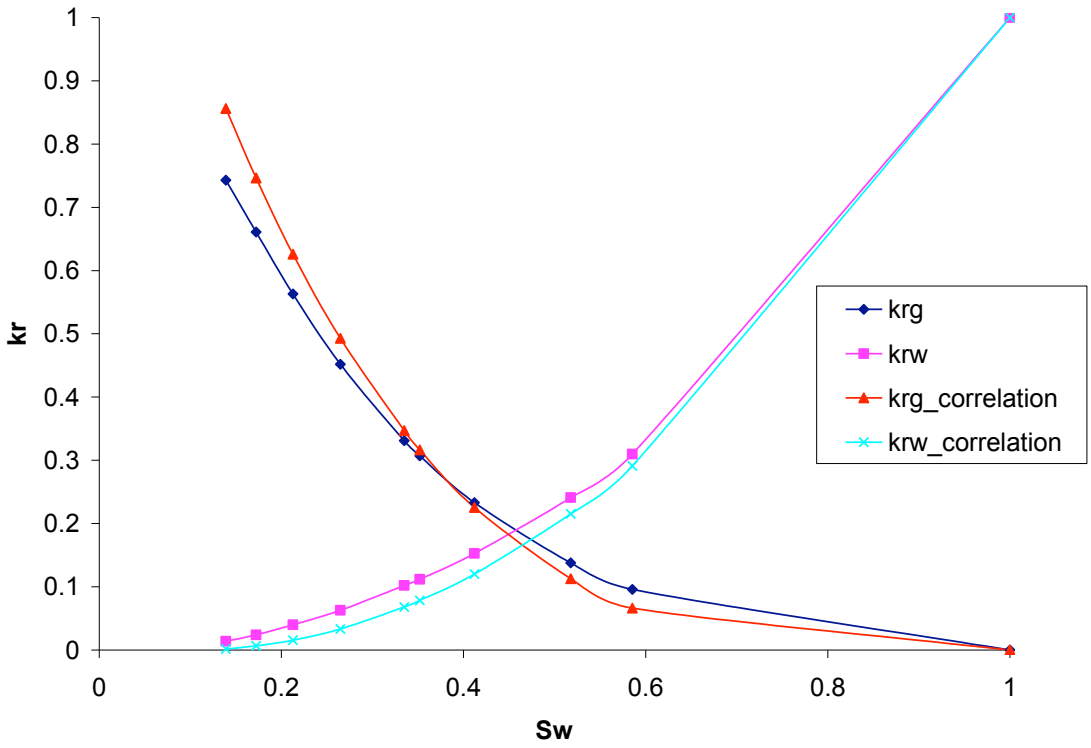

Figure 7.1.b.1. Relative permeability of the sediment without hydrate

The following correlation is developed for relative permeability by matching the results of the percolation theory:

$$k_{rw} = \left(\frac{S_w - S_{wr}}{1 - S_{wr}} \right)^2 \qquad (8a)$$

$$k_{rg} = \left(\frac{1 - S_w}{1 - S_{wr}} \right)^{3.5} \qquad (8b)$$

where k_{rw} is relative permeability of water or the wetting phase and k_{rg} is relative permeability of gas or the nonwetting phase.

Figure 7.1.b.2 shows the relative permeability obtained from percolation theory for the base case at different hydrate saturations. The curvature of relative permeability curves increase with increasing hydrate saturation.

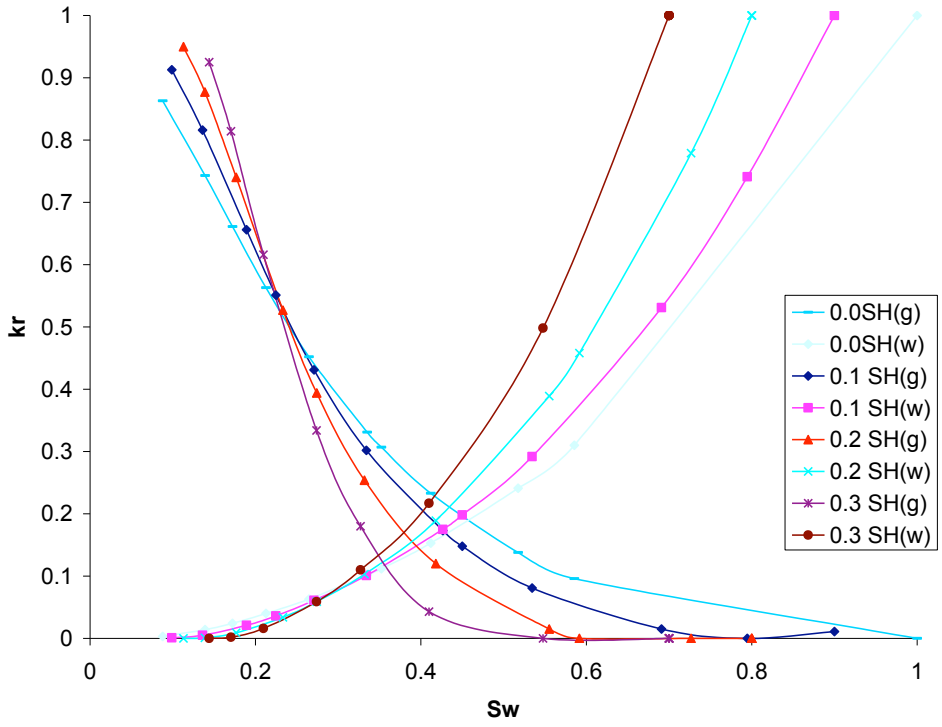

Figure 7.1.b.2(a): Relative permeability curves for different hydrate saturations

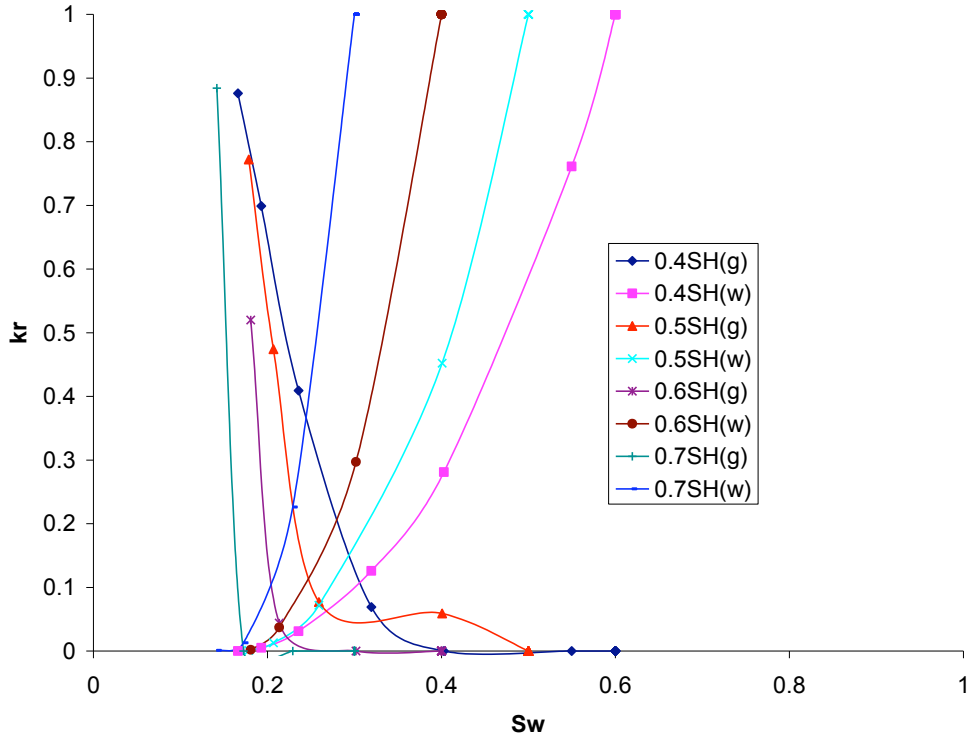

Figure 7.1.b.2(b): Relative permeability curves for different hydrate saturations

A correlation was developed between the computed relative permeability and hydrate saturation. The following correlation finds the best fit with the percolation theory results.

$$k_{rw} = \left(\frac{S_w - S_{wr}}{1 - S_H - S_{wr}} \right)^{(2+2S_H)} \qquad (9a)$$

$$k_{rg} = \left(\frac{1 - S_H - \beta S_w^{\alpha}}{1 - S_H - S_{wr}} \right)^{(3.5-S_H)} \qquad (9b)$$

$\alpha = 2,\ S_H \geq 0.5$

$= 1,\ S_H \leq 0.2$ (9c)

$= 3.25S_H + 0.425,\ 0.2 < S_H < 0.5$

$\beta = 10S_H - 1,\ S_H > 0.1$

$= 1,\ S_H \leq 0.1$ (9d)

Figure 7.1.b.3 shows comparison of relative permeability curves for 2 hydrate saturations (0.4 and 0.6) obtained from percolation theory and the correlations developed in Eq. (9).

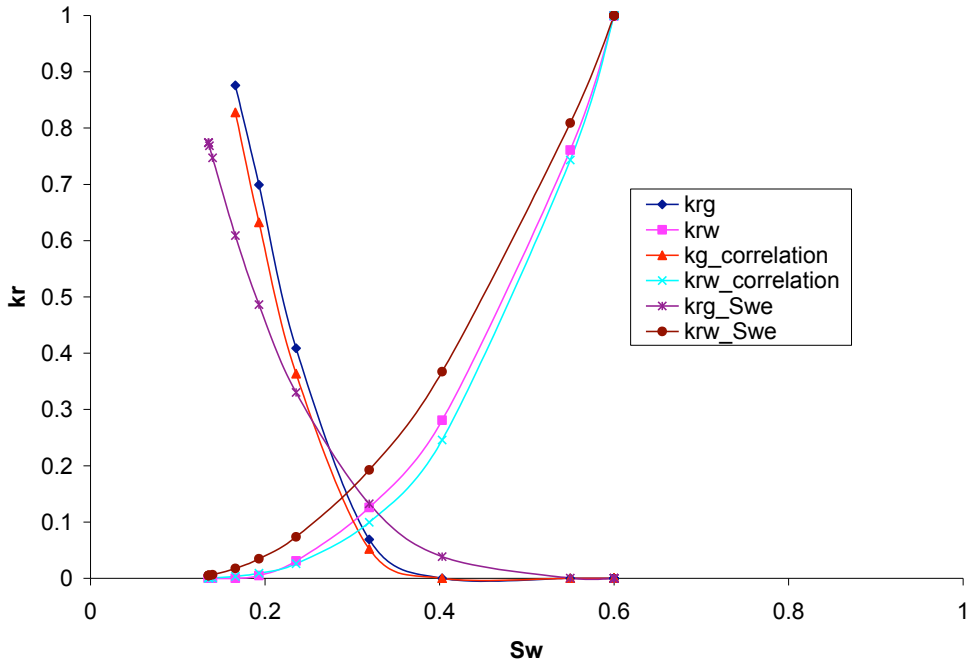

Figure 7.1.b.3(a): Relative permeability of the sediment for hydrate saturation 0.4

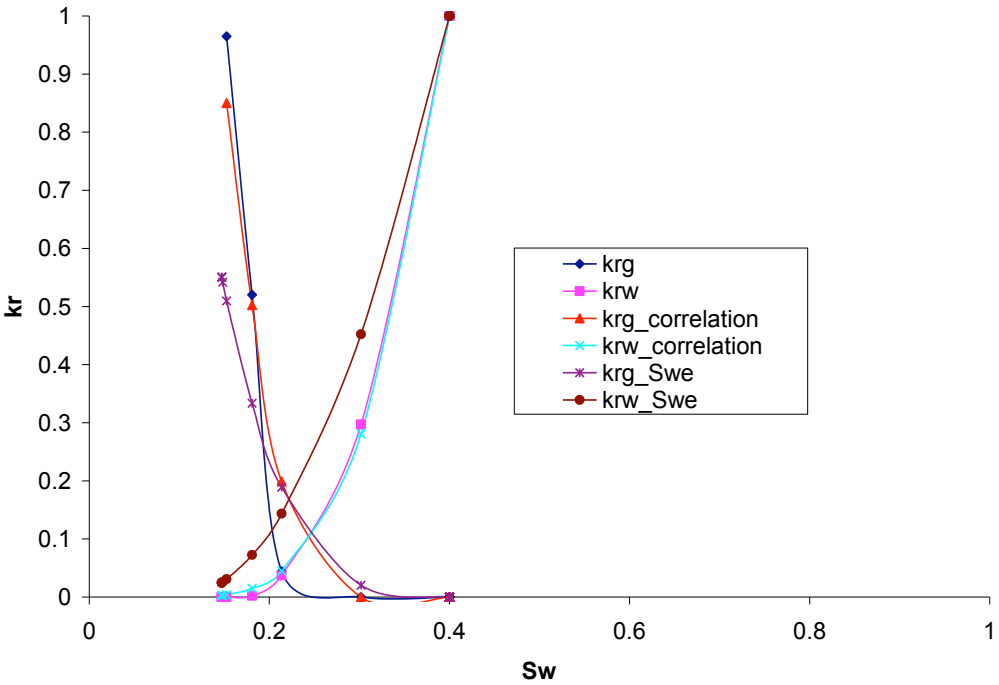

Figure 7.1.b.3(b): Relative permeability of the sediment for hydrate saturation 0.6

This shows that the correlation in equation 14 is valid for normal distribution of particle size which gives Rayliegh pore radius distribution.

Conclusions

- When hydrates deposit from a solubilized brine phase, hydrates deposit on walls of pore and pore-scale hydrate saturation is independent of size.
- Normal distribution of particle size of spherical sediments gives Rayleigh distribution of pore throat radius.
- For Rayleigh throat radius distribution, relative permeability matches Corey correlation with ng = 3.5 and nw = 2.
- With increasing hydrate saturation, the gas exponent ng decreases and water exponent nw increases.
- Using effective fluid saturations to calculate relative permeability in the presence of hydrates does not agree with calculated relative permeabilities.

Subtask 7.2a Strategy for gas production from confined hydrate reservoirs

Introduction

In this work, we are considering injection of warm water and depressurization for production from confined Class 2 hydrate reservoirs. The source of warm water could be a nearby oil reservoir or an underlying water aquifer. Gas production from a hydrate reservoir is studied through numerical simulation.

Approach

The numerical model used is a finite-volume simulator that takes into account heat transfer, multiphase fluid flow and equilibrium thermodynamics of hydrates. Four components (hydrate, methane, water and salt) and five phases (hydrate, gas, aqueous-phase, ice and salt precipitate) are considered in the simulator. Water freezing and ice melting are tracked with primary variable switch method (PVSM) by assuming equilibrium phase transition. Equilibrium simulation method is used here because kinetics of hydrate formation and dissociation are relatively fast in the field-scale. This simulator has been validated against several other simulators for the problems in the code comparison study conducted by US DOE.

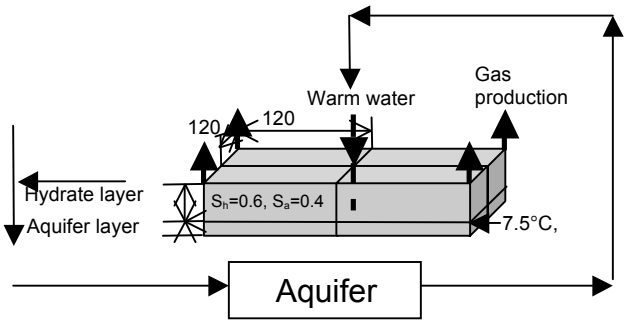

Figure 7.2.a.1: Domain considered for the base case

The objective of this study is to identify optimum production strategies for gas production from Class 2 hydrate reservoirs through numerical simulation. The domain selected as the base case is a quarter five-spot of size 120m x120m x10m (Figure 7.2.a.1). Initial temperature and pressure are assumed to be 7.5°C and 9MPa, respectively, which lie in the hydrate stable zone. The bottom 2m of the domain is an aquifer layer (S_A=1.0) and the top 8m is a hydrate layer with a hydrate saturation, S_H of 0.6 and aqueous saturation, S_A of 0.4. There is no heat and mass transfer though the side boundaries due to symmetry. There is only heat transfer, but no mass flow through the top and bottom boundaries due to impermeable shale layers. The effect of injection temperature, injection pressure and production well pressure on gas and water production is studied. The saturation histories encountered in these simulations will be modeled at the pore scale for transport properties.

Simulations were run for different injection pressures, injection temperatures and production pressures for 3000 days and total production of gas was compared for the above parameters.

For the case of no injection, the dissociation is due to pressure falling below the hydrate stable pressure due to depressurization at the production well. The heat of dissociation comes from surroundings, decreasing the temperature of the reservoir. Ice starts forming if the pressure goes below quadruple point pressure. After all the hydrates dissociate, the temperature again starts rising by the heat from surroundings.

For the case of warm water injection, the pressure of injection has to be higher than the reservoir pressure for the hot water to go in. The temperature rise is higher for higher temperature and higher injection pressure (injection flow rate increases). But if injection pressure is high the average pressure in the reservoir increases, slowing the dissociation of hydrates (and even formation of additional hydrates) before the warm water reaches a certain region. If production pressure and temperature are both high, the rate of production of gas increases. The total production of gas also depends on the production pressure, and for different production pressure the optimum injection conditions vary.

Figure 7.2.a.2 shows total production for the production well pressure of 2MPa. The injection temperature was kept constant at 20C and injection pressure was varied. The results were compared against the no injection or depressurization only case. When warm water is injected at a higher pressure but at a relatively low temperature (20C in the present case) the gas production rate decreases with increasing injection pressure. This is because the average pressure of the reservoir domain increases; dissociation of hydrate slows down. In case of 5MPa of injection pressure, the total production of gas increases because water occupies some pore space that would have been occupied by gas during depressurization. At higher injection pressure the hydrate dissociation is not complete in 3000 days. For low temperature water injection, only depressurization seems to be better than warm water injection.

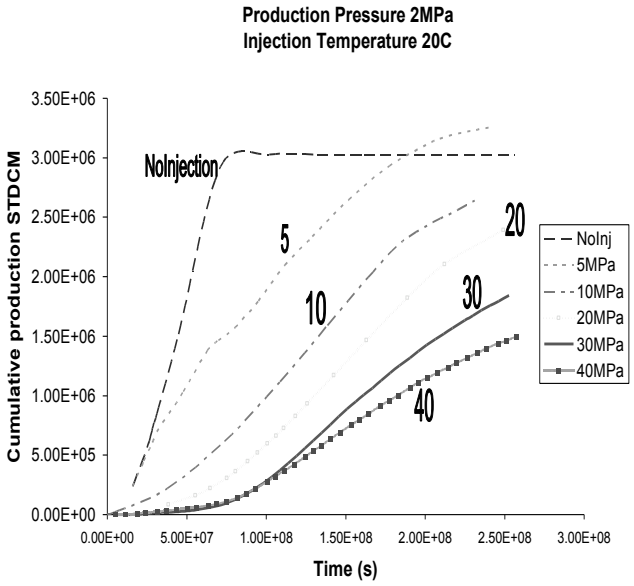

Figure 7.2.a.2: Cumulative production of gas with varying injection pressure, 20°C of injection temperature and 2MPa of production pressure

Figure 7.2.a.3 shows the cumulative production of gas when production well pressure is kept at 4MPa and injection temperature is 80°C. The injection pressure is varied. In this case, only depressurization is slow and does not dissociate all the hydrates present in 3000 days. With increasing injection pressure the gas production rate increases. With an injection water of 80°C, as the injection pressure increases more of the reservoir gets to this high temperature which helps hydrate dissociation.

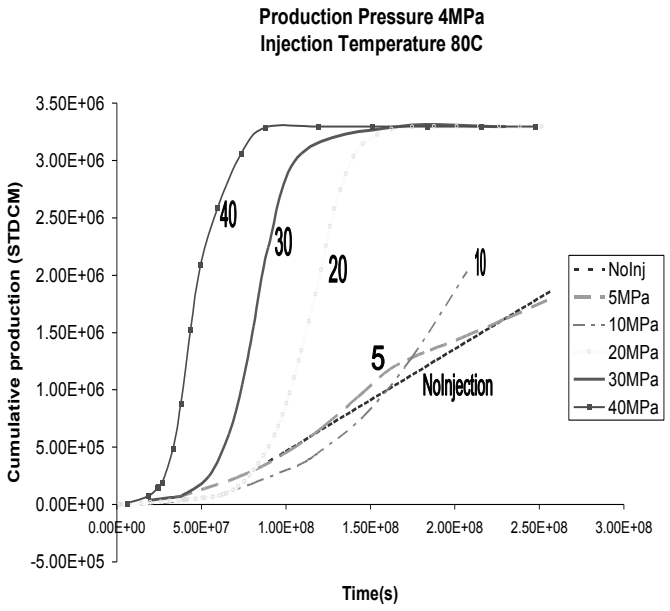

Figure 7.2.a.3: Cumulative production of gas with varying injection pressure at 80°C of injection temperature and 4MPa of production pressure.

If injection temperature is in medium range (50°C) then injection pressure and production pressure play an important role. Figure 7.2.a.4 and 7.2.a.5 are plots for 2MPa and 4MPa of production pressure, respectively, at 50°C of injection temperature with varying injection well pressures. If Injection pressure rises from 5MPa to 10MPa the production almost remains same for the case of production pressure 2MPa but decreases drastically in the case of production pressure 4MPa. This can be attributed to higher average pressure in the reservoir domain, which hinders hydrate dissociation. In case of injection pressure of 30MPa and 40MPa the total production and rate of production increases (Figure 7.2.a.4 and 7.2.a.5), though initial rate of production falls due to increase in average reservoir pressure, which assists hydrate formation while temperature is still not high. The gas production rate is non-monotonic with the increase in injection pressure.

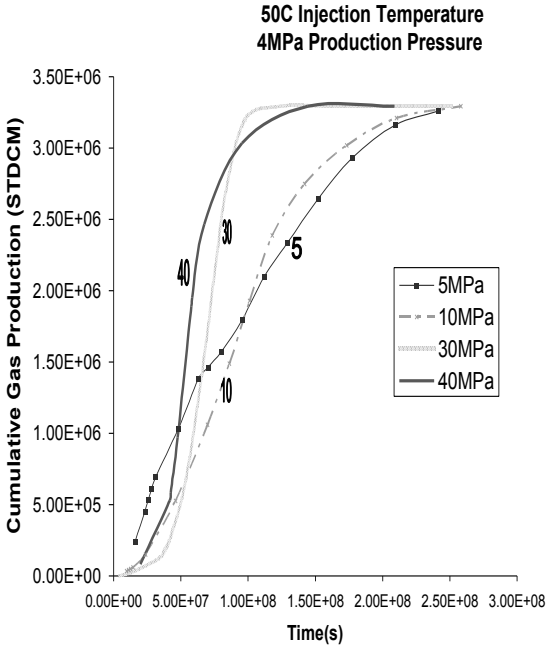

Figure 7.2.a.4: Cumulative gas production with varying injection pressure and 2MPa of production pressure and 50°C of injection temperature.

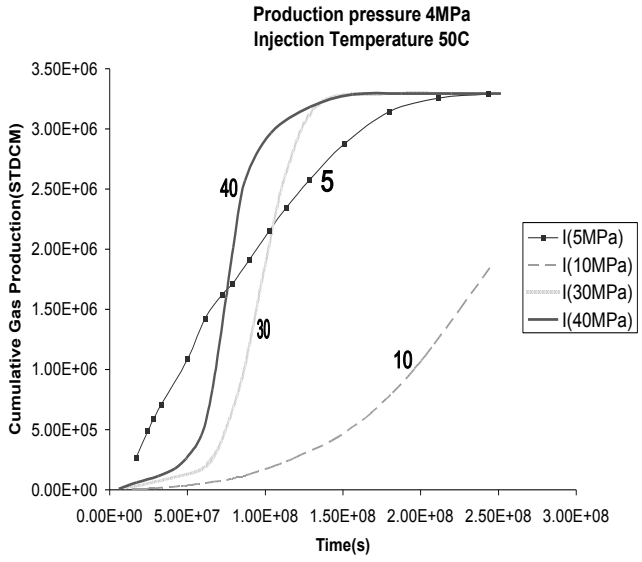

Figure 7.2.a.5: Cumulative gas production with varying injection pressure and 4MPa of production pressure and 50°C of injection temperature.

Conclusions

For warm water injection, production well pressure, injection temperature and pressure play an important role in the production of gas from hydrate deposits. For high injection temperature, the higher pressure increases the flow of warm water (heat) in the reservoir making the production rate faster, but if injection temperature is not high then only depressurization is the best method of production. At intermediate injection temperature, the production rate changes non-monotonically with the injection pressure. These parameters should be chosen carefully to optimize recovery and recovery rate of gas.

Subtask 7.2b Strategy for gas production from unconfined hydrate reservoirs

Introduction

In this study, we consider reservoirs with a limited aquifer. We assume that the un-confinement of the aquifer is not at the bottom but on one side of the aquifer. For the limited aquifer case we study only horizontal wells, and that makes the reservoir translationally symmetric. So, for this case we study the reservoir in 2 dimensions but the total amount of hydrates and hydrate to water ratio are same as in our previous case of unconfined reservoir. The initial conditions and rock properties are the same as in the previous case. The injection well conditions are also same with injection pressure of 50MPa, and injection temperature of 50°C. Production well pressure is 4MPa. Circle shows the producer and X shows the injector in the figures.

Reservoir description

We consider a hydrate block similar to the block AC 818 in the Gulf of Mexico. The block is a 1200m long and 500m wide reservoir, as shown in Figure 7.2.b.1. It has an 18m thick hydrate layer which is underlain by an infinite aquifer. In the hydrate zone, hydrate saturation is 0.75 and water saturation is 0.25. Initial pressure at the bottom of the reservoir is 31.4MPa and initial temperature is 294.88K which vary in the reservoir according to hydrostatic pressure drop and geothermal gradient, respectively. To model the infinite aquifer a 12m thick aquifer zone is considered for simulation in which the bottom most 3m layer was assumed to have a permeability $1/10^{th}$ of the hydrate layer absolute permeability. The water saturation is 1.0 for the aquifer layer. For over-burden, no mass flow is allowed while heat can transfer with a specified heat transfer coefficient. At the under-burden, we have an infinite aquifer, so, heat transfer is allowed and the pressure is specified at the bottom boundary. The water can come into the reservoir or go out according to the pressure difference between the bottom most grid layer and the boundary pressure. For lateral boundaries no heat or mass flow is considered, due to symmetry.

Results

Horizontal reservoir

Figure 7.2.b.1 shows the well configurations we study for the horizontal reservoirs. The bold line at the bottom shows the un-confinement where constant pressure condition is maintained. The pressure maintained is equal to the initial pressure of the reservoir. Water can flow in or flow out of the reservoir depending on the difference between reservoir pressure and boundary pressure at un-confinement. The under-burden in this case is an impermeable shale layer so no mass flow boundary condition is applied. The horizontal wells are in perpendicular direction to the face shown in the figure.

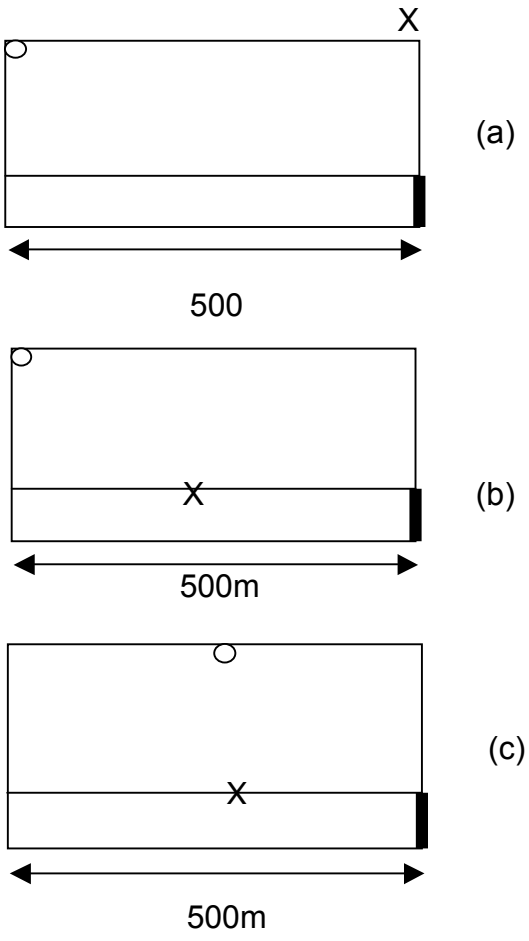

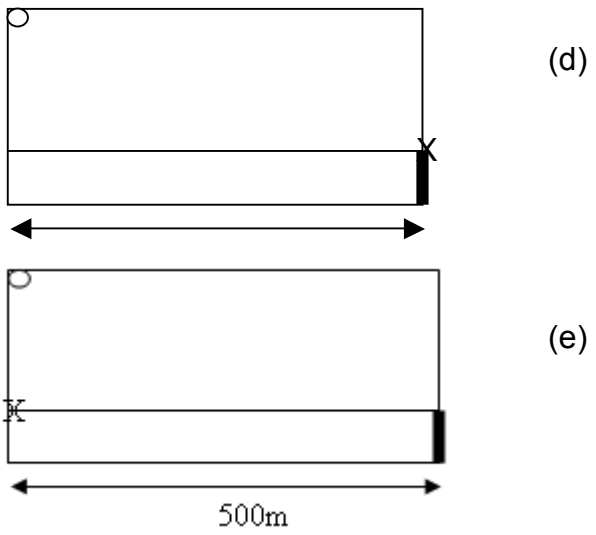

Figure 7.2.b.1: Schematic of 2-d reservoir showing (a) 'injector_up_producer_up', (b) 'injector_downmid_producer_up', (c) 'inline_mid', (d) 'opposite' and (e) 'inline_side'

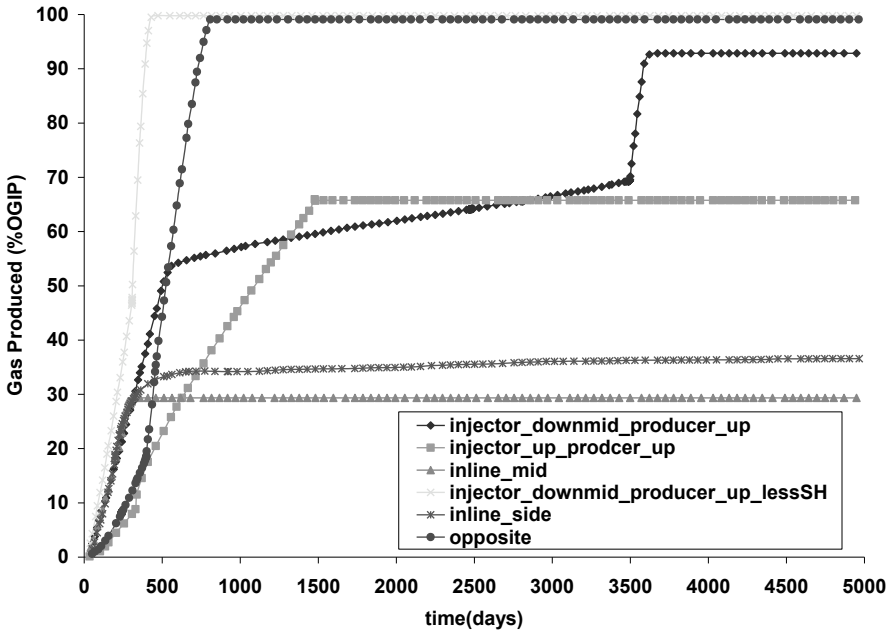

Figure 7.2.b.2: Production curves for different well configurations

First we compare the two cases with different hydrate saturations for which the well configuration is shown in Fig 7.2.b.1(b). If hydrate saturation is low then the permeability of hydrate bearing layer is high and the mobility of the fluids in the hydrate bearing layer is high. Hence the flow of the injected water is high in the low hydrate saturation (0.6) case and gas is produced at a high rate. Figure 7.2.b.2 shows the cumulative production of gas. Also less heat is needed to dissociate less amount of hydrate in the same pore volume. Figure 7.2.b.3a shows the in-situ profiles for high hydrate saturation

case ‘injector_downmid_producer_up’. Initially all the hydrates on the right of the injection well are dissociated (Figure 7.2.b.3a). Due to presence of the un-confinement on the right side in the aquifer we are able to maintain a pressure drop on the right side so water is flowing and is dissociating hydrate.

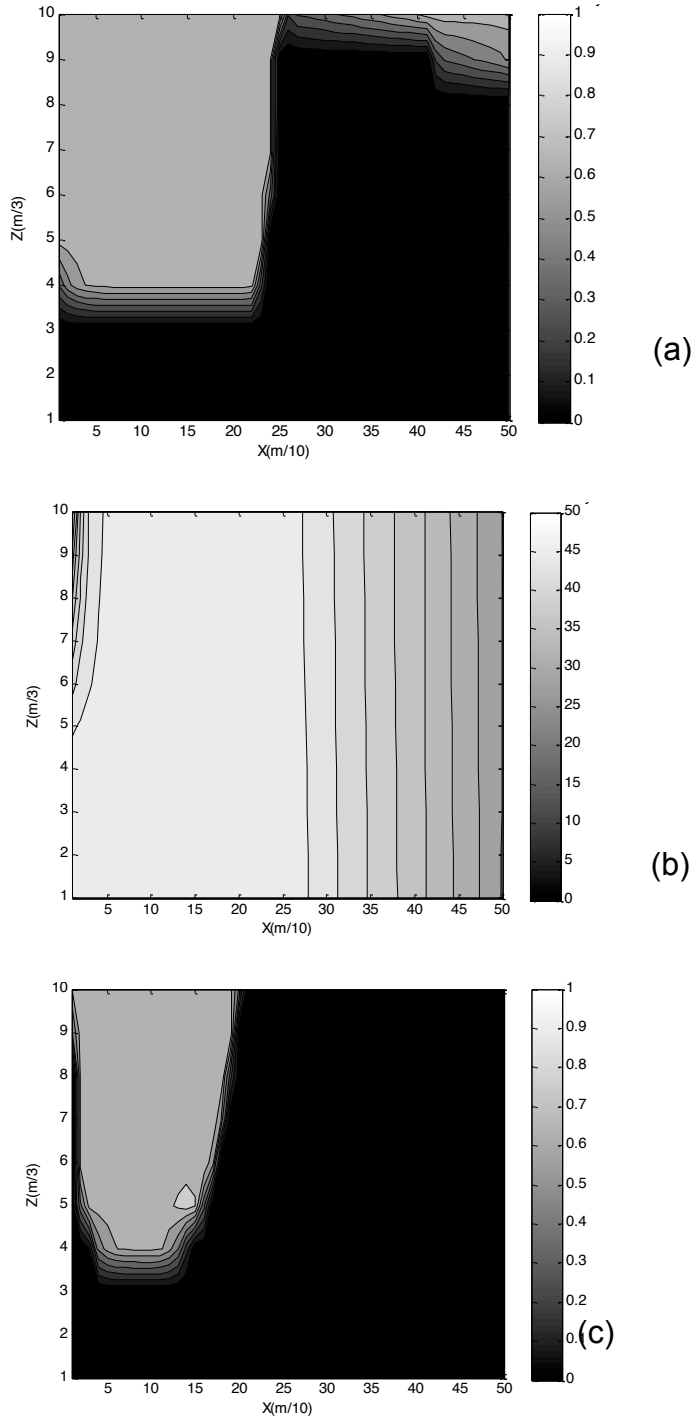

Figure 7.2.b.3 (a) Hydrate saturation profile after 450 days (b) pressure profile after 450 days (c) hydrate saturation profile after 3300 days for ‘injector_downmid_producer_up’

On the left side the pressure in the aquifer zone is almost same and hence no water flow towards left (Figure 7.2.b.3b). The production well is not able to depressurize a whole lot due to high hydrate saturation leading to low permeability. When all the hydrates on the right side of the injection well have dissociated the gas production rate decreases as the hydrate dissociation rate on the left side is very slow. After about 3500 days some hydrate dissociates on the left most boundary and a water channel forms to the production well (Figure 7.2.b.3c). This increases the flow of warm water through the channel in the left direction and hence an increase production rate is seen after 3500 days. But still we are not able to recover 100% of OGIP in 5000 days because some of the hydrates on the top left side are bypassed by formation of the channel.

Due to formation of water channel in the cases ‘inline_mid’ and ‘inline_side’ warm water flows from injector to producer bypassing most of the hydrates. Figure 7.2.b.4(a) and (b) shows the hydrate saturation profile after 5000 days for the case ‘inline’ and ‘inline_side’ respectively, showing water channel formation. In these cases injector and producer are very close to each other; so we produce only 30-35% of original gas in place.

In the case when injector and producer both are on the top of the hydrate bearing layer ‘injector_up_producer_up’ the injection is very difficult in the hydrate layer. But the aquifer un-confinement is limited to only one side so we are able to depressurize the reservoir slowly. Figure 7.2.b.4(c) shows the in-situ profile of hydrate saturation after 5000 days for this case. A lot of hydrates are left undissociated.

In the case named ‘opposite’, we are able to take advantage of both warm water flooding as well as depressurization as the wells are far apart. In this case no channel is formed due to large distance between the wells. Figure 7.2.b.4(d) shows the hydrate saturation profile after 200 days showing the depressurization and warm water flooding effect.

For the horizontal reservoirs where the aquifer is limited, the depressurization helps and the above study shows that it is better to keep the injector and producer at a horizontal distance so that water channel does not form to bypass the hydrate bearing sediments. Injector near the aquifer helps to transfer heat due to high permeability of aquifer zone. High hydrate saturation also affects the mobility of the fluids; depressurization is more effective when hydrate saturation is low in the sediments.

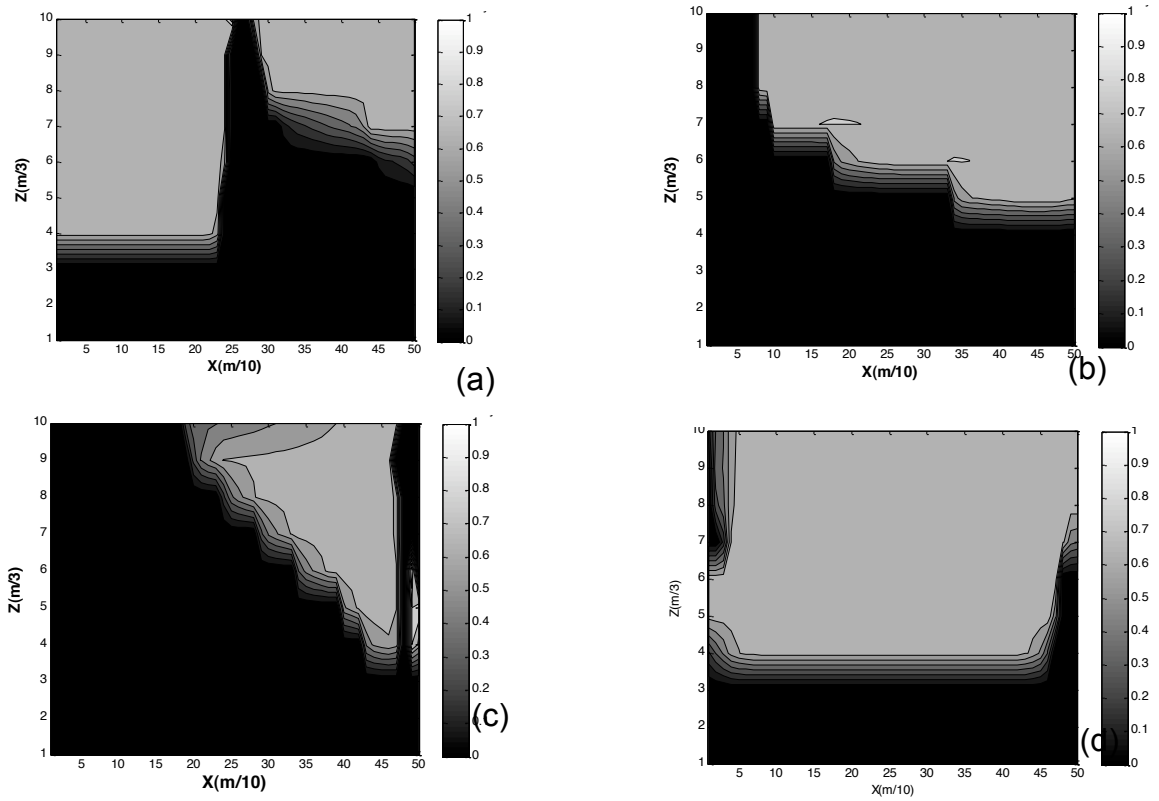

Figure 7.2.b.4: Hydrate saturation profile (a) after 5000 days for the case 'inline', (b) after 5000 days for the case 'inline_side', (c) after 5000 days for the case 'injector_up_producer_up' and (d) after 200 days for 'opposite'

Dipping reservoirs

To study the effect of dip (18°) and to find the optimum well configuration for dipping unconfined reservoirs with limited aquifer, we study configurations shown in Figure 7.2.b.5.

In the dipping reservoirs, the over-burden and under-burden are impermeable shale layers. The ratio of initial hydrate to water is same as in the horizontal reservoir. The reservoir is unconfined along the depth and a pressure boundary condition is applied to model the limited aquifer. Gas rises due to gravity so the production well has to be at the top of the reservoir. From the simulation of horizontal reservoirs, we found that warm water injection helps when the injection well is near to the limited aquifer, as mobility of water is higher in the aquifer. Using this information we try two limiting cases of injection well on the water hydrate contact boundary. In the case 'production_top_injection_top' the injection well is near overburden while in the case 'production_top_injection_bottom' the injection well is near underburden. For dipping the reservoir, we try depressurization in the 'no_injection' case.

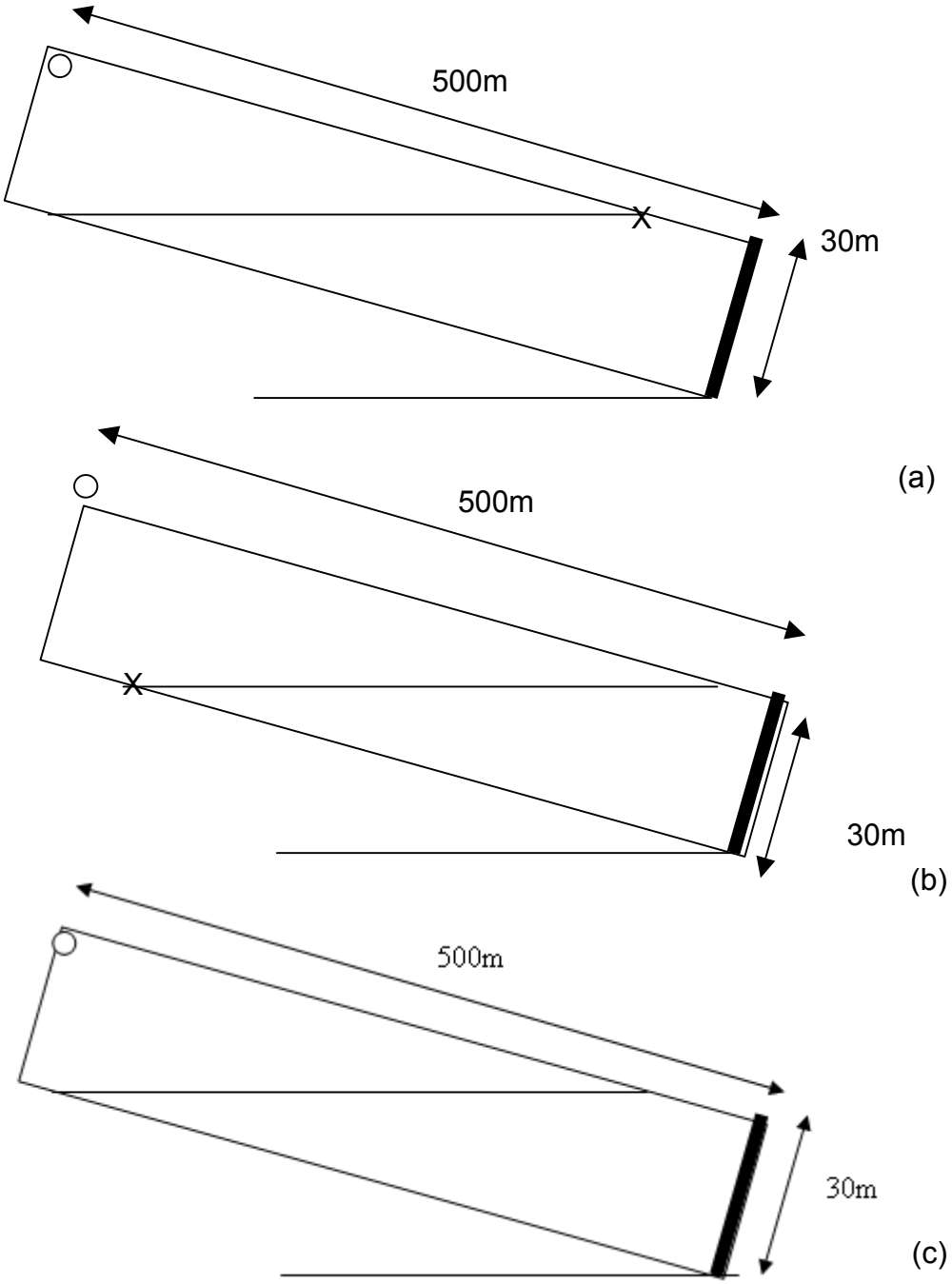

Figure 7.2.b.5: Dipping hydrate reservoir (a) 'production_top_injection_top', (b) 'production_top_injection_bottom' and (c) 'no_injection'

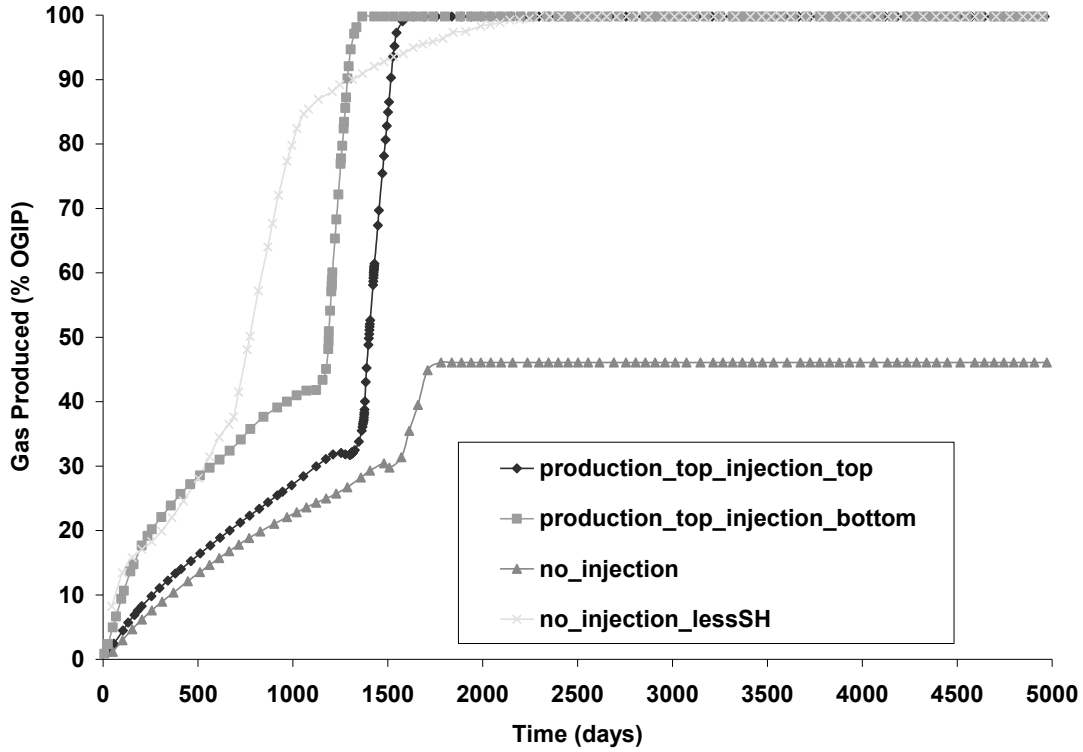

Figure 7.2.b.6: Cumulative gas production for dipping reservoir

Figure 7.2.b.6 shows the cumulative gas production using different well configurations. The production curves for the cases 'production_top_injection_top' and 'production_top_injection_bottom' are comparable. In both these cases initial production is due to depressurization at the production well. Figure 7.2.b.7 shows the hydrate saturation profiles after 1200 days for both the cases. For the case 'production_top_injection_top' the depressurization front is about to reach the aquifer layer after which the production rate increases. In the case 'production_top_injection_bottom' the depressurization dissociation from has reached the aquifer and the warm water flow becomes easy after that in the hydrate bearing zone and hence the production rate increases.

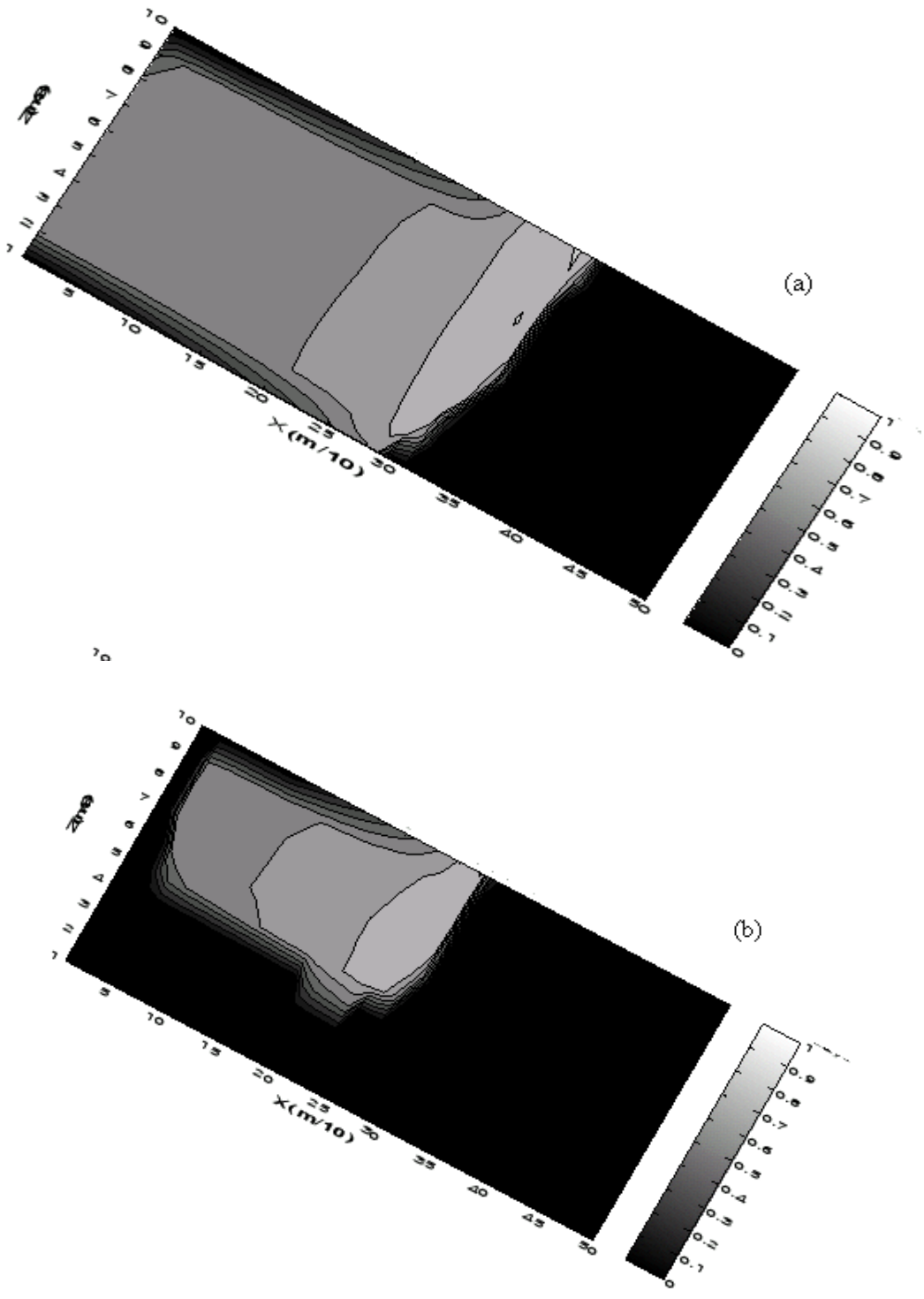

Figure 7.2.b.7: Hydrate saturation profile after 1200 days for (a) ‘production_top_injection_top’and (b) ‘production_top_injection_bottom’

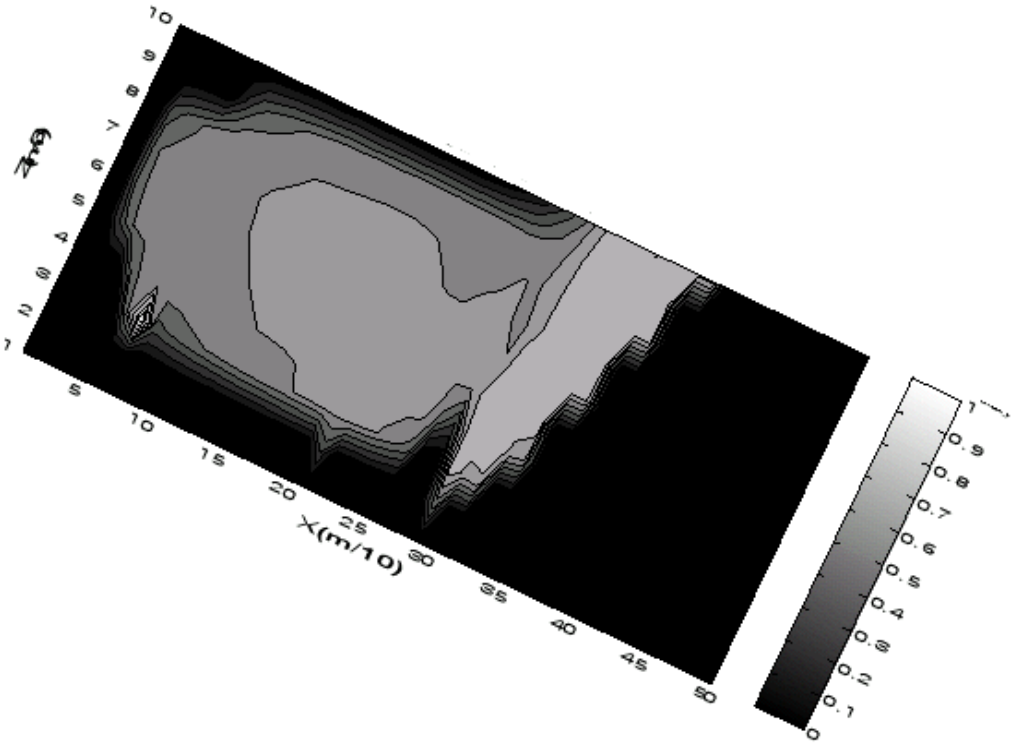

Figure 7.2.b.8: Hydrate saturation profile after 5000 days for 'no_injection'

In the 'no_injection' case initially the production is similar to the other two cases till the depressurization front reaches the aquifer. But in the no injection case no warm water is available to heat the reservoir. The channels of water zone formed along the perifree bypass the hydrate bearing zone due to its low permeability and production stops after 45% of OGIP is produced. Figure 7.2.b.8 shows the hydrate saturation profile after 5000 days.

When the saturation of hydrate is low, then depressurization is effective as the permeability of hydrate bearing zone is not as low as in the case of 0.75 hydrate saturation. So, in the low hydrate saturation case 'no_injection_lessSH' we are able to produce 100% of the original gas in place.

For dipping reservoirs, depressurization is not effective in limited aquifer if the hydrate saturation is high. The cumulative production and production rates are similar if the injection well is on the hydrate water contact zone.

Conclusions

Three types of reservoirs have been studied to find the optimum production strategy for different conditions. For the horizontal reservoir if the aquifer attached is at the under-

burden and large then depressurization is ineffective. The injection well should be near the aquifer zone for the mobility of the water injected. The position and the orientation of the production well are not that important as the production is due to thermal stimulation by warm water injection. Horizontal wells are better as they increase the area of warm water reach. More injection wells can be used for increasing the production rate and cumulative production for a field.

When the aquifer is limited and on the down dip side of the reservoir, the reservoir can be depressurized but the warm water injection is necessary for high production rate. Aquifer helps to mobilize the hot water injected. For limited aquifer case, the distance between the injection and production well should be increased so that water channel bypassing the hydrate bearing sediments does not form.

When we have a dipping formation the production well should be at the top and the injection well should be on the contact of hydrate and water zones for optimum production.

Thus in all the cases discussed, the injection well should be on the contact of hydrate and water zones for high production rate, the production well should be on the top of the hydrate bearing layer. The distance between the production well and the injection well should be optimized based on the hydrate saturation and the aquifer size.

Subtask 7.2c Gas production from heterogeneous reservoirs

Introduction

In previous studies, we had assumed that the hydrate reservoirs are homogeneous. In this section, we assume hydrate layers of different initial hydrate saturation and permeability. Warm waterflooding is simulated and the gas production is computed.

Reservoir description

We consider a hydrate block similar to the last section except for the heterogeneity. The block is a 1200m long and 500m wide reservoir, as shown in Figure 7.2.c.1. It has an 18m thick hydrate layer which is underlain by an infinite aquifer. The hydrate zone has two layers each 9 ft thick. The top hydrate zone has a porosity of 0.28, permeability of 100 md and a hydrate saturation of 0.2. The bottom hydrate zone has a porosity of 0.39, a permeability of 1000 md and a hydrate saturation is 0.8. Initial pressure at the bottom of the reservoir is 31.4MPa and initial temperature is 294.88K which vary in the reservoir according to hydrostatic pressure drop and geothermal gradient, respectively. The dipping reservoir is assumed to be the same as the last section except for the two hydrate layers as shown in Figure 7.2.c.2.

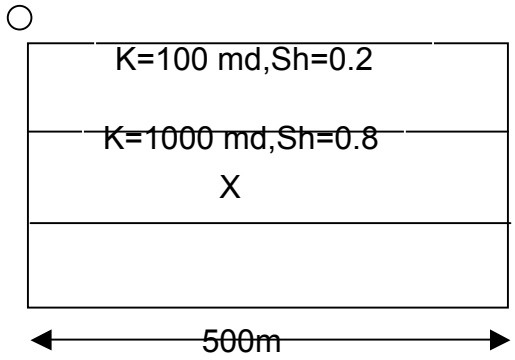

Figure 7.2.c.1(a): Schematic of 2-d reservoir showing 'injector_downmid_producer_up'

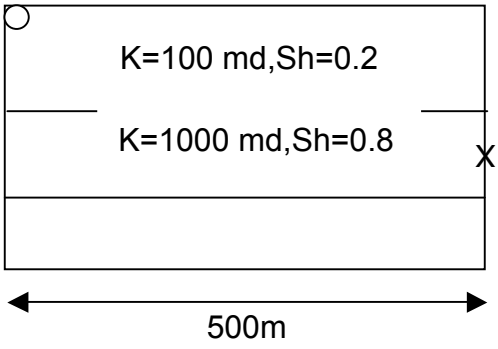

Figure 7.2.c.1(b): Schematic of 2-d reservoir showing 'injector_down_producer_ up'

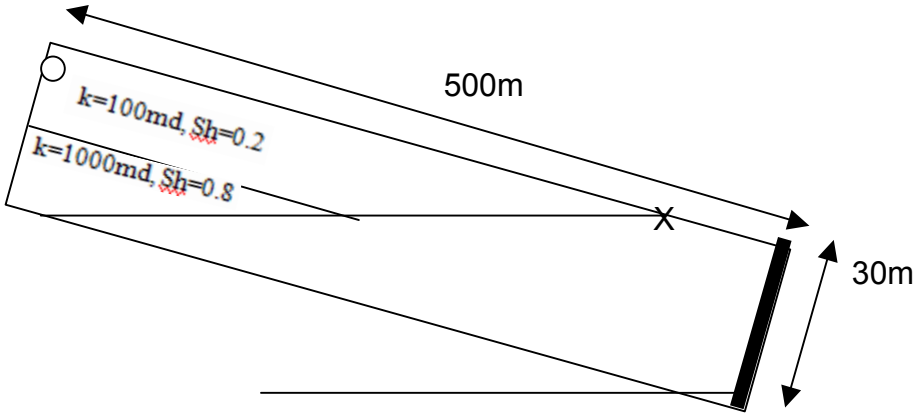

Figure 7.2.c.2(a): Dipping hydrate reservoir 'production_top_injection_top'

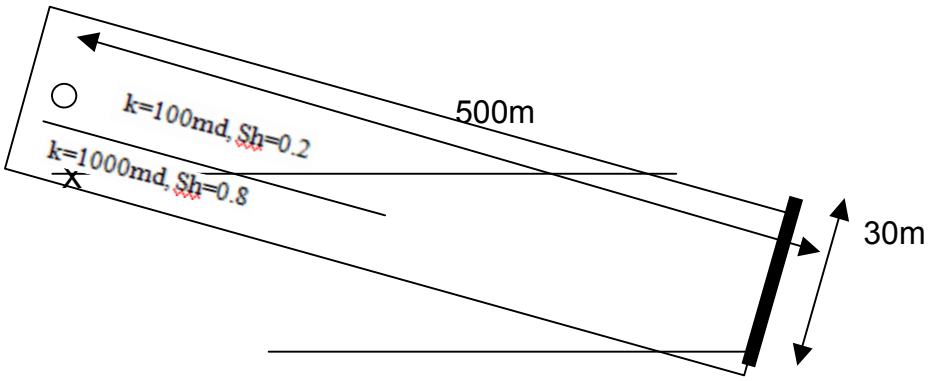

Figure 7.2.c.2(b): Dipping hydrate reservoir ‘production_top_injection_bottom’

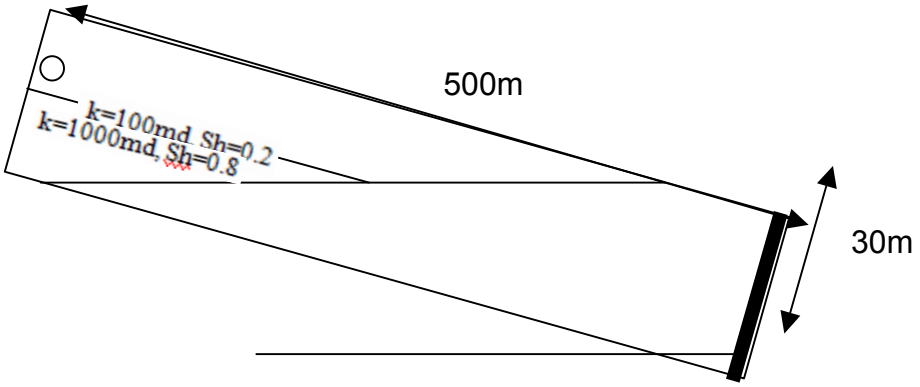

Figure 7.2.c.2(c): Dipping hydrate reservoir ‘no_injection’

Results

Horizontal reservoir

Figure 7.2.c.3 shows the effect of heterogeneity on gas production. Both the simulation results are for the well configuration “Injector downmid Producer up” shown in Figure 7.1.c.1(a). The homogeneous case corresponds to the homogeneous reservoir discussed in the last section. The amount of hydrate is not the same in both the cases; thus gas produced is plotted as the % of the original gas in place. The gas production is faster in the heterogeneous case because the higher permeability sediment gets flooded first, but the heat from the higher permeability warms the hydrate in the lower permeability zone. Also, there is less hydrate in the lower permeability layer than the high permeability layer.

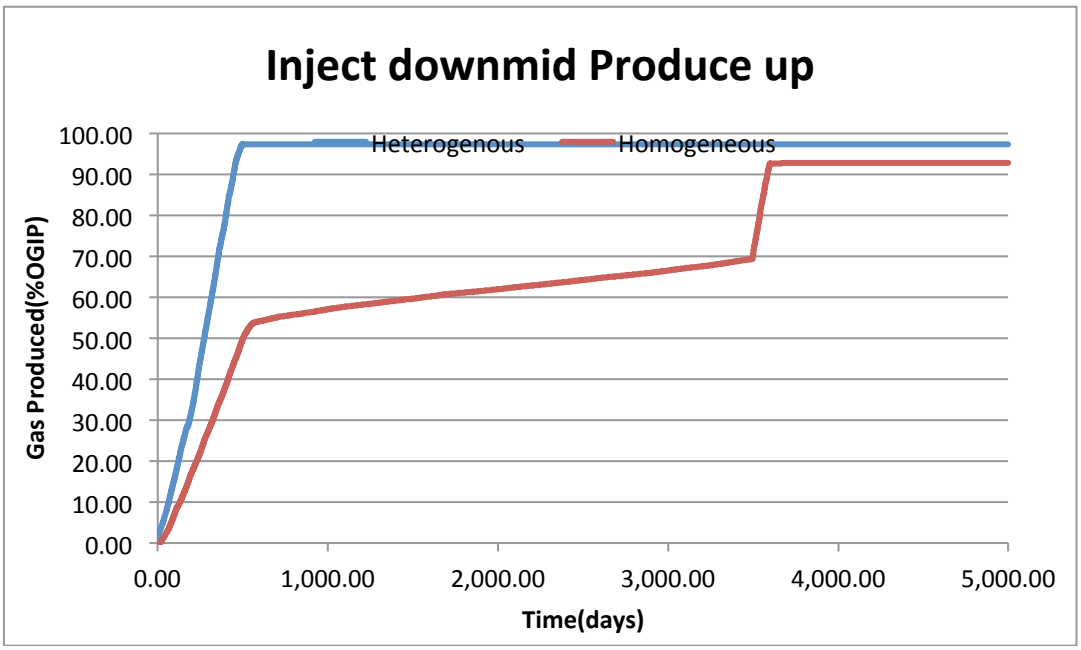

Figure 7.2.c.3: Gas production for homogeneous and heterogeneous 'inject downmid produce up' reservoir

Figure 7.2.c.4 shows the effect of heterogeneity on gas production. Both the simulation results are for the well configuration "Injector down Producer up" shown in Figure 7.1.c.1(b). In this case, the injector is not close to the aquifer. Thus the injectivity of the well is low for a long time especially for the heterogeneous reservoir and thus the gas production is low.

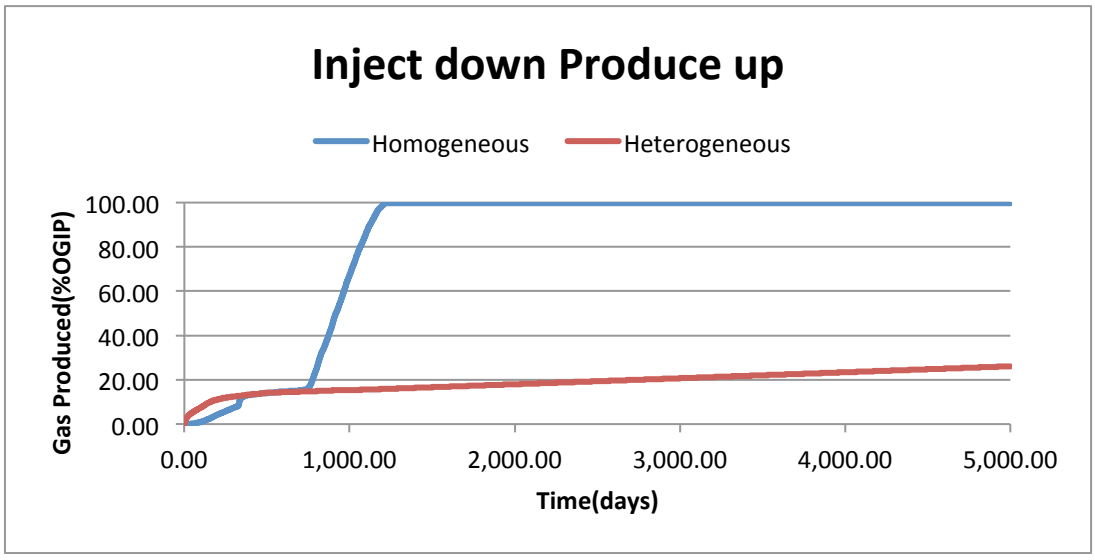

Figure 7.2.c.4: Gas production for homogeneous and heterogeneous 'inject down produce up' reservoir

Dipping reservoir

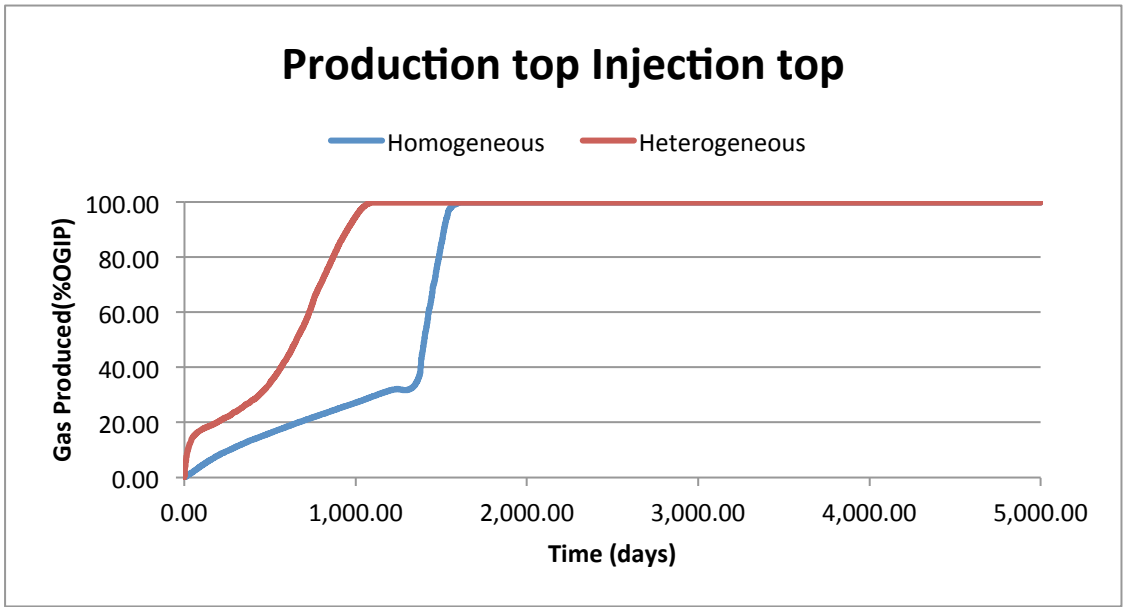

Figure 7.2.c.5: Gas production for homogeneous and heterogeneous 'produce top inject top' reservoir

Figure 7.2.c.5 shows the effect of heterogeneity on gas production in dipping reservoirs. Both the simulation results are for the well configuration 'production_top_injection_top' shown in Figure 7.1.c.2(a). The gas production in the heterogeneous reservoir is faster than that in the homogeneous reservoir. Figure 7.2.c.6 shows the effect of heterogeneity on gas production for 'production_top_injection_bottom' configuration. Again the gas production is faster for the heterogeneous reservoir. The heterogeneity improves the heat transfer and increases the gas production.

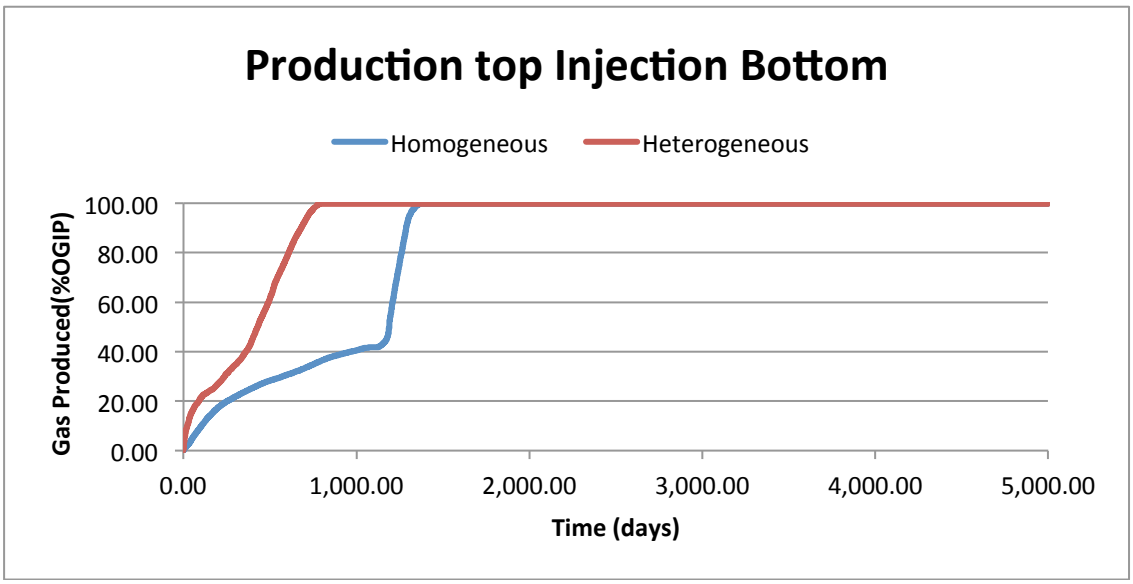

Figure 7.2.c.6: Gas production for homogeneous and heterogeneous 'produce top inject bottom' reservoir

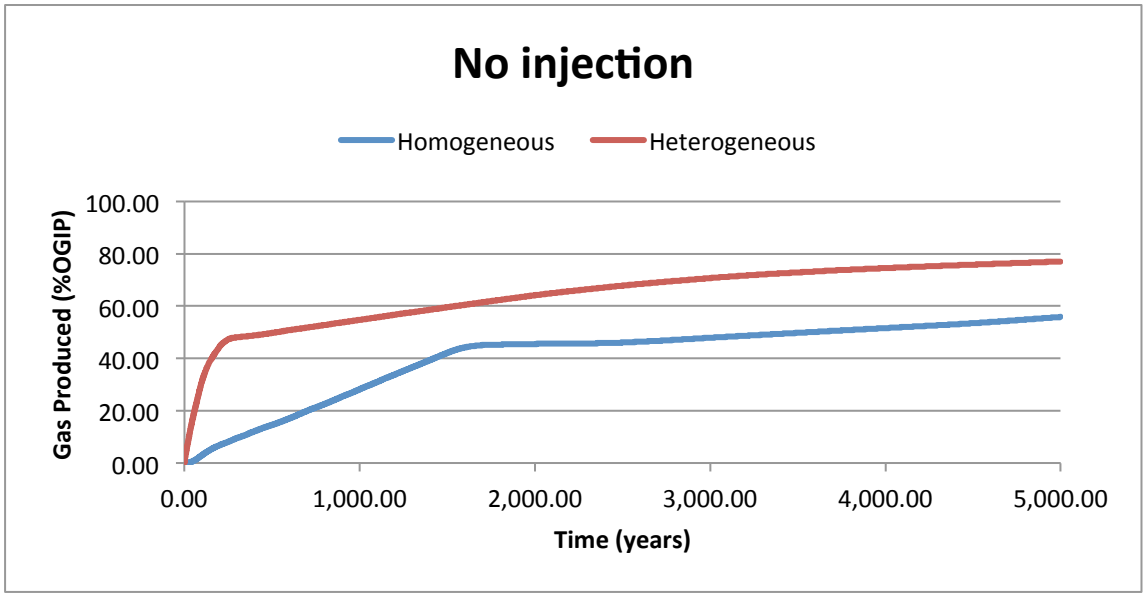

Figure 7.2.c.7: Gas production for homogeneous and heterogeneous 'no injection' reservoir

Figure 7.2.c.7 shows the effect of heterogeneity on gas production for depressurization in dipping reservoirs. Again the gas production is faster for the heterogeneous reservoir for depressurization.

Conclusions

The effect of heterogeneity is studied for warm water injection and depressurization. In most cases, the gas production is faster in heterogeneous reservoirs. The heat transfer is enhanced because of faster flow in the higher permeable zones.

Subtask 7.2d CO_2 injection

Introduction

In previous studies, we have shown that depressurization is ineffective in unconfined reservoirs; warm water injection is effective and horizontal wells are more effective than vertical wells (Phirani et al., 2009, 2009a). In this study, we consider CO2 injection into methane hydrate reservoirs to release methane and sequester CO2.

Numerical model

Five components (methane, carbon dioxide, water, methane-hydrate, CO_2-hydrate) and six phases (gas phase, aqueous phase, liquid CO_2-rich phase, ice, methane-hydrate, CO_2-hydrate) are considered in the simulator. For the conversion of gas (carbon dioxide or methane) and water to the respective gas-hydrate or vice versa, pressure-temperature phase diagram is used. The fraction of CO_2 and methane in gas and liquid phases is calculated using the Peng-Robinson equation for the two phases. The component fraction of the gases in the aqueous-phase and the water in the gas-phase is calculated using the solubility functions (Carroll and Mather, 1999).

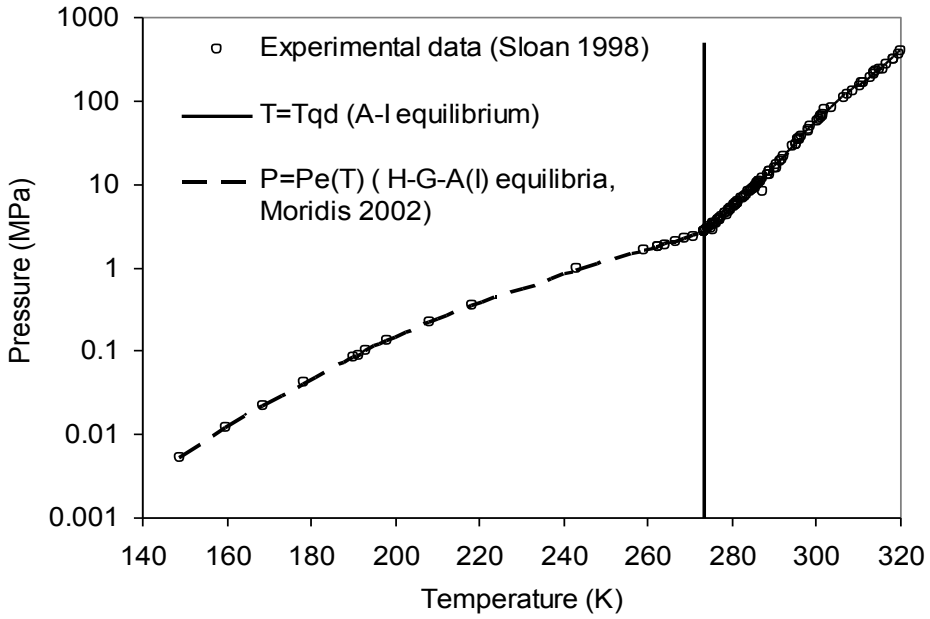

Figure 7.2.d.1: Equilibrium curve for methane hydrate stability zone

Methane-hydrate phase diagram

Figure 7.2.d.1 shows the pressure-temperature diagram for methane-hydrates (Sloan, 1998). The two important curves shown in the figure are the gas-hydrate equilibrium curve (P_{em}-T curve, where P_{em} is the equilibrium pressure for the methane-hydrates and T is the temperature) and the water-ice equilibrium curve (vertical line). For the phase boundary between the aqueous and the ice phases, the pressure effect on the freezing (melting) temperature is negligible under typical hydrate conditions (Sloan, 1998), and therefore it is approximated by the vertical straight line T = 273.2 K. The intersection of the gas-hydrate and the water-ice equilibrium curve is called the quadruple point. Above the gas-hydrate equilibrium curve (higher pressure), methane can exist as a hydrate and below the curve methane exists as a gas. Similarly, on the right side of the vertical line, the water is stable in liquid form and on the left in the solid form. Three phases can coexist on the equilibrium curve for the methane-hydrate system. If the pressure and temperature conditions lie on the equilibrium curve, gas-ice-hydrate can exist on the left side of the vertical line and water-gas-hydrate on the right. At the quadruple point (273.2 K), all the four phases can co-exit. In the present work, the correlation between P_{em} (equilibrium pressure) and T (temperature) for a salt-free system is represented with the regression formulas obtained by Moridis (2003) by fitting the experimental data reported by Sloan (1998).

In the present work, a thermodynamic equilibrium is assumed between the aqueous and ice phases. There is no kinetic barrier to the phase transition between the aqueous-phase and the ice-phase. But hydrate formation and dissociation are considered to be kinetically controlled. Thus meta-stable methane-hydrate can exist in the gas stable zone and meta-stable gas can exist in the presence of water in the hydrate stable zone. The assumption of the equilibrium between the aqueous-phase and the ice-phase is valid only when the kinetics of ice melting and water freezing is sufficiently quicker than the hydrate kinetics. This assumption is made because we are unaware of a suitable kinetic model for the phase transition between the aqueous-phase and the ice, and we believe that the incorporation of a gas molecule into the water clathrates is slow compared to freezing.

CO_2-hydrate phase diagram

Figure 7.2.d.2(a) shows the pressure-temperature phase diagram of the CO_2-hydrates (Sloan, 1998). Two curves are shown in Figure 2(a). The points shown as triangles represent the equilibrium data of the CO_2 gas-hydrate system, while the points plotted as squares show the equilibrium data for pure CO_2 gas-liquid system. Above the CO_2 gas-liquid equilibrium curve, at high pressures, CO_2 exists as a liquid-phase while below the curve CO_2 exists as a gas. Similarly, CO_2 in the presence of water exists as a hydrate above the CO_2 gas-hydrate equilibrium curve, and as a liquid or gas below the CO_2 gas-hydrate equilibrium curve, depending on the temperature and pressure conditions.

Figure 7.2.d.2(a) also shows the two quadruple points for the CO_2 equilibrium diagram. The vertical line on the left passes through the left quadruple point, the freezing point of water (271.1 K, T_{qdl}). The freezing point is less because the CO_2 solubility in the water is high. Ice exists on the left side of the vertical line and water on the right side. The vertical line on the right shows the intersection of the gas-liquid equilibrium curve for pure CO_2 with the hydrate-CO_2 equilibrium curve (283.2 K, T_{qdr}). At the left quadruple point we can have aqueous, gas, hydrate and ice phases. On the right quadruple point we can have gas-CO_2, liquid-CO_2, water and hydrate. For this data we have developed a correlation (Eq. 2) to represent the equilibrium curves, similar to the correlation for methane-hydrates developed by Moridis (2003).

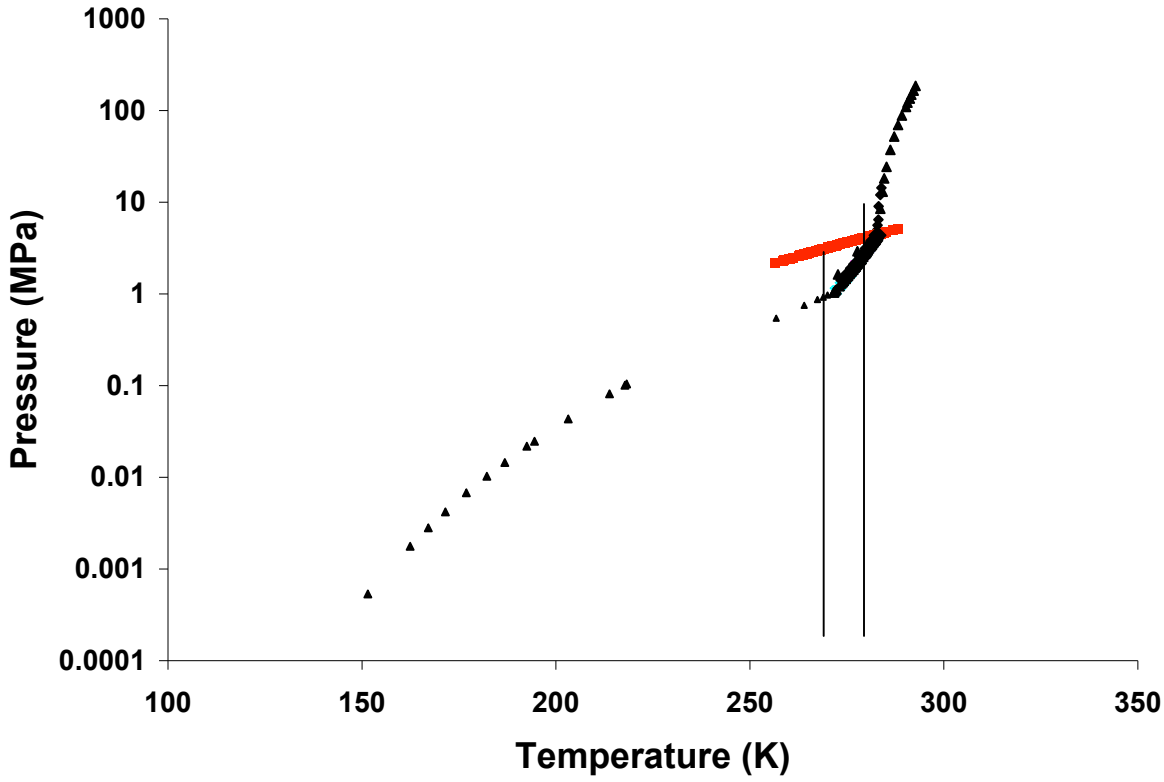

Figure 7.2.d.2(a): Equilibrium data for CO2- hydrate system

$$P_{ec} = \begin{cases} \exp(2.95910923520255\times10^{-10}\mathrm{T}^5 - 3.11697200658458\times10^{-7}\mathrm{T}^4 \\ \quad + 0.000132144540610005\mathrm{T}^3 - 0.0284975863532\mathrm{T}^2 \\ \quad + 3.21260589574589\mathrm{T} - 145.260413199229) \\ \qquad\qquad T \le T_{qdl} \\ \exp(-3.90289929172812\times10^{-6}\mathrm{T}^5 \\ \quad + 0.0054246841668\mathrm{T}^4 - 3.01568474817701\mathrm{T}^3 \\ \quad + 838.17111136993\mathrm{T}^2 - 116470.278754549\mathrm{T} \\ \quad + 6473275.96654239) \\ \qquad\qquad T_{qdl} < T \le T_{qdr} \\ \exp(0.000112579309352343\mathrm{T}^5 - 0.16247250385449\mathrm{T}^4 \\ \quad + 93.7907178622661\mathrm{T}^3 - 27071.2822913195\mathrm{T}^2 \\ \quad + 3906853.0872557\mathrm{T} - 225530302.91665) \\ \qquad\qquad T > T_{qdr} \end{cases} \qquad (2)$$

To find the fraction of the liquid CO_2 phase and the gas CO_2 phase at a particular pressure and temperature, the flash calculation is done for the two components, methane and carbon-dioxide, and the two phases, liquid phase (CO_2-rich phase) and gas phase (methane-rich phase) using the Peng-Robinson equation of state. The formation and dissociation of the CO_2-hydrate is treated as a kinetic phenomenon similar to the formation and dissociation of the methane-hydrate.

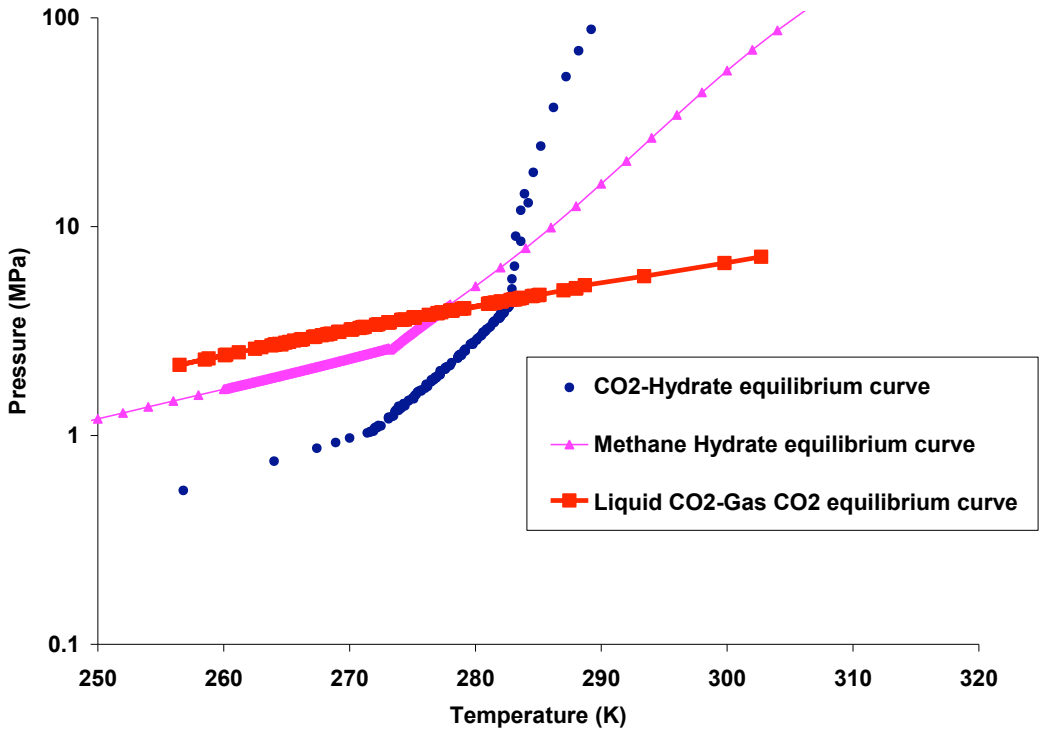

Figure 7.2.d.2(b): The equilibrium data for methane and CO_2 hydrates

Figure 7.2.d.2(b) shows the pressure-temperature phase diagram of methane-hydrate and CO_2-hydrate together. The circles show the CO_2-hydrate equilibrium curve, the triangles show the methane-hydrate equilibrium curve, and the squares show the CO_2 gas-liquid equilibrium curve. In the area between the circles and the triangles, methane exists as a gas while CO_2 exists as a hydrate.

Kinetic model

The kinetics of hydrate formation and dissociation, written as the consumption rate of gas, is described by Eq. 3

$$r^m = kA_s(f - f_{eq}), \qquad (3)$$

where r^m (mol/m^3-s) is the consumption rate of methane or carbon-dioxide; k (mol/m^2-Pa-s) is the kinetic constant of hydrate formation or dissociation; A_s (m^2/m^3) is the reaction surface area. f is the fugacity of the gas at given pressure and temperature condition and f_{eq} is the equilibrium fugacity of the gas at the given temperature. The consumption rate of water and hydrate can be calculated as:

$$r^w = nr^m, \qquad r^h = -r^m \qquad (4)$$

where r^w and r^h are the consumption rates of water and hydrate, respectively; n is the hydration number of the hydrate. The Peng–Robinson equation of state is used to evaluate the gas fugacity f and f_{eq} in Eq. 3. The direction of the transition between the gas, water and hydrates is determined by the driving force ($f - f_{eq}$). Hydrates tend to form when ($f - f_{eq}$) is positive, i.e., the gas pressure at a particular temperature is greater than the equilibrium pressure at that temperature ($r^m > 0$). On the other hand, if $p_G < p_e$ (where p_G is the actual gas pressure and p_e is the equilibrium pressure), the driving force $f - f_{eq}$ is negative, and hydrates tend to dissociate ($r^m < 0$). If $p_G = p_e$, then ($f - f_{eq}$)=0, which implies reaching an equilibrium state ($r^m = 0$).

For hydrate dissociation, the kinetic constant k is written in an Arrhenius-type equation as (Kim et al., 1987)

$$k = k_0 \exp\left(-\frac{Ea}{RT}\right) \tag{5}$$

where k_0 is the intrinsic kinetic constant, Ea is the activation energy, and R is the gas constant (8.314 J/molK). For methane-hydrate in a bulk phase system without salt, k_0 = 3.6×10^4 mol/m^2 Pa s, and Ea/R =9752.73K, as measured by Clarke and Bishnoi (2001). For CO_2-hydrate without salt k_0 = 1.83x10^5 mol/m^2 Pa s, and Ea/R = 12374.308 K, as measured by Clarke and Bishnoi (2004). Measurement of the kinetic constant for the hydrate formation is more difficult than for the dissociation. Englezos et al. (1987a) measured the value for the formation of methane-hydrate from methane gas and water. The results exhibited an ambiguous dependence on temperature. In this work, the kinetic constant of the hydrate formation is assumed to be a constant and its default value takes the average of the results measured by Englezos et al. (1987a), which is 0.5875×10^{-11} mol/m^2-Pa-s. For the CO_2-hydrate formation, the rate constant is taken from Malegaonkar et al. (1997) and is approximated as 0.35x10^{-10} mol/m^2-Pa-s.

The determination of the reaction surface area A_s in Eq. 3 for a porous medium system is still quite uncertain, because it is difficult to visually monitor the hydrates inside the pores. Many methods have been used to calculate the area. Yousif et al. (1991) estimate the area using the relation:

$$A_s = \sqrt{\frac{\phi_e^3}{2K}} \tag{6}$$

where K is the permeability of the porous medium and ϕ_e is the effective porosity. The volume inside pores available to fluids keeps changing due to the formation and dissociation of the hydrates in the hydrate bearing porous medium. The absolute porosity (ϕ) is constant during the process and the effective porosity is calculated as:

$$\phi_e = \phi(S_{FL}+S_{AQ}) \tag{7}$$

where S_{FL} is the saturation of the fluid phase (CO_2 + CH_4 rich phase) and S_{AQ} is the saturation of the aqueous phase (water rich phase). Masuda et al. (2002) used the following equation to estimate A_s:

$$A_s = \phi S_H A_{Si} , \quad (8)$$

where A_{Si} is a constant $3.75\times10^5 m^2/m^3$. In the present study the method used by Sun and Mohanty (2005) is used. They have proposed

$$A_s = \Gamma A_p \quad (9)$$

where A_p is the pore surface area and Γ is the fraction of the pore surface area that is active in the hydrate kinetics. The value of Γ depends on the actual process and is described in detail by Sun and Mohanty (2005). In the kinetics of the hydrate formation the nucleation process is neglected in Eq. 3 and it is assumed that the porous medium provides the nucleation sites for the hydrate formation.

Phase composition

The system can have six phases (gas, aqueous phase, CO_2-rich liquid phase, ice, methane-hydrate, CO_2-hydrate) and five components (methane, carbon dioxide, water, methane-hydrate, CO_2-hydrate). For the phase compositions, the following assumptions are made: (1) The adsorption of any component on the rock surface is neglected. (2) Hydrate phases have the respective hydrate component only, i.e., the methane-hydrate phase has only the methane-hydrate as a component and the CO_2-hydrate phase has only the CO_2-hydrate component. (3) the ice phase is composed of only the water component. (4) Gas is composed of methane, CO_2 and water. (5) The aqueous phase is composed of water, methane and CO_2. (6) the liquid phase has CO_2, methane and water (limited amount). The following symbols are used to represent the different phases and components. The phase symbols are used in the subscript for the properties and the component symbols are used in the superscript

Phases:

Methane-Hydrate: HM

CO_2-Hydrate: HC

Ice: IC

Aqueous: AQ

Fluid: FL (gas and liquid phase together which separately are represented as)

Gas: GS

Liquid: LQ

Components

Water: w

Methane: m

CO_2: c

Methane-Hydrate: hm

CO_2-Hydrate: cm

Based on the above assumptions, mass of each component can be found in a unit volume represented as

$$\begin{aligned} M^w &= \rho_{AQ} S_{AQ} X^w_{AQ} + \rho_{IC} S_{IC} + \rho_{GS} S_{GS} X^w_{GS} + \rho_{LQ} S_{LQ} X^w_{LQ} \\ M^m &= \rho_{AQ} S_{AQ} X^m_{AQ} + \rho_{GS} S_{GS} X^m_{GS} + \rho_{LQ} S_{LQ} X^m_{LQ} \\ M^c &= \rho_{AQ} S_{AQ} X^c_{AQ} + \rho_{GS} S_{GS} X^c_{GS} + \rho_{LQ} S_{LQ} X^c_{LQ} \\ M^{hm} &= \rho_{HM} S_{HM} \\ M^{hc} &= \rho_{HC} S_{HC} \end{aligned} \qquad (10)$$

where S_i is the saturation of the phase *i*, X_i^j is the mass fraction of the component j in the phase *i* and ρ_i is the density of the phase *i*.

For the phase saturations, the following equation must hold:

$$\sum_{i=AQ,GS,LQ,IC,HM,HC} S_i = 1 \qquad (11)$$

For the compositions of the gas, liquid, and aqueous phases,

$$\begin{aligned} X^w_{GS} + X^c_{GS} + X^m_{GS} &= 1 \\ X^w_{LQ} + X^c_{LQ} + X^m_{LQ} &= 1 \\ X^w_{AQ} + X^c_{AQ} + X^m_{AQ} &= 1 \end{aligned} \qquad (12)$$

To find the fractions of liquid and gas for a given fluid-phase saturation, where the fraction of the methane and carbon-dioxide is known, a flash calculation is done. The flash calculation also gives the fraction of the CO_2 and the methane components in both the phases. To find the equilibrium partition of the water in the fluid phase and the CO_2 and methane gases in the aqueous phase, solubility functions and Henry's law are used. The details of these functions are discussed by Sun and Mohanty (2005).

The densities of the solid phases, ρ_{HM} , ρ_{HC} and ρ_{IC} are assumed to be constant. In the present work, the values of ρ_{HM} , ρ_{HC} and ρ_{IC} are are set to be 0.9, 0.91 and 0.917 g/ml, respectively (Sloan, 1998). The gas- and liquid-phase densities, ρ_{GS} and ρ_{LQ} respectively, are evaluated with the Peng–Robinson EOS, and the aqueous-phase density ρ_{AQ} is considered a function of pressure, temperature and salinity according to the data given in the CRC Handbook of Chemistry and Physics (2004/2005).

Internal energy

The total internal energy per unit volume *U* is given by

$$U = \phi(\rho_{GS}S_{GS}U_{GS} + \rho_{AQ}S_{AQ}U_{AQ} + \rho_{HM}S_{HM}U_{HM} + \rho_{IC}S_{IC}U_{IC} + \rho_{HC}S_{HC}U_{HC} + \rho_{LQ}S_{LQ}U_{LQ}) + (1-\phi)\rho_S U_S, \quad (13)$$

where *Uj* is the specific internal energy of the phase *j* in J/kg and ϕ is the porosity of the porous medium. Note, the subscript *S* in the above equation represents the sediment phase, which is inactive in the mass transfer but plays an important role in the heat transfer. The sediment density ρ_S is assigned according to the rock mineralogy. The evaluations of U_{AQ}, U_{HM}, U_{HC}, U_{IC} and U_S have been described in detail by Sun and Mohanty (2005). U_{LQ} and U_{GS} are calculated by the Peng-Robinson EOS and thermodynamic evaluations of the enthalpy.

Flow models

The solid phases (*HM*, *HC* and *IC*) are assumed to be immobile. The convection of the fluid phases (*GS, LQ* and *AQ*) during the hydrate formation - dissociation process is usually slow; hence Darcy's law for multiphase flow can be used to find the convection of different phases (Lake, 1989).

$$\bar{v}_j = -\frac{\overline{\overline{K}}k_{rj}}{\mu_j}.\left(\nabla p_j + \rho_j \bar{g}\right) \quad (14)$$

where v_j is the Darcy velocity of the phase *j (j =GS, AQ* and *LQ)*; *K* is the absolute permeability tensor; k_{rj} , μ_j and p_j are, respectively, the relative permeability, the viscosity and the pressure of phase *j*; *g* is the gravitational acceleration.

The absolute permeability is estimated by using Civan (2001) power law model which is described in Phirani and Mohanty (2009). To find relative permeabilities, a two-phase system is considered, i.e., aqueous-phase and fluid-phase. For the two-phase system, the Brooks-Corey correlations are used to find relative permeabilities. To find the relative permeability of the gas-phase, which is a fraction of the fluid phase, a factor of (S_{GS}/S_{FL}) is multiplied to the fluid phase relative permeability while for the liquid phase system a factor of (S_{LQ}/S_{FL}) is used. The Brooks-Corey correlations used in this work are described in detail by Sun and Mohanty (2005). No capillary pressure is assumed between the liquid and gas phases, while the capillary pressure is assumed to be non-zero between fluid and aqueous phases and found using the Brooks-Corey model.

Gas viscosity μ_{GS} in Eq. 14 is considered to be a function of the temperature T and the density ρ_{GS} with the empirical model by Selim and Sloan (1989). The viscosity of the aqueous-phase μ_{AQ} is assumed to be a constant at 1 cp. The liquid viscosity μ_{LQ} is calculated using a correlation by Fong et al. (1996). The mass transfer is presumed to occur through only convection. Physical dispersion and diffusion are assumed to be equal to the numerical dispersion. The mass flux for the component *i (i = m,w, c),* F^i, is

$$F^i = \rho_{GS} v_{GS} X^i_{GS} + \rho_{AQ} v_{AQ} X^i_{AQ} + \rho_{LQ} v_{LQ} X^i_{LQ} \, . \qquad (15)$$

The heat transfer can take place by both convection and conduction. The heat flux is calculated by

$$F^i = \rho_{GS} v_{GS} H_{GS} + \rho_{AQ} v_{AQ} H_{AQ} + \rho_{LQ} v_{LQ} H_{LQ} - \lambda \nabla T \, , \qquad (16)$$

where H_j *(J/*kg*)* is the specific enthalpy of the phase *j (j =GS,AQ and LQ)* and λ (W/m K) is the effective thermal conductivity. The evaluation of H_{GS}, H_{LQ} and H_{AQ} are described in Sun and Mohanty (2005). Energy is treated as a pseudo-component in the present work and is represented by the superscript "*e*". λ is the volume average of the conductivity of the phases present in the unit volume.

Governing equations and numerical solution

Mass Balance equations are:

$$\frac{\partial}{\partial t}\left(\varphi M^m\right) + \nabla \cdot \overline{F}^m = -MW^m r^m + q^m \qquad (17a)$$

$$\frac{\partial}{\partial t}\left(\varphi M^c\right) + \nabla \cdot \overline{F}^c = -MW^c r^c + q^c \qquad (17b)$$

$$\frac{\partial}{\partial t}\left(\varphi M^w\right) + \nabla \cdot \overline{F}^w = -MW^w r^w + q^w \qquad (17c)$$

$$\frac{\partial}{\partial t}\left(\varphi M^{hm}\right) = -MW^{hm} r^{hm} \qquad (17d)$$

$$\frac{\partial}{\partial t}\left(\varphi M^{hc}\right) = -MW^{hc} r^{hc} \qquad (17e)$$

The energy balance equation is:

$$\frac{\partial}{\partial t}\left(\varphi U\right) + \nabla \cdot \overline{F}^e = -q^e \qquad (18)$$

The simulator solves the above equations along with the thermodynamic properties of CO_2 and methane, the phase diagrams of the CO_2-hydrate and the methane-hydrate, the phase compositions, internal energy, kinetics of the hydrate formation and dissociation, and the flow and transport models described in the 'flow models' section. In the above equation MW^i is the molecular weight of the component i. The heat of formation and dissociation of the hydrate is incorporated in the energy balance equation through the internal energy calculations. Any in-situ sources of the components and energy are neglected, and hence the source term is determined by the boundary conditions applied. For the mass transfer equations, pressure or flow rate are used as the boundary conditions in the simulator, while for the energy balance equation, temperature is specified as the boundary condition.

A finite volume method is used to discretize the governing equations spatially. This discretization method provides the flexibility to use any co-ordinate system of our choice. The governing equations are discretized using backward Euler method in time, giving a fully implicit solution scheme. The phase mobility is calculated by single upstream averaging. In the discretized system every grid-block is governed by the six non-linear equations corresponding to the mass and energy balance equations. For each grid block, these equations are coupled with the thermodynamic, kinetic, flow and transport models. Mass transfer and heat transfer couple the equations for different grid-blocks.

Primary variable switch method is used to define the primary variables depending on the phase conditions in a particular grid-block. Three cases are considered in the present case, depending on the temperature and saturation conditions. This method is similar to the method used by Sun and Mohanty (2005). In the present work the three cases considered are described in Table 1.

Table 1: Cases considered in the primary variable switch method

Case	**Water-rich phase**	**Variables**
1	AQ	P, S_{AQ}, S_{HM}, S_{FL}, X^C_{FL}, T (S_{IC}=0)
2	AQ-IC	P, S_{AQ}, S_{HM}, S_{FL}, X^C_{FL}, S_{IC} ($T=T_{qd}$)
3	IC	P, S_{IC}, S_{HM}, S_{FL}, X^C_{FL}, T (S_{AQ}=0)

S_{FL} is the saturation of the fluid phase and X^C_{FL} is the fraction of CO_2 in the fluid phase. The flash calculation at a particular temperature and pressure condition gives the S_{GS} and S_{LQ} which are secondary variables. The primary variables are found by solving the governing equations. The secondary variables are calculated using the equations described above or from the thermodynamic calculations. The phase status or the case is determined by S_{AQ} and S_{IC}. If S_{AQ} >0 and S_{IC}>0, then we are in case 2 and the corresponding primary variables are used. If only S_{AQ}>0, then we are in case 1, and the

corresponding primary variables are chosen. If only $S_{IC}>0$, then we are in case 3, and the corresponding primary variables are chosen. If $S_{AQ}=0$ and $S_{IC}=0$, then the temperature of the grid block is checked to determine the phase status. If $T>T_{qd}$, then case 1 is used, if $T<T_{qd}$ then case 3 is used and if T=Tqd then case 2 is used. The primary variables are switched according to the change in the phase status of the grid block, which is the status of the water-rich phase. If a grid block has ice and water present, then the temperature has to be the quadruple point temperature where ice and water can co-exist. Thus, temperature is not a primary variable, which is case 2 in Table 1. If during the simulation the ice-phase disappears, then we are no longer on the quadruple point. The aqueous phase saturation and temperature are the primary variables, while the ice saturation is known and equals 0. If the aqueous-phase disappears, then we move from case 2 to case 3 in Table 1.

The Newton Raphson method is used to solve the discretized equations after ascertaining the variables similar to the method used by Sun and Mohanty (2005). The PVSM method is used inside the Newton-Raphson method where the phase status is checked for each Newton-Raphson iteration.

Results and discussion

Using the model developed above, core scale CO_2 flooding of methane-hydrate bearing sediments is simulated. A 12 cm core saturated with water and methane-hydrates is considered. The initial saturation of water is 0.6 and the initial saturation of methane-hydrate is 0.4. The initial pressure in the core is assumed to be 6.1MPa at a temperature of 278K. At this pressure and temperature conditions, methane exists in the hydrate form. Figure 7.2.d.3 shows the schematic of the core used for the simulations. To dissociate the methane-hydrates, pure CO_2 is injected from the left boundary at 6.11MPa and 278K. At this pressure and temperature conditions, CO_2 exists in the liquid form. The pressure at the right boundary is maintained at 6.09MPa. The pressure drop across the core is 0.02MPa. 1-D simulations are performed for CO_2 injection in the above described methane-hydrate bearing core. The simulation was carried out for 50hrs of CO_2 injection. The domain is discretized in 10 gridblocks.

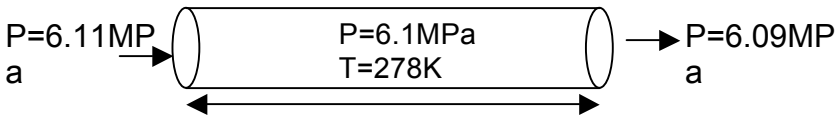

Figure 7.2.d.3: Schematic of the core used for simulations.

As the CO_2 liquid phase goes in the core, the saturation of the fluid phase increases with a high mole fraction of CO_2 and the partial pressure of methane decreses in the fluid phase. This implies that equilibrium fugacity of methane (fugacity at the current temperature and equilibrium pressure of the hydrate formation) is greater than the actual fugacity of methane gas. To equilibrate the two fugacities, methane-hydrate dissociates and the mole fraction of methane in the fluid phase increases. The injection of pure CO_2 pushes the dissociated methane downstream. 15% of the total methane-hydrate present in the system dissociates within 50 hrs of CO_2 injection. Figure 7.2.d.4 shows the cumulative production and injection from the core in terms of pore volumes. If all the pores are filled with hydrate then the total amount of gas (CO_2 or methane) present is about 160 pore volumes. Methane-hydrate saturation is 0.4, hence about 40 pore volumes of methane are present. Figure 7.2.c.4 shows that we are able to produce 0.8 pore volumes of methane and 2.6 pore volumes of CO_2 while we inject about 15 pore volumes of CO_2 in the core in 50 hrs. A small amount of water is also pushed through the production boundary. In situ profiles of saturations and temperature provide some insight into this process.

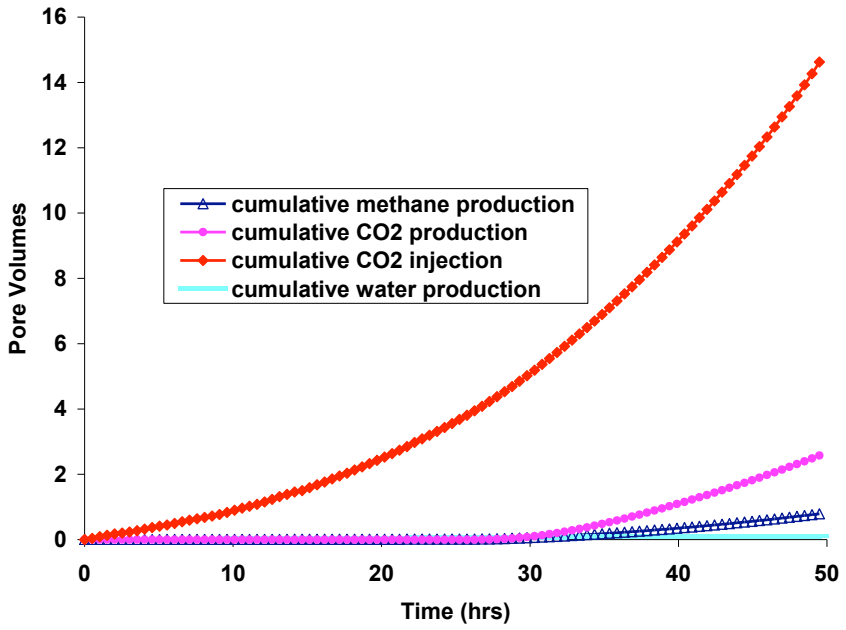

Figure 7.2.d.4: Cumulative methane production, CO_2 production and CO_2 injection

Conclusions

A thermal, compositional, kinetic simulator for CO_2 flooding of the methane-hydrate bearing sediments is developed. 1-D simuations of CO_2 injection shows that the fluid saturation remains low due to the adverse mobiity ratio of the displacement of water

with gas/liquid CO_2. To form CO_2-hydrate a specific fraction of CO_2 should be present in the fluid phase which is continuously decreased by the release of methane (due to the methane-hydrate dissociation). The energy of formation of the CO_2-hydrate is utilized in the methane-hydrate dissociation which maintains the temperature of the core. The methane-hydrate dissociation front moves at a slow rate of approximately 1/40 cm/hr for the kinetics assumed in the base case. To dissociate methane-hydrate by CO_2 injection, either we need to keep the CO_2 mole fraction very high in the fluid phase or operate at a relatively lower pressure (shallower reservoirs of methane-hydrates).

Task 8: Seafloor and Borehole Stability

Summary

To assess the seafloor and borehole stability, we completed three integrated subtasks that allowed us to use numerical models, laboratory data and experiments, logging and geophysical data, and field data. The three subtasks completed were: Subtask 8.1 – Sediment hydrate properties; Subtask 8.2 – Modeling (In)Stability; and Subtask 8.3 – Data Integration and Collaboration. The primary scientific accomplishments were the development of models on heterogeneous hydrate accumulation including fracture hosted hydrate in clays, the time-frames and mechanics of fracture genesis, and the preference for systems to allow fracture-dominated failure and hydrate accumulation over large-scale slope instability. This first order insight may help explain why hydrate-related slope failures are hard to find in nature – the fracturing process may release pressure prior to large-scale failure. Future research will continue to look at scenarios that generate large failure and/or systems that are primed for failure due to hydrates. These model studies (Subtask 8.2) were largely fed through the collaboration and data gathering that occurred through Subtasks 8.1 and 8.2. We have published peer-reviewed papers and given national and international presentations on each Subtask (see Publications and Presentations).

Milestone status

8.1a Collection of data – completed 05/08

8.1c Complete database – completed 06/10 and resulted in a review paper of physical properties of gas hydrate bearing sediment has been published (Waite et al., 2009) and a digital database has been submitted to NETL.

8.2a Link database with models – completed 12/11. We have developed numerous 1D, 2D, single-phase, multi-phase, steady-state and transient models for fluid flow and geomechanical processes in hydrate systems. Each of these models relies on geomechanical and fluid flow properties that we developed or collected from previous studies.

8.2b Add sediment stability to models – completed 12/11. We have 1D and 2D slope stability models that define how and when fractures and slope failures occur in hydrate setting.

8.2c Conditions for (in)stability – completed 12/11. We have shown how failures can occur in terms of local failure (fractures) at geologic and human timescales and how this explains many physical and geophysical field observations about fluid flow transients and hydrate-filled fractures in fine-grained sediments. This work also shows a preference for fracturing over large-scale, regional failure, which to a first order may explain the difficulty in truly locating hydrate-related slope failure in natural systems. High overpressure genesis will drive regional failure, which

we have shown, however this is not unique to hydrate systems but is a trait of many overpressured settings worldwide. Figure work on transients in hydrate systems could implicated hydrates as a trigger in driving force in very specific settings. We will continue to pursue this work in our ongoing, non-hydrate slope stability projects.

8.3 Integrating Geomechanical Studies – completed 09/09. This task was completed in parallel with subtask 8.1 and resulted in a physical properties workshop and a review paper on geomechanical properties. This paper has been used to provide input for models, to synthesize the state of knowledge of geomechanical properties, and to motivate studies where data are insufficient.

Subtask 8.2: Modeling (in)stability

Understanding the processes which control the accumulation and distribution of methane hydrates is integral to understanding their role in geohazards, global climate change, and energy production. We completed numerical modeling studies of porous and fractured media flow to examine the interaction between transient, heterogeneous flow paths and hydrate distribution in marine sediments (Figure 1). This theory-based research was tested against field observations of heterogeneous hydrate accumulations in fine-grained sediments from Ocean Drilling Program (ODP) Legs 164 (Blake Ridge) and 204 (Hydrate Ridge), Integrated Ocean Drilling Program (IODP) Expedition 311 (Cascadia margin), the Gulf of Mexico Gas Hydrate Joint Industry Project (GOMJIP), and the India National Gas Hydrate Project (NGHP). Our work extended regional, steady-state hydrate studies by examining the pore- and fracture-scale processes that influence the fluid and chemical transport controlling methane hydrate accumulations. In our models, we focused on how hydrate formation in fractures and pores affects the permeability and pressure distribution in the system, as well as the effects on chemical equilibria. The primary outcomes of this work are that formation of fracture-hosted hydrate deposits by hydraulic fracturing is possible in settings with high methane flux and low sediment permeability; that the relative fluxes of different methane phases (dissolved/gaseous) influences hydrate and fracture distributions; that pore-scale inhibition of hydrate nucleation due to capillary phenomena controls preferential accumulation of hydrate in coarser-grained sediments; and that marine hydrate provinces are dynamic settings that evolve on time scales from decades to centuries.

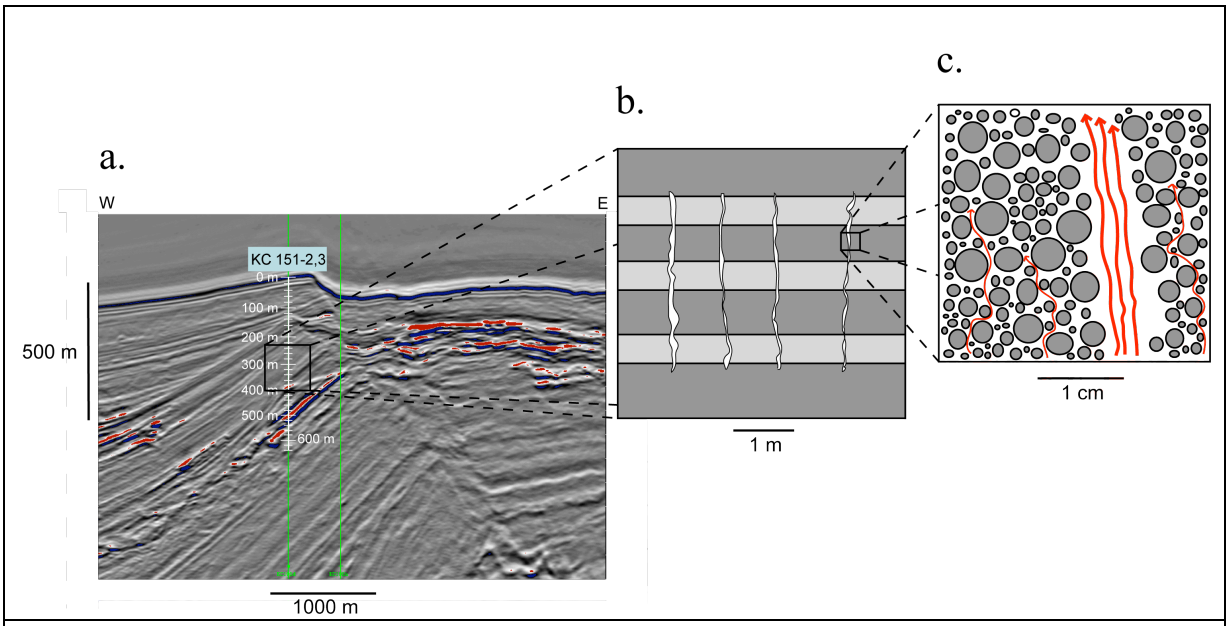

Figure 1. Illustration of different scales and heterogeneity of fluid flow paths and hydrate accumulation in gas hydrate systems. (a) Seismic line across the Keathley Canyon Block 151 well site showing a regional-scale methane hydrate zone. The bottom simulating reflection (BSR) crosses the wellbore at ~390 meters below sea floor. (b) Schematic of vertical fractures through fine-grained sediments, which can act as zones of focused fluid flow, which are forced apart due to increased fluid pressures. (c) Fluid flow occurring at the fracture and pore scale. If a fracture is sufficiently clogged with hydrate, the fracture permeability can be decreased to a value near that of the sediments, at which point flow through the porous medium becomes an important mode of fluid transport.

We estimate that thousands to millions of years are required to form fracture systems by hydraulic fracturing driven by occlusion of the pore system by hydrate. This time scale is a function of rates of fluid flow and permeability loss. Low-permeability layers in a sedimentary column can reduce this time if the permeability contrast with respect to the surrounding sediments is of order 10 or greater. Additionally we find that tensile fracturing produced by hydrate heave around hydrate lenses is a viable fracture mechanism over all but the lowermost part of the hydrate stability zone. With our coupled fluid flow-hydrate formation model, we assessed fracture formation at four well-studied hydrate provinces: Blake Ridge offshore South Carolina, Hydrate Ridge offshore Oregon, Keathley Canyon Block 151 offshore Louisiana, and the Krishna-Godavari Basin offshore India (Figure 2). We conclude that hydraulic fracturing due to pore pressure buildup is reasonable only at Hydrate Ridge and the Krishna-Godavari Basin due to sediment age constraints, and that hydrate-filled fractures observed at Blake Ridge and Keathley Canyon Block 151 are formed either by hydrate heave or in preexisting fractures. Our findings offer new insight into the processes and time scales associated with fracture-hosted hydrate deposits, which help further our understanding of hydrate systems.

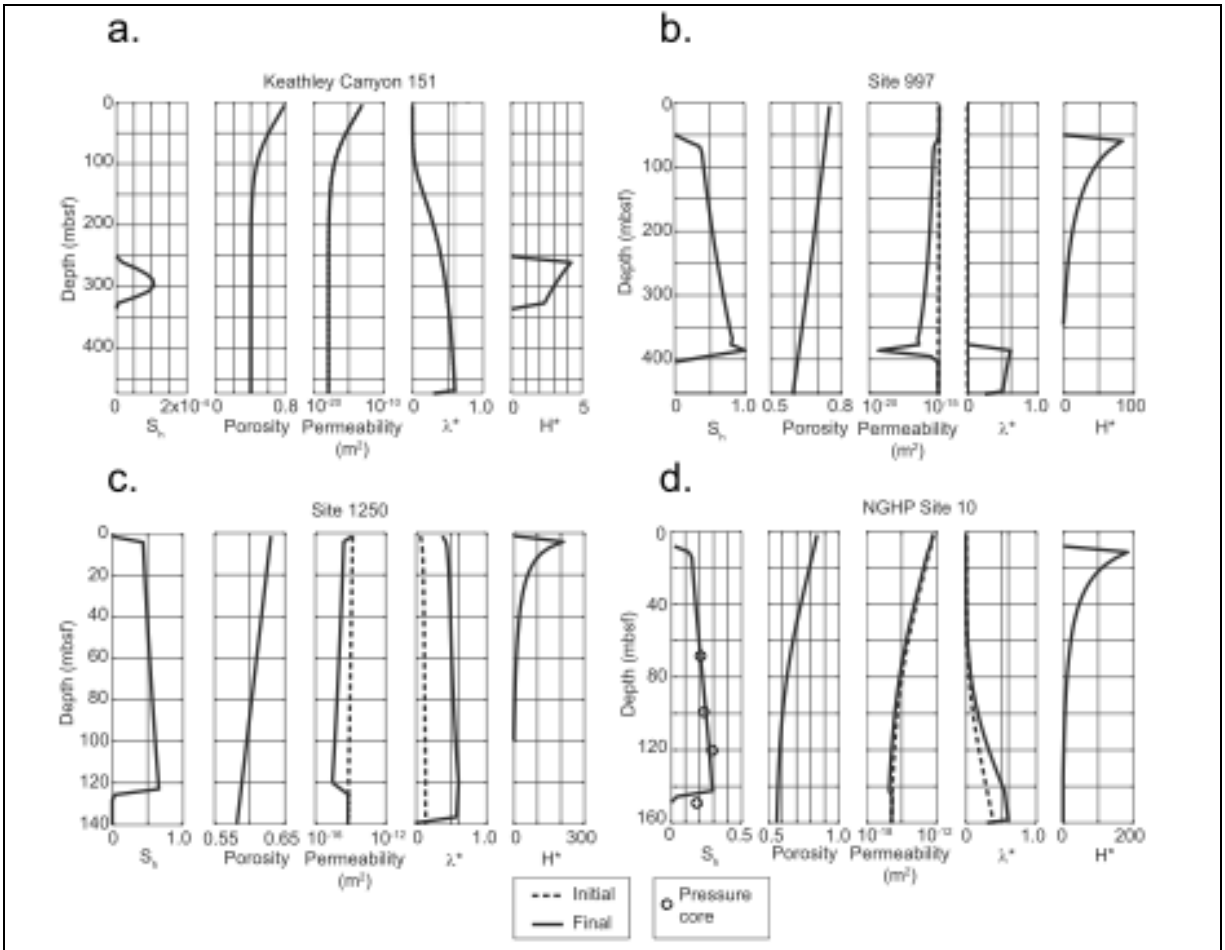

Figure 2. (a) Model results for KC151 with q_f = –0.4 mm/yr. From left to right: hydrate saturation, porosity, permeability, overpressure ratio λ*, and ratio of hydrate heave force to vertical effective stress H*. The fracture criterion is represented by the dashed line at λ* = 0.6. The hydraulic fracturing criterion is achieved after 900,000 years. Hydraulic fractures initiate at the base of the MHSZ. The hydrate heave force is sufficient to produce sub-vertical veins and fractures in the interval 250–340 mbsf. S_h is small in this case because the initial λ* is close to the critical value of 0.6, requiring only a slight reduction in permeability to cause fracturing. (b) Model results for Blake Ridge with q_f = –0.2 mm/yr. The fracture criterion is achieved after 8,000,000 years. Hydraulic fractures are generated first near 390 mbsf where S_h = 0.99. The hydrate heave force is sufficient to produce sub-vertical veins and fractures in the interval 50–310 mbsf. (c) Model results for Hydrate Ridge with q_f = –300 mm/yr. The fracture criterion is achieved after 9,000 years. Fractures initiate near 122 mbsf. The hydrate heave force is sufficient to produce sub-vertical veins and fractures above 90 mbsf. (d) Model results for NGHP Site 10 with q_f = –35 mm/yr. The hydraulic fracturing criterion is achieved after 100,000 years. The hydrate heave force is sufficient to produce sub-vertical veins and fractures in the interval 10–135 mbsf. Note how the computed S_h profile closely matches the pressure core saturations; we use this match as a constraint on vertical flow rates.

We simulated methane hydrate formation with multiphase flow and free gas within the regional hydrate stability zone (RHSZ). We found that hydrate distribution and fracture behavior are largely determined by the phase of the methane supply. In our model we allowed free gas to enter the RHSZ when porewater salinity increased to the value required for three-phase equilibrium. Fractures nucleate when the excess pore pressure exceeds the vertical hydrostatic effective stress. At Hydrate Ridge, where methane supply is dominantly free gas, hydrate saturation increases upwards and fractures nucleate high within the RHSZ, eventually allowing gas to vent to the seafloor (Figure 3). At Blake Ridge, where methane supply is dominantly in the dissolved phase, hydrate saturation is greatest at the base of the RHSZ (Figure 3); fractures nucleate here and in some cases could propagate through the RHSZ, allowing methane-charged water to vent to the seafloor (Figure 4). This demonstrates that the rate of methane supply to the RHSZ controls the rate of hydrate formation and time required to generate hydraulic fractures regardless of the phase of the methane, and that the phase of the supplied methane controls the location of fractures within the RHSZ.

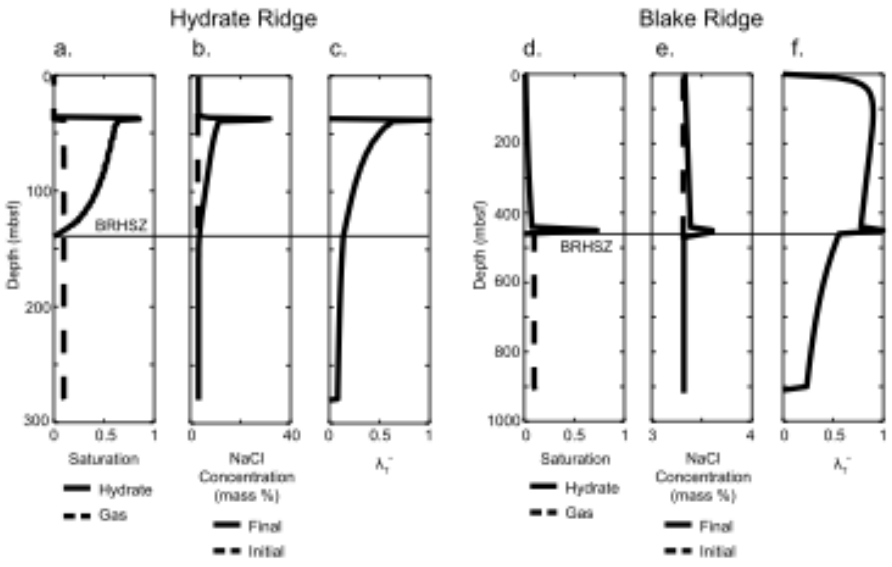

Figure 3. Model results. Entire model domain (twice RHSZ thickness) is plotted. (a) S_h and S_g at Hydrate Ridge after 1900 years. Gas has migrated ~100 m upwards through the RHSZ. S_h increases upwards since salinity must be higher shallower in the RHSZ to reach three-phase equilibrium. (b) Salinity at Hydrate Ridge. Salinity has increased to ~30% at 38 mbsf. (c) λ_T^* at Hydrate Ridge. Values increase upwards to 38 mbsf, where fractures initiate. (d) S_h and S_g at Blake Ridge after 16,000 years. Gas is unable to move into the RHSZ because excess salt is removed by water flux. Hydrate forms most rapidly at the BRHSZ where the dissolved methane concentration gradient is greatest. (e) Salinity at Blake Ridge. Salinity increases slightly near the BRHSZ due to methane formation. Most salt is flushed upwards in the water flux. (f) λ_T^* at Blake Ridge. Fractures initiate at the BRHSZ where the most hydrate has accumulated. $\lambda_T^* \approx 0.6$ just below the BRHSZ, indicating elevated gas pressure at this point.

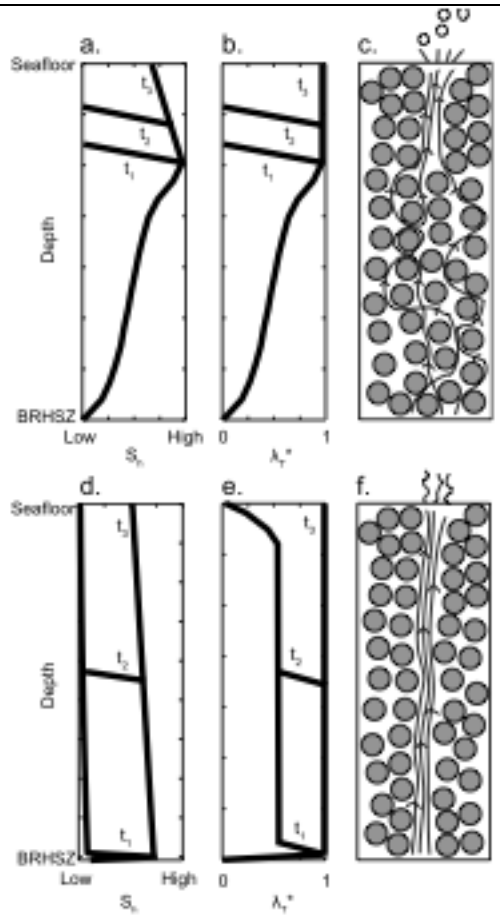

Figure 4. (a) In a gas-dominated system, fractures initiate at the top of the gas column at time t_1. Fracturing continues upwards as hydrate accumulates in existing fractures and increases P_c (t_2) until fractures reach the seafloor (t_3). Above the fracture nucleation point, S_h decreases since the effective stress decreases, requiring less hydrate to drive pore pressures to the point of failure. (b) Evolution of λ_T^*. λ_T^* reaches 1 at t_1, and fractures propagate upwards as λ_T^* reaches 1 shallower in the system (t_2) until fractures reach the seafloor (t_3). (c) Conceptual model of gas migration pathways in a gas-dominated system. Gas moves through the pore space up to the point where fractures initiate, and through fractures above that point. Free gas vents to the seafloor, potentially forming pockmarks and releasing gas bubbles. (d) In a water-dominated system, gas is unable to enter the RHSZ. Fractures initiate at the BRHSZ when hydrate and free gas accumulation drives λ_T^* sufficiently high (t_1). As hydrate ac- cumulates higher in the RHSZ, fractures can propagate upwards (t_2) until they reach the seafloor (t_3). (e) Evolution of λ_T^*. λ_T^* reaches 1 at the BRHSZ (t_1), and as hydrate forms shallower in the RHSZ, fractures propagate upwards (t_2) until they reach the seafloor (t_3). (f) Conceptual model of water migration pathways in a water-dominated system. When fractures reach the seafloor, water moves preferentially through the fractures and reaches the seafloor in focused zones of high flux, creating seeps and chemosynthetic communities at the seafloor. Lower flux occurs through the pore system.

We simulated 1-D, steady, advective flow through a layered porous medium to investigate how capillary controls on solubility including the Gibbs-Thomson effect in fine-grained sediments affect methane hydrate distribution in marine sediments. We computed the increase in pore fluid pressure that results from hydrate occluding the pore space and allowed fractures to form if the pore fluid pressure exceeded a fracture

criterion. We applied this model to Hydrate Ridge and northern Cascadia, two field sites where hydrates have been observed preferentially filling cm-scale, coarse-grained layers. We found that at Hydrate Ridge, hydrate forms in the coarse-grained layers reaching saturation of 90%, creating fractures through intervening fine-grained layers after 2000 years (Figure 5). At northern Cascadia, hydrate forms preferentially in the coarse-grained layers but $2x10^5$ years are required to develop the observed hydrate saturations (~20-60%), suggesting that hydrate formation rates may be enhanced by an additional source of methane such as in situ methanogenesis. We developed expressions to determine the combinations of sediment physical properties and methane supply rates that will result in hydrate-filled coarse-grained layers separated by hydrate-filled fine-grained layers, the conditions necessary to fracture the fine-grained layers, and the conditions that will lead to complete inhibition of hydrate formation as pore space is constricted. This work illustrates how sediment physical properties control hydrate distribution at the pore scale, and how hydrate distribution affects fracturing behavior in marine sediments.

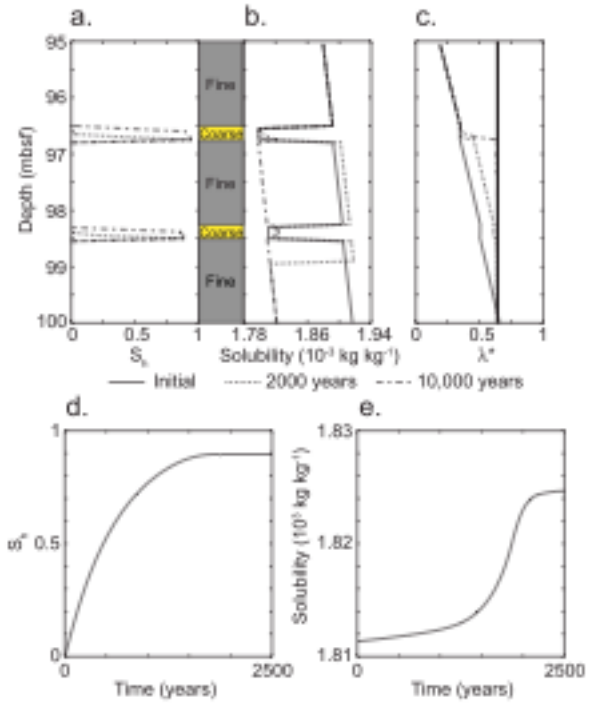

Figure 5. Model results for Hydrate Ridge. (a) Hydrate saturation. Both coarse-grained layers fill with hydrate to $S_h \approx 0.90$ after 2000 years. This is attributable to fractures opening in the fine-grained layers after 2000 years. (b) Methane solubility in the pore fluid. Initially the solubility in the fine-grained layers is greater than that in the coarse-grained layers. After 2000 years, hydrate has formed in the coarse-grained layers, and the solubility has increased slightly; the solubility in the fine-grained layers has increased slightly as well due to the increase in pore fluid pressure as hydrate occludes the pore space in the coarse-grained layers. Fractures have developed over the lowest 1 m of the lower fine-grained layer, and the solubility values reflect this as they have decreased to the value for free water. (c) Overpressure ratio. The critical value is marked by the solid line at $\lambda^* = 0.67$. (d) Hydrate saturation versus time in the lower coarse-grained layer. (e) Change in solubility versus time in the lower coarse-grained layer.

To investigate transient fracturing and methane venting behavior in dynamic systems, we applied our multiphase flow model to southern Hydrate Ridge. Episodic seafloor methane venting is associated with focused fluid flow through fracture systems at many sites worldwide. We investigated the relationship between hydraulic fracturing and transient gas pressures at southern Hydrate Ridge. Two collocated seismic surveys, acquired 8 years apart, at Hydrate Ridge show seismic amplitude variations interpreted as migration of free gas in a permeable conduit, Horizon A, feeding an active methane hydrate province. The geophysical surveys also reveal transients in gas venting to the water column. We propose that episodic gas migration and pressure fluctuations in the reservoir underlying the regional hydrate stability zone (RHSZ) at southern Hydrate Ridge influence methane supply to the RHSZ and are linked with periodic fracturing and seafloor methane venting (Figure 6). We modeled the effect of pore pressure variations within the deep methane source on fracturing behavior with a 1D model that couples multiphase flow, hydrate accumulation, and pore pressure buildup. As the reservoir pressure increases, fractures open when the pore pressure exceeds the hydrostatic vertical effective stress. Gas then flows through the fractures and vent at the seafloor while hydrate precipitates in the fracture system. We showed that active seafloor gas venting occurs for approximately 30 years, and that the available methane reservoir is exhausted 30 to 55 years after the onset of pressure buildup. This provides important constraints on the time scale of transient fluid flow at southern Hydrate Ridge, and illustrates how pore pressure pulses affect fluid flow and fracturing behavior in active methane hydrate provinces.

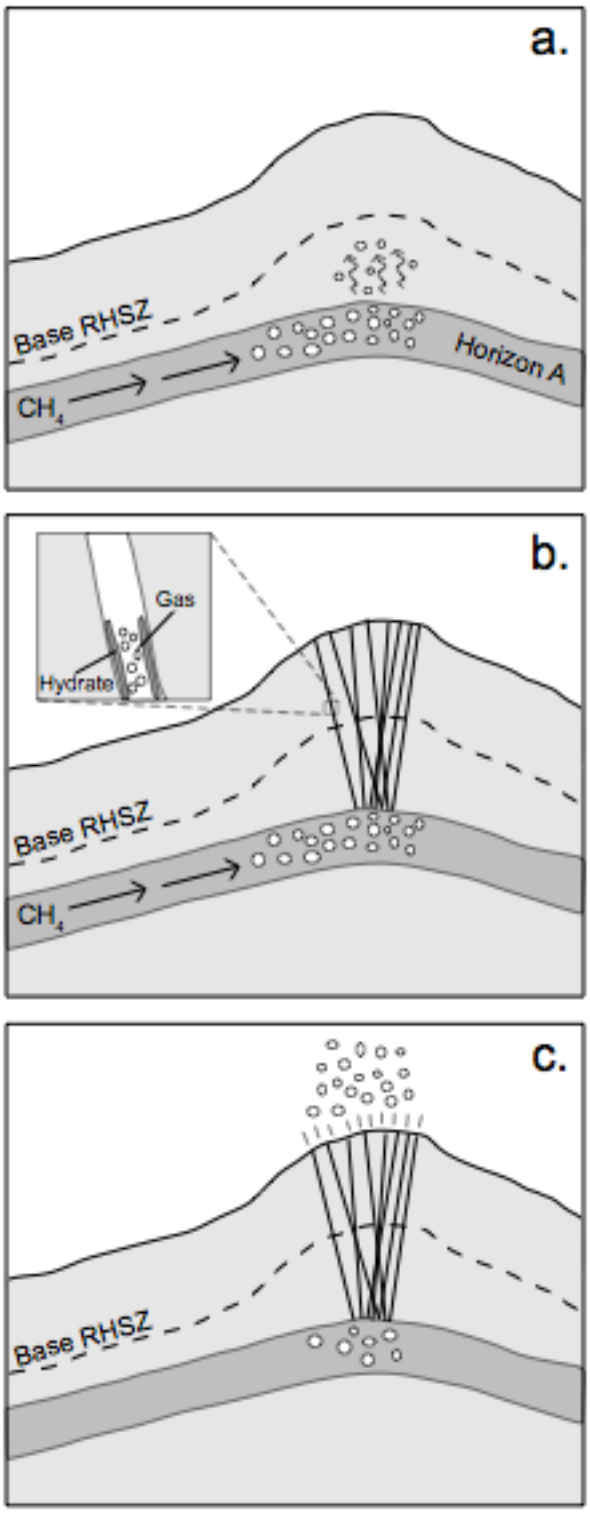

Figure 6. Model stages for hydrate accumulation, fracturing and venting. (a) Stage 1: accumulation of gas and porous medium flow above Horizon A. (b) Stage 2: fractures form, gas front propagates through fractures as hydrate forms and increases local salinity. (c) Stage 3: gas vents to the seafloor until gas reservoir is exhausted. Time-frames and venting history are highly controlled by the rate of pressure genesis in the deep horizon (Horizon A).

Beyond these models, we have also explored 2D models to look at stability and gas hydrate accumulations. These models include lithologic heterogeneity and multiple fluid phases. Heterogeneity has shown that permeable conduits increase the ability to capture methane thus increasing hydrate saturation (Figure 7). Simply, the larger the permeability contrast, the more likely hydrate and gas are to accumulate in the more permeable conduits. This may help explain saturations in high flux conduits like pipes, vents, and dipping reservoirs in advective systems. These systems along however do not generate large failure. The scenarios that yield large failure are those that have sedimentation-induced overpressure, which has been shown in multiple non-hydrate systems as well. These results, while first-order, indicate that hydrates along can generate local failures, but may not be able to self-generate failure; they may be a contributing factor, but not the sole driving force.

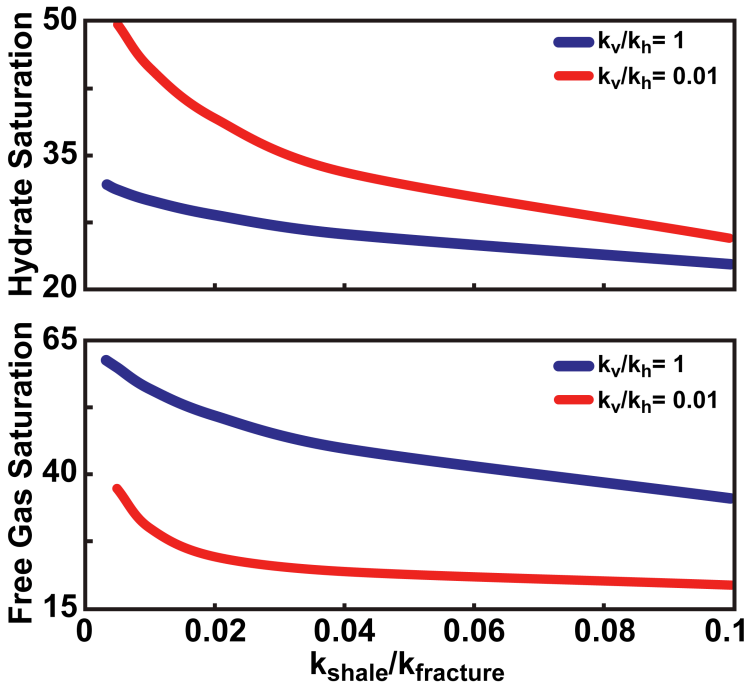

Figure 7. Model results showing the importance of permeability contrasts and permeability anisotropy on the accumulation and saturation of methane hydrate and free gas saturations. As permeability contrast between a shale and fracture (or sand) becomes smaller (k shale << k fracture or k sand) the hydrate and free gas saturations in the permeable unit increases. As anisotropy decreases (kv/kh) in the shale, the saturations also increase.

Subtask 8.3: Integrating geomechanical studies

This task has been coupled with Subtasks 8.1 and 8.2 as we use geomechanical field data to test our stability and fracture models. This subtask involved assessing our state of knowledge in geomechanics to maximize our understanding of geomechanical properties of hydrate bearing sediments across DOE-funded projects. We worked directly with the USGS, MIT, Georgia Tech, and LBNL produce a review manuscript on geomechanical properties.

Students

Hugh Daigle – PhD (2011) from Rice University for his hydrate-related research on geomechanics and fluid flow

L. Ashley Hubbard – MS (2008) from Rice University for investigation of fluid composition relationships at diverse sites in the northern Gulf of Mexico

Steinar Hustoft – visiting Ph.D. student from University of Tromso, Norway (2008) who studied sediment properties and fluid flow history for the hydrate bearing Norwegian margin

Nastasja Scholz – visiting PhD student from University of Victoria who studied fluid flow and slope stability in the hydrate region of the Cascadia margin

Hydrate Collaborations and Community Service

We have continued to collaborate formally and informally with national and international colleagues related to hydrate research. This has been in multiple formats including student exchanges, invited presentations at international meetings, participation in hydrate workshops, peer-review of hydrate proposals and papers, contributions to planning of field programs, and integration of our modeling work with existing field data. The extent of this work is detailed in our peer-reviews publications and presentations.

Task 9: Geophysical Imaging of Gas Hydrate and Free Gas Accumulations

Summary

We primarily focused on developing traveltime and waveform based method for detection of gas hydrate and a rock physics model for quantification of gas hydrate in fractured media.

Milestone status

Task	Date	Status
9.1 Preliminary processing and inversion of seismic data.	08/08 – 08/09	Completed. Manuscript in review
9.2: Final 1-D elastic and 2-D acoustic waveform inversion.	08/09 – 08/10	Completed. Manuscript in preparation
9.3: Rock physics modeling (in collaboration Stanford University)	08/10 – 08/11	Completed. Manuscript in preparation

1. The seismic data that is being used for Task 9 comes from Krishna-Godavari (K-G) Basin in the Indian east coast. The well data were collected during the NGHP drilling expedition in 2005. The PI is successfully collaborating with National Institute of Oceanography (NIO), India.

2. Prior to applying our imaging methodology we interpret existing seismic sections to obtain a generic idea about geo-thermal gradient, fault patterns, and BSR structure.

3. Subtask 9.1 involves preliminary processing and traveltime inversion of the data were accomplishes. A pre-stack depth migrated image is generated using velocity model from composite inversion/migration that agreed very well with the sonic log suggesting that the velocity model and the depth image were geologically accurate.

4. Subtask 9.2 involved 2-D acoustic and 1-D elastic waveform inversion. We realized that with the currently dataset was not suited for 1-D elastic inversion. Finally we performed 2D visco-elastic inversion

5. Subtask 9.3 involves development of rock physics model for quantification of gas hydrate in fractured media. This work is done is association with Jack Dvorkin of Stanford University.

Interpretation of existing seismic data

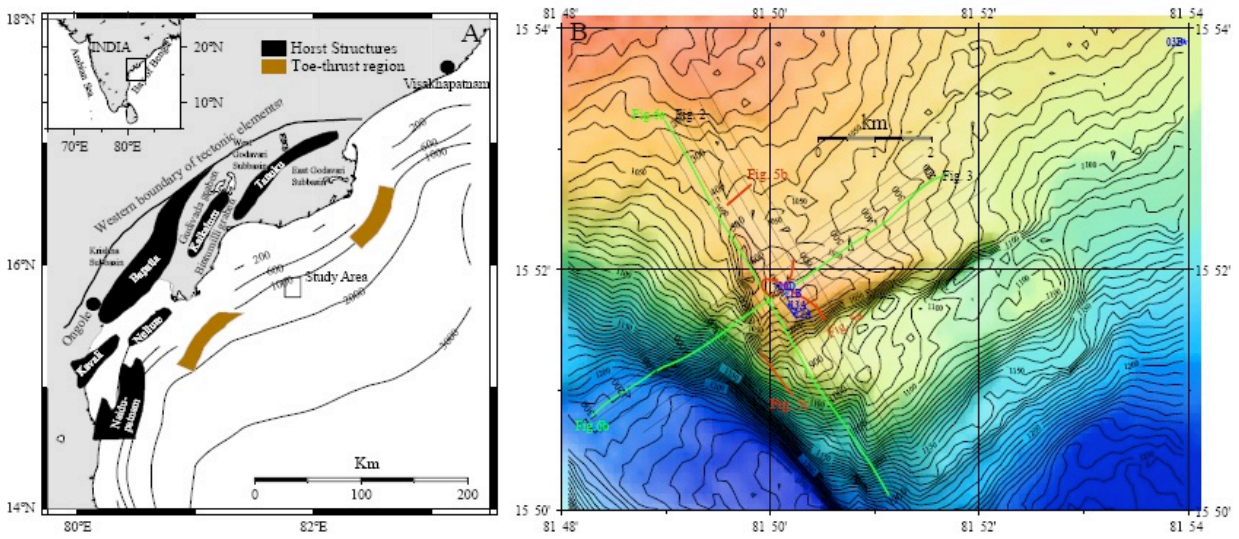

A B

Figure 1. Study Area. A. KG basin is located offshore east coast of India. The horst and graben structures and the toe-thrusts have been interpreted after Rao (2001) and Bastia (2006). Study area with multibeam bathymetry is shown in B. Seismic lines used in this study are indicated in solid back lines; seismic lines in green are displayed in Figures 2a (NW-SE) and 2b (SW-NE). The NW-SE line has been used for tomography as well as full waveform inversion. Stars denote location of NGHP-01-10/12/13/21 sites.

Hydrates have been inferred in the KG basin early on through exploration seismic datasets. The ground-truthing of hydrate deposits in the Indian continental margin occurred in 2006 through collaboration between the Indian National Gas Hydrate Program (NGHP) and the United States Geological Survey (USGS). An extensive drilling/coring operation known as the NGHP-01 expedition was executed to assess the hydrate potential of the Indian continental margin. During the expedition, which lasted over four months, 15 sites were visited in the KG basin (Collett et al., 2006). Three drill sites in the KG basin, NGHP-01-10, 12, and 13 (Figure 1), are relevant to this paper. Preliminary imaging of seismic data prior to the NGHP expedition suggested that the area around all the three sites is fault dominated and characterized by a patchy BSR (Collett et al. 2006).

During the NGHP-01 expedition Site NGHP-01-10 was both cored and logged, Site NGHP-01-12 only cored, and Site NGHP-01-13 only logged. The presence of gas hydrates was confirmed at Site NGHP-01-10 and 12 by visual observations. However, temperature anomalies from Infrared (IR) imaging were much higher in NHGP-10 compared to NGHP-01-12 suggesting greater hydrate saturation at NGHP-01-10. Hydrate concentration estimated from depressurization of pressure cores at NGHP-01-

10 and NGHP-01-12 is respectively estimated at 17.6 – 25.4 % and 2 % of the pore volume. Chlorine in the pore water at Site NGHP-01-10 has a deviation of 398 – 634 mM from its background value of ~556 mM indicating hydrate formation and dissociation. In contrast, no significant variation in Chlorine concentration is observed at NGHP-01-12 also suggesting that hydrates at Site NGHP-01-10 may not extend to Site NGHP-01-12. Site NGHP-01-13 was dilled 150m NW of NGHP-01-12 to test the continuity of hydrates at NGHP-01-10. The wireline resistivity at site NGHP-01-13 was found to be low compared to NGHP-01-10 (Figure 1). However, due to a fairly high resistivity over the background, in this paper we assume site NGHP-01-13 to have hydrates. In absence of a core at NGHP-01-13, the actual hydrate saturation at this site is not known.

In passive continental margins such as K-G basin the formation and distribution of gas hydrates appears to be closely related with the fluid/gas flow into the base of hydrate stability zone (BHSZ) from deeper region that can perturb the geo-thermal gradient (Ruppel and Kinoshita, 2000). In passive settings, anomalous flow occurs in areas with rapid sedimentation and compaction that prevents the fluids to be expelled during sedimentation (Judd and Hovland, 2007) and leading to perturbations in BHSZ (Pecher et al., 2009). It is also a common practice to use BSR derived heat flow to understand the thermal profile along the continental margins (Ganguly et al., 2000). In this study, we first interpret existing seismic data to estimate the geothermal gradient (GTG) to understand the thermal regime around NGHP-01-10 site. We identify zones of abnormal GTG and establish a relationship between abnormal GTG with the observed surface and subsurface structures.

Our current understanding is that large (> 10 m throw) scale faulting near the NGHP-01-10 site enables a focused fluid flow which in turn controls the growth and accumulation of the gas hydrate within the faults themselves. We suspect that the fluid flow also perturbs (increases by 15-20%) the regional geo-thermal gradient (38 ^{o}C/km) and final concentration of hydrates is from interplay between the volume of the advecting fluid, their temperature and methane concentration, and permeability of the faults. Using a suite of geophysical data we show that that high concentration of hydrates could be limited to parts of the stratigraphy that are close to the faults. It is possible that hydrate in the K-G basin in sites that have similar fault patterns as NGHP-01-10 are controlled by the faults and therefore have high spatial variability. Our findings have significant implication on the future of hydrate exploitation in the K-G basin.

Datasets used for fluid flow estimation comprise multi-channel seismic (MCS), high resolution sparker (HRS), Multi-beam bathymetry, and sub-bottom profiler (SBP). Fault pattern in the vicinity of the NGHP-10-01 is interpreted simultaneously on all datasets. Bottom-Simulating Reflector (BSR) in interpreted only in the MCS time and depth stacks. Increase in the interval velocity over a background velocity of 1.6 km/s is considered as a proxy for increase in hydrate concentration above the BSR. Similarly, decrease in interval velocity is considered as a proxy for free gas. Heat flow and GTG are calculated using the temperature at the seafloor and at the BSR from the NGHP-01-10 well core/logs.

Data

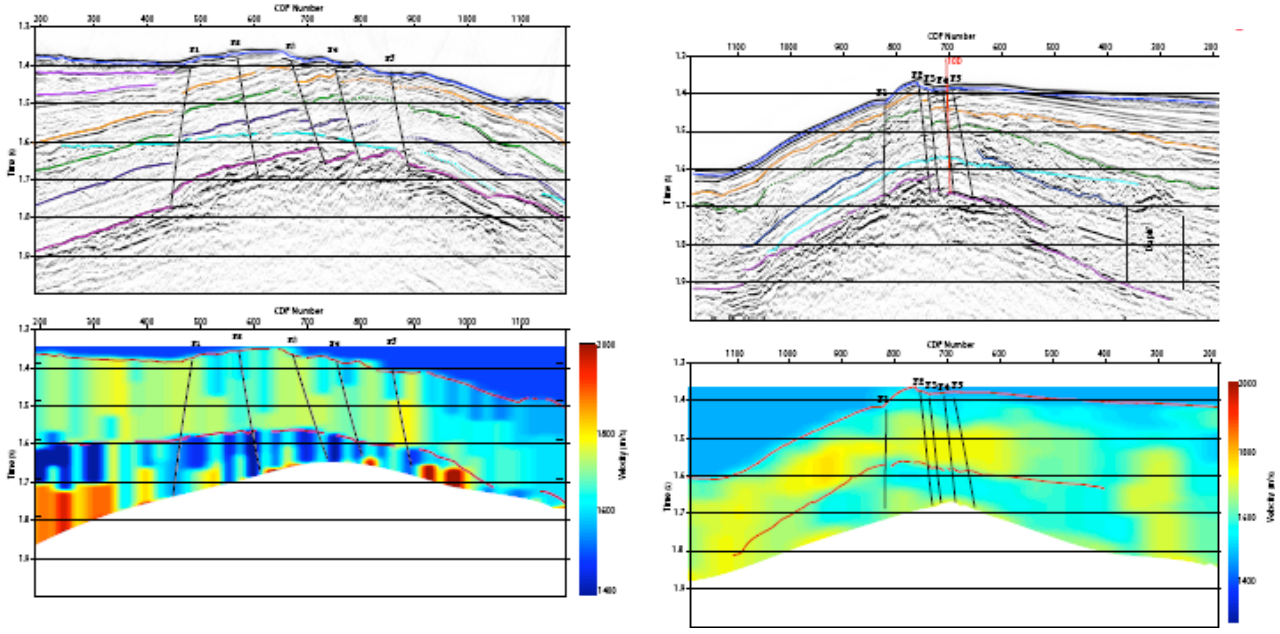

A. Line 15(NW-SE) B. Line 47 (NE-SW)

Figure 2. Multichannel Seismic. Top A and B: The interpreted section; light blue color represents BSR. Bottom A and B. The velocity model from the conventional semblance analysis method for stacking velocity estimation; blue is slower velocity and red is faster velocity. Water bottom and BSR are highlighted on the velocity model. A drop in interval velocity is observed below the BSR (free gas?) and several high velocity patches (hydrates?) are observed above the BSR.

About 100 km total length of MCS profiles (12 profiles ~8.5 km each covering the location of NGHP-10-01) were processed and interpreted. The main purpose of processing was to provide a quasi 3-D structural image. The processing sequence was simpler than the sequence adopted for inversion in Subtask 9.1. MCS processing follows standard methods emphasizing on deconvolution to remove the source bubble effects and normal and dip move-out velocity analysis. Other modules include trace editing, filtering, stacking, and post-stack time migration sequentially. Typically in marine datasets, multiples are a serious concern. Fortunately, in our case, due to the depth of the seafloor (~1000 m), seismic coda of interest lies within the first multiple (~2.67 s). The time sections were scaled in depth using stacking velocity. The seafloor and BSRs were picked on both time and depth seismic profiles after analyzing inline and crossline misties. The picked horizons were interpolated into three-dimensional surfaces.

Multi-beam bathymetry data was used sea floor topography. These data were acquired onboard Sagar Kanya in 2002. Processing of these data was done using Multibeam System 4.6.10 (Caress and Chayes, 1996) has been used to process and grid the swath bathymetry data. The bathymetric mosaic shows the surface expression of major faults.

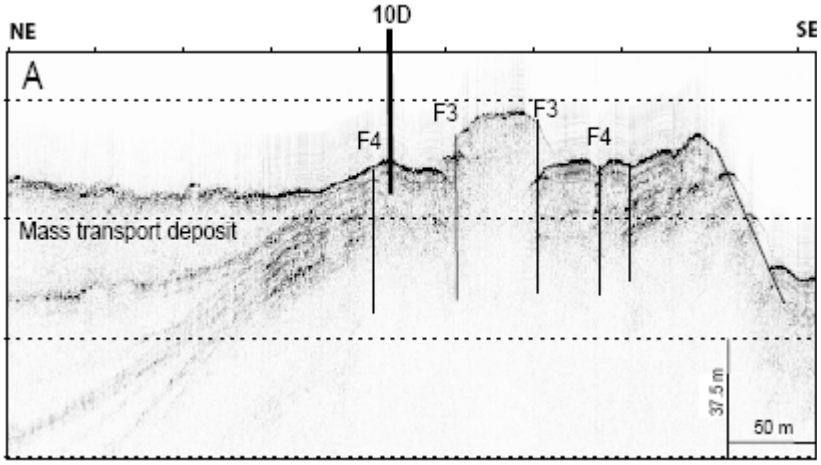

Figure 3. The SBP data close to the mound. The central portion of the mound is located close to site 10. The surface imprints of fault F3 and F4 have been interpreted. The SBP profile is coincident with Line 15 (Figure 2a).

The sea-bottom profile (SBP) data have been used to infer the shallow subsurface structure and faulting was acquired onboard Marion Dufresne in 2007 using Seafalcon 11 echo-sounder. One of the main features of this profiler was the use of a dedicated transmission array, large bandwidth signal and a large size multibeam reception array to create a high signal-to-noise ratio and a narrow beam width. SBP

High Resolution sparker (HRS) data was used to image shallow depths (< 100 m) below the seafloor in high resolution (~1.5 m scale). The data have a dominant frequency bandwidth of 150-1000 Hz and were acquired onboard Sagar Nidhi in 2009 using the 10KJ Geo-Resources Sparker system.

BSR derived geothermal gradient was computed from the depth and temperature of the seafloor and BSR. The seafloor temperature was obtained by using the available Conductivity-Temperature-Depth (CTD) profiles in the study area. The phase curve of methane hydrate and sea water was obtained from the equation of Miles et al (1995). The temperature at the BSR depth was obtained by considering the phase curve and the seafloor temperature assuming that the BSR depth corresponds to the base of the hydrate stability zone. GTG was calculated from the above parameters as:

$$GTG = \frac{(T_{bsr} - T_{sf})}{(Z_{bsr} - Z_{sf})}, \quad (1)$$

Where Z and T represent the depth and temperature respectively and the subscript *bsr* and *sf* corresponds to the BSR and seafloor respectively. The heat flow was calculated by multiplying GTG with the average thermal conductivity (0.82 W/mK) of the sediment as,

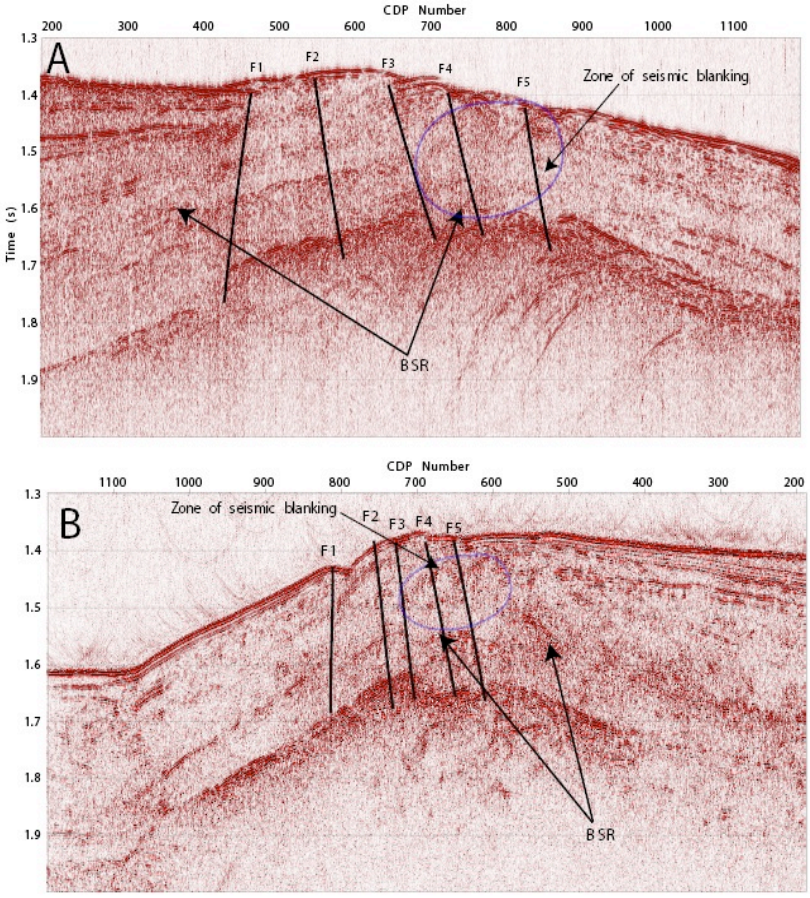

Figure 4. HRS profiles A) Coincident with Line 15. B) Coincident with Line 47. The CDP number on HRS data represents the closest CDP number of MCS data. Faults observed in the MCS data (Figure 2) have been interpreted in the HRS profiles. BSR is not observed in these data as strongly as MCS data.

Geo-Thermal Gradient Computation

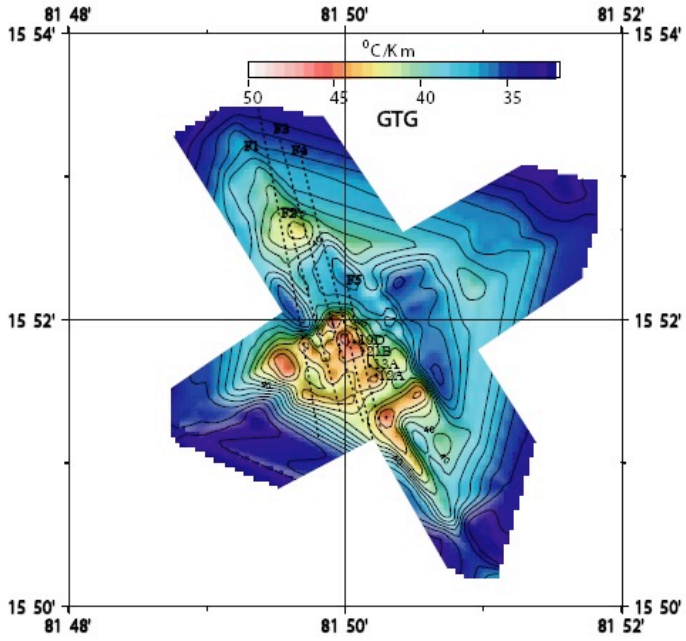

Figure 5. BSR derived GTG in the study area. The traces of fault system are shown in the plot. An abnormal increase in GTG is observed close to the fault system towards the mound.

$$q = k_{avg} GTG \quad (2)$$

Where K_{avg} and GTG represent the average thermal conductivity and the geothermal gradient. The thermal conductivity was measured on the sediment cores collected onboard JOIDES Resolution (Collett et al., 2008).

We compute GTG for all seismic profiles individually. Along the NW-SE seismic profiles such as Line 15 (Figure 2a), we observe an increase in GTG from 40 ^{o}C/km to about 45 ^{o}C/km between CDPs 700 to 1000. The observed GTG is higher close to the fault system. Likewise, along Line 47 (Figure 2b) the GTG increases from 38 ^{o}C/km to 45 ^{o}C/km between CDPs 650 to 850 close to the fault system F3-F5. The spatial distribution of GTG suggests that it increases from ~38 ^{o}C/km to ~45 ^{o}C/km towards the top of the mound. In general, anomalous GTG perturbation appears to be controlled by topography and the fault system in the study area. Further, GTG is higher towards the basinward side of the mound compared to that of landward side and *may* be related to increased width of the fault system in the basinward direction.

The mean thermal conductivity of the shallow sediment (< 200 m) in the site NGHP-01-10 measured onboard JOIDES resolution is about 0.82 W/mK with a standard deviation of 0.04 W/mK (Collett et al., 2008). The variation of the measured thermal conductivity in the shallow sediment is small (standard deviation of 0.04) and the presence of hydrate has insignificance influence on the bulk thermal conductivity (Grevemeyer and Villinger, 2001), therefore, we ignore the variation in thermal conductivity and estimate the heat flow by taking the product of mean thermal conductivity and the BSR-derived GTG. The heat flow in this region increases towards the center of the mound from 31.16 W/m2 to about 36.9 W/m2.

Interpretation of existing data

Critical to understanding of fault-controlled hydrate distribution is a bathymetric mound (between CDPs 450 to 700 in Line 15A) which is bounded by the faults (F1 and F3; Figure 2). We interpret this mound on all 12 lines and estimate its elongation to be ~5 km length in NNW-SSE direction. The maximum relief of mound (using depth conversion with waver velocity) is ~30 m. Faults bounding the mound dip towards SSE and NNW direction.The throw (from depth scaling using stacking velocities) across the faults are ~20-30 m. The shaded relief map of multibeam swath bathymetry along with the available seismic lines also shows the extent and geometry of the mound.

Horizons and faults are interpreted on all lines for stratigraphic correlation (Figure 2). The acoustic basement of the seismic profiles is marked by high amplitude, reverse polarity horizon (interpreted in magenta) which *may* represent the horizon with free gas. Other marker horizons on all lines are interpreted in orange, green, and dark blue. Major faults, F1-F5 (Figs. 2) are interpreted in all available seismic lines and the trace of the fault system is plotted on the seafloor map. The surface imprint of the fault system appears to be in NNW-SSE direction (Fig 5). Sites NGHP-01-10/21/12/13 where the presence of gas hydrates is confirmed by drilling (Collett et al., 2008) appear to be closely related to the interpreted fault system. The hydrate concentration in sties 12 and

13 was found to be far less than site 10. Although the sites are located close to each other (within a kilometer) the hydrate distribution appears to be heterogeneous; we believe that the heterogeneity is created by the fault system.

The SBP data across the topographic mound (Figure 3) suggest two distinct geological strata; parallel continuous reflectors having a mound like structure and acoustically transparent masses having semi-prolonged bottom echo with regular overlapping hyperbolae suggesting mass transport deposits. These sediment deposits are conformable to the seafloor and onlap onto the mounded finely layered sediment. The surface imprint of the major faults (F1, F3 and F4) is observed in all the illustrated SBP profiles. In the central portion of horst structure, several closely spaced faults are observed. The NGHP-01-10 site is located close to the major fault F4.

The HRS data along the inline (Line 15; Figure 2a) and crossline (Line 47; Figure 2b) seismic profiles are illustrated in Figure 4. The interpreted fault system are superimposed form the MCS lines. Due to the high frequency nature, the BSRs are not well defined except in few parts of model probably where the base of the hydrate stability zone is narrower. Amplitude blanking (reduction of acoustic impedance between layers *could be* due to the hydrates; Lee and Dillon, 2001) is widely observed. Prominent seismic blanking is observed between CDPs 650 to 950 in Figure 4a while some seismic blanking is observed between CDPs 600 to 720 in Figure 4b. Images indicate that zone of seismic blanking coincides with the region of fault system (F3-F5) further suggesting association of hydrate and the faulted region.

Preliminary discussion on existing datasets

In the KG basin, the direct evidence of the fracture filled gas hydrates comes from the X-ray images of the pressure cores. The analysis of LWD images, resistivity, and velocity logs of NGHP-01-10 site suggest the presence of gas hydrate filled high angle faults (Lee and Collett, 2009). The presence of fractures increases the secondary porosity and permeability of the sediment and result in focused fluid flow which increases the likelihood of gas hydrate formation (Ruppel and Kinoshita, 2000). In the seismic sections we have identified major fault systems (F1-F5) extending at least 200 m deep from the seafloor. The faults have created a horst-and-graben structure; the bathymetric mound is a horst. Site 10 which recovered massive hydrates is situated besides a horst structure. Several patches of locally increased velocity are observed in velocity model from modest processing of suggesting presence of hydrates in the vicinity of faults. The HRS data show blanking further suggesting presence of hydrates in the faulted stratigraphy. The lateral and vertical extent as well as the throw of the fault suggests that the fault system of this magnitude could be controlled by neo-tectonic activities and therefore could be regionally present in the K-G basin. It is therefore possible that the distribution of hydrates in the K-G basin is closely linked to fault distribution.

Indirect estimation of GTG and heat flow from the depth of the gas hydrate stability zone has been used to understand the thermal regime of the continental margins (Hyndman

and Davis, 1992; Grevemeyer and Villinger, 2001). The heat flow (q) primarily depends on the age of the crust (Stein and Stein, 1994) and can be calculated as,

$$q = 48 + 96 * e^{-0.0278*t} \quad (3)$$

Where t represents the age of the crust in Ma and the equation is valid for t > 55 ma. The study area is located in M11 magnetic anomaly (Ramana et al., 1994); hence we can assume the age of the crust to be ~ 130 Ma. Substituting the value for age of the crust in equation (3), we obtain the background heat flow to be about 50 m W/m2. The heat flow also shows significant dependence on the nature of sediments, the sedimentation rate and age of the sediment. Assuming 100 % clay sediment (Collett et al., 2008) and a sedimentation rate of ~ 20-30 m/Ma, the correction factor will be of the order of 35-40 %. After accounting the correction due to sediment, we estimate the background heat flow to be in the range of 30 -32.5 m W/m2. The background GTG estimated from heat flow assuming mean thermal conductivity of 0.82 W/mK will be about 36-40 ^{o}C/km.

BSR-derived GTG may differ from the actual GTG due to uncertainty in calculation of phase curves if the gas composition of the hydrates is not known, uncertainty in calculating the bottom water temperature, inaccuracy in estimating the depth of the reflectors due to unavailability or errors in velocity model and error in BSR depth estimation due to seismic anisotropy. Moreover, such discrepancy may also occur if the BSR depth does not correspond to the base of the hydrate stability zone due to capillary force arising in fine grained sediment (Ruppel, 1997). Additional errors in heat flow estimate may come from the uncertainties in estimating thermal conductivity and the effect of gas hydrates on thermal conductivity.

Preliminary processing and traveltime inversion

From the NGHP-01 well report (Collette *et al* 2006) following inferences relevant to our subtask are as follows:

1. Initially, none of the three wells (10D, 12A, and 13A; Figure 6) showed any obvious lithological control on hydrate distribution.

2. Of the three wells only 10D penetrated the BSR; no free-gas was encountered.

3. Well 12A which was drilled 500m SE of 10D could only be cored (no logging was done). Chlorinity analysis suggests hydrates in 10D do not extend to 12A

4. In the de-pressurization test, 12A recovered ~20% of hydrates as compared to 10D.

5. Well 13A which was drilled 150m SE of 10D could only we logged (no cores were available). The volume of hydrates in 13A was similar to that in 10D.

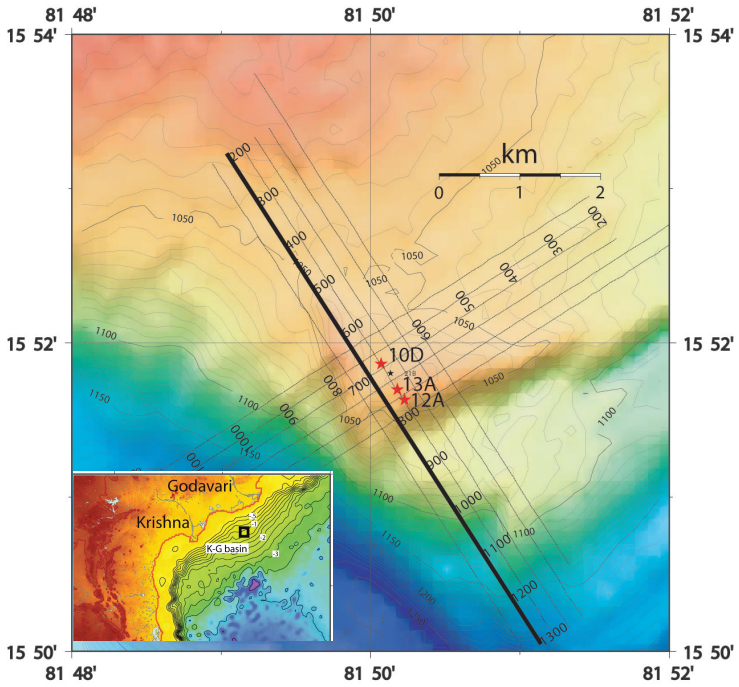

Figure 6. Bathymetry map of the study area. Location with respect to the Indian east-coast is shown in inset. Seismic line released for this study by Indian Govt. is shown in bold. Other available survey lines for future release are shown in grey. Wells 10D, 13A, and 12A, were logged/cored during NGHP-01 expedition. Data from these wells are in public domain.

Travel time inversion and pre-stack depth migration

The composite inversion-migration method used in this work is same as the Unified Imaging (UI) method developed by (*Jaiswal and Zelt*, 2008). This method estimates a structurally consistent velocity and reflectivity model starting with standard processing methods. UI, in this work, is essentially a composite of reflection tomography and Kirchoff's pre-stack depth migration (PSDM).

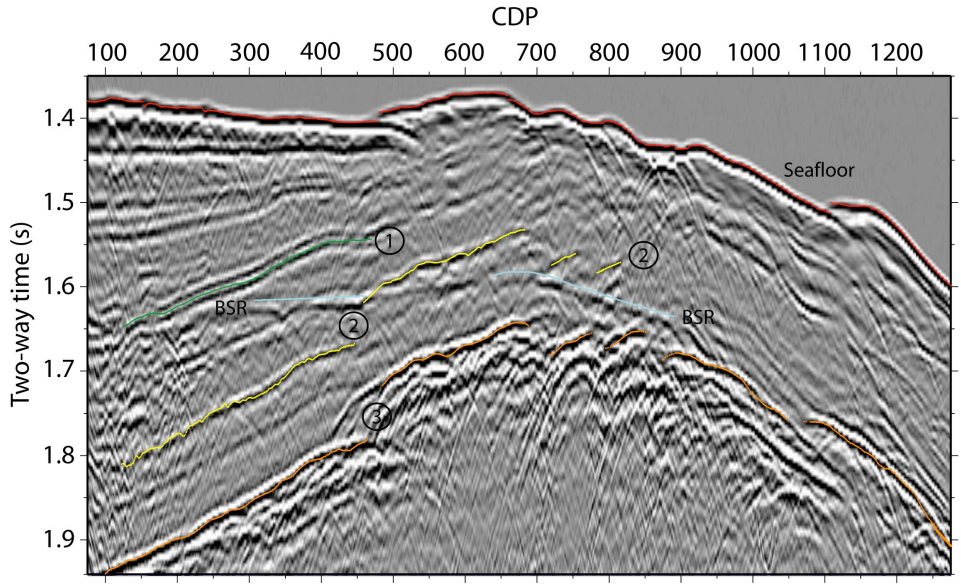

Figure 7. Stacked data. Seafloor, and reflectors labeled 1 – 3 are used in inversion. The BSR is interpreted in blue and is not used in inversion.

UI begins with generation of the stack (Figure 7) using the best possible stacking velocity model and interpretation of events to be used in inversion. Interpretation of the stacked data (Figure 2) is inverted as zero-offsets arrival times. The stacking velocity model is converted to depth using Dix's smooth gradient method (*Dix*, 1955), Vel0 (Figure 8a). This model is used for depth migration and identifying the same events that were interpreted in the stacked data. Following this, wide-angle traveltimes corresponding to these reflectors are picked in the raw shot gathers. The geometry of the reflectors for inversion of wide angle data are interpretation of the depth migrated images (Figure 9).

By inverting the wide-angle traveltimes, UI updates the interval velocity model. Repeated cycles of traveltime inversion and depth migration are performed; a "cycle" refers to a single run of joint inversion followed by depth migration. The horizons are modeled as floating reflectors (*Zelt*, 1999). The updated velocity model is then used for depth migration and zero-offset inversion. For the zero-offset inversion, the velocity model is maintained stationary. The interpreted horizons are compared with the corresponding inverted horizons by computing their normalized RMS distance, ***j***. In case this distance is found to exceed unity, the updated velocity model and interpretation from the current cycle is used as the initial velocity model and horizon depths for the next cycle. The cycles are repeated until a value of unity is achieved for ***j***. In this paper three cycles were required for ***j*** to converge to unity.

n UI, the root-mean-square (RMS) distance, *d*, between the interfaces from the zero-offset inversion and the corresponding interfaces from the interpretation of the depth migrated image;

$$\boldsymbol{d} = \frac{1}{n}\sqrt{\sum_{i=1}^{n}(z_i^p - z_i^v)^2} \qquad (4)$$

In equation (4) z^p and z^v are the interpreted and inverted interfaces and n is the number of nodes at which the interfaces are compared. Due to the limited frequency bandwidth of the depth image and the presence of random and coherent noise, the interpreted horizons in the depth image are associated with uncertainties. A coefficient of congruence, $\boldsymbol{j}$, is therefore defined to account for the uncertainties and used as a measurement of the proximity of a given velocity model to the true velocity model;

$$\boldsymbol{j} = \frac{1}{n}\sqrt{\sum_{i=1}^{n}\left(\frac{z_i^p - z_i^v}{\sigma_i}\right)^2} \qquad (5)$$

In equation (5) σ_i is the uncertainty assigned at the i^{th} node (5m in the work). A value of unity for $\boldsymbol{j}$ implies that the structural discrepancies have been fit to the level of the interpretational uncertainties and the unified imaging is said to have converged at this point. Similarly, a value of $\boldsymbol{j}$ greater than unity implies that the velocity model requires improvement and a value less than unity suggests that the data have been overfit.

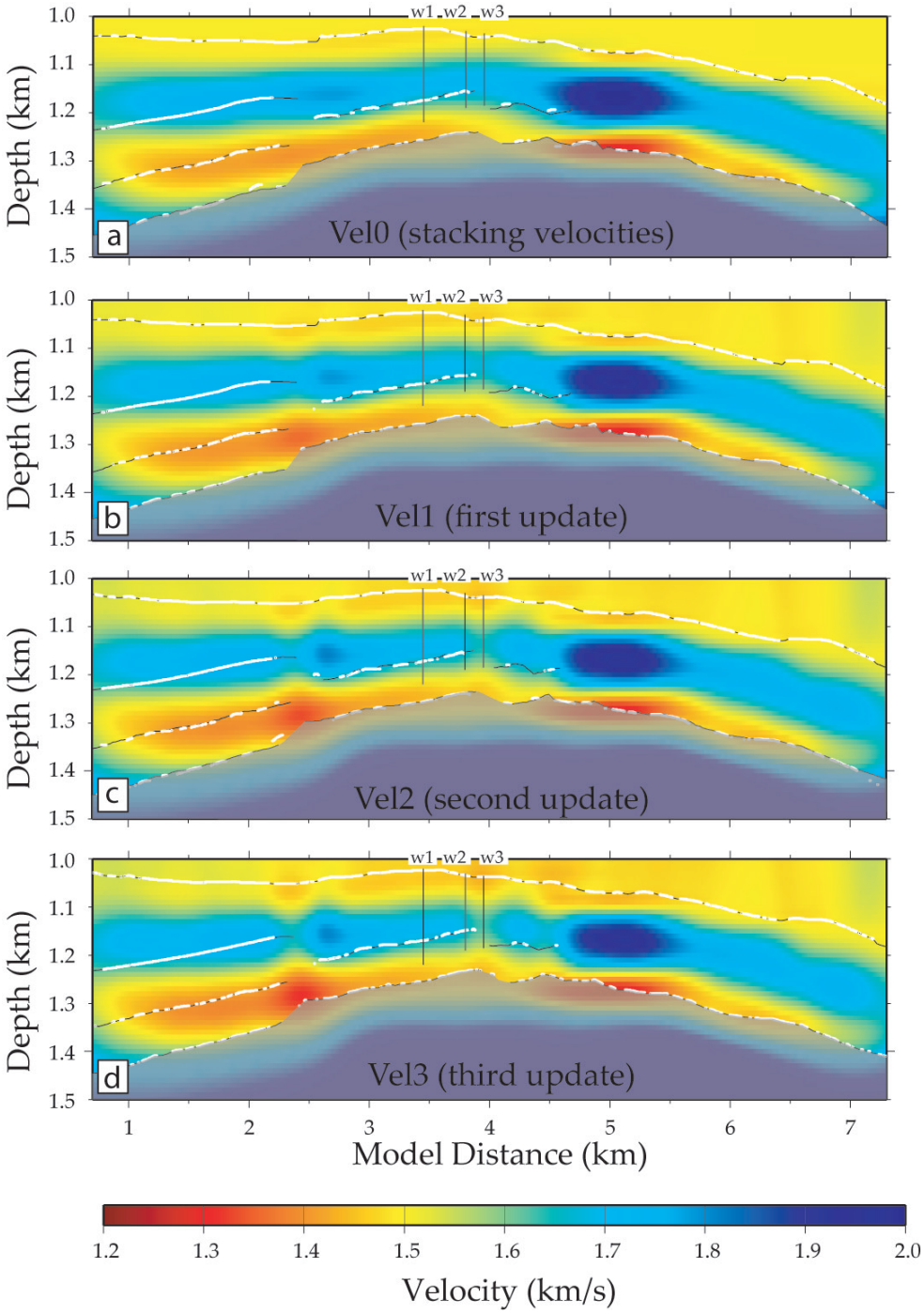

Figure 8. Velocity models from composite inversion-migration method. A) Starting velocity model from conventional processing. B) – D) Updated models from inversion of reflection traveltimes. In A) – D) the horizons picked for inversion are shown in with solid black line. The inverted horizons are overlaid in white. Model in d) is considered preferred as the picked and inverted horizons have reasonable overlap. In A–D, parts of the model not covered by rays are shaded in grey. W1 – 3 represent wells 10D, 13A, and 12A respectively. As observed in the cores, 10D and 13A (W1 and W2) appear to sample the same hydrate patch while 12A (W3) appears to be disconnected.

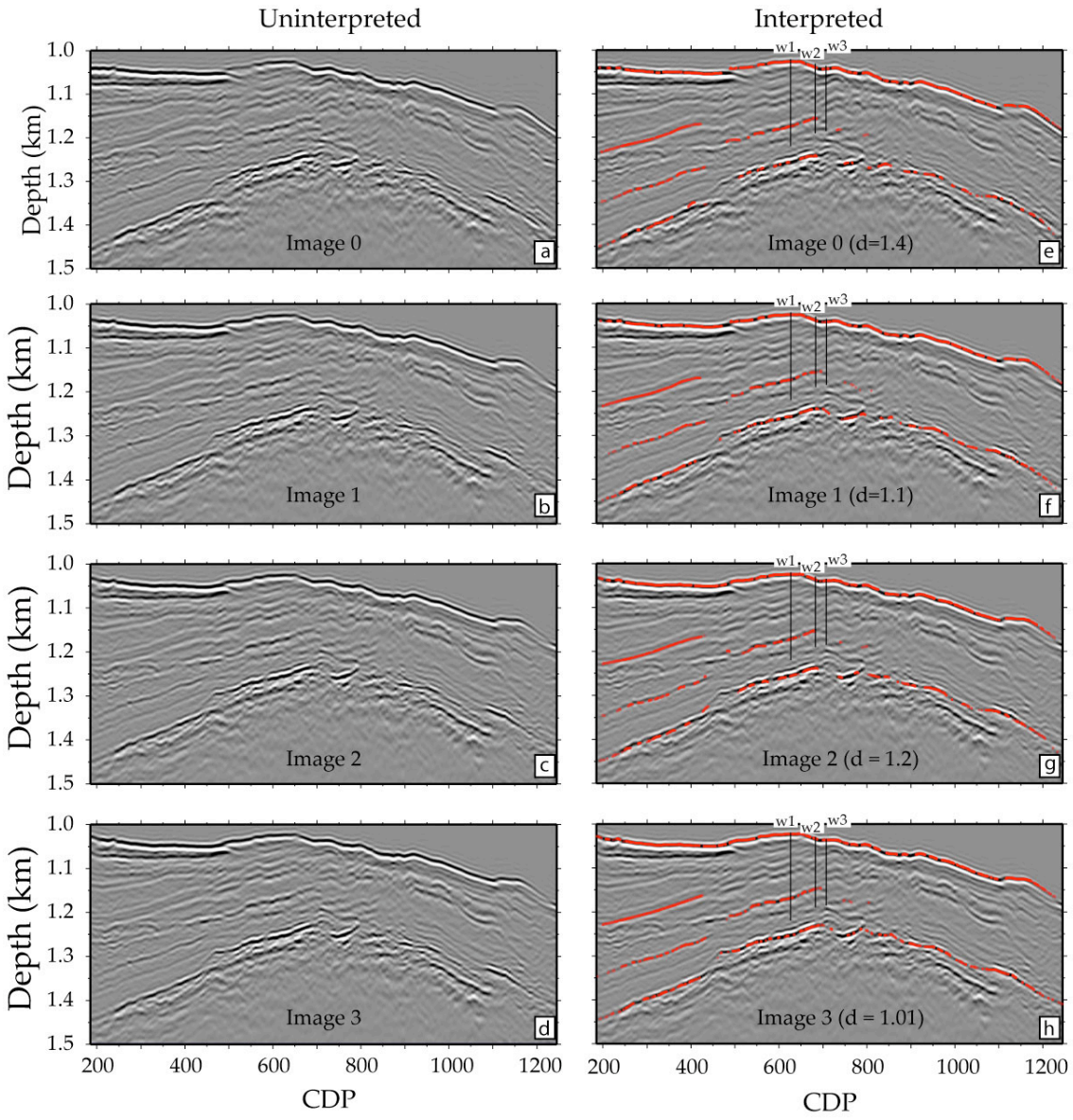

Figure 9. Depth Migrated Image. A) Image0 – D) Image3 are pre-stack depth-migrated reflectivity images using Vel0 – Vel3 velocity models in Figure 2 respectively. E) – H) are same as A) – D) with inverted interface (in red) and well overlaid. In E) – H) ***d*** is a parameter for congruency test. Note that Image 3 has the best agreement between observed and inverted interfaces. W1 – W3 are wells 10D, 13A, and 12A respectively.

Unified imaging utilizes (*Zelt et al.*, 2006) method of traveltime inversion. Traveltimes in this method are computed on a regular grid by solving the Eikonal equation using the finite-difference scheme of (*Vidale*, 1988) modified to account for large velocity gradients (*Hole and Zelt*, 1995). Raypaths, in accordance with Fermat's principle, are determined by following the steepest gradient of the time field from a receiver to a source. The inverse modeling part linearizes the non-linear traveltime inverse problem with the help of an initial model that is iteratively updated based on the discrepancy between the observed and the predicted traveltimes.

The inverse modeling formulates an objective function which is the L_2 norm of a combination of data errors and model roughness (second-order partial derivative and minimizes it to compute the model updates. For a given observed data vector d_{obs} and predicted data vector d_{pre}, the objective function for simultaneously constraining the velocities and the interfaces is expressed as:

$$E(s,z) = \delta d^T C_d^{-1} \delta d + \lambda\{\beta[\delta s^T C_{s,h}^{-1} \delta s + s_z \delta s^T C_{s,v}^{-1} \delta s] + (1-\beta)[\delta z^T C_{z,h}^{-1} \delta z]\} \quad (6)$$

In equations (6) $\delta d = d_{pre} - d_{obs}$ are the data errors and $\delta s = s - s_0$ is the slowness perturbation vector being solved for; s_0 is the starting slowness vector, C_d is the data covariance matrix; covariance matrices $C_{s,h}$, and $C_{s,v}$ measure horizontal and vertical roughness of the slowness perturbation, respectively, l is the trade-off parameter, and s_z determines the relative importance of maintaining vertical versus horizontal model smoothness. $\delta z = z_0 - z$ is the interface depth perturbation vector being solved for; z_0 is the starting interface vector and $C_{z,h}$ is the covariance matrix that measures the interface roughness. β determines the relative weights of slowness and interface regularizations. Regularization is implemented by scaling with the inverses of the data and model (slowness and interface) space covariance matrices in an attempt to obtain the smoothest model appropriate for the data errors (*Scales et al.*, 1990). The data misfit in traveltime inversion is assessed using the normalized form of the misfit parameter, the chi-squared error, χ^2, (*Zelt*, 1999). Assuming the errors in the observed picks are uncorrelated and Gaussian in nature, a value of χ^2 equal to 1 indicates that the observed traveltimes have been fit to within their assigned uncertainties.

Due to the inherent velocity-depth tradeoff in the joint inversion, achieving a χ^2 value of unity in every cycle is not the ultimate goal. Instead the overall geological sensibility of the updated velocity model is given more emphasis. The joint inversion is halted when the updates start yielding structures that appear to be geologically implausible even if the convergence has not been reached. For given updates in the velocity model, updates in the corresponding interface depths are sought through PSDM. As the velocity model progressively becomes close to the true velocity model, the migrated image also positions the interfaces closer to their true depth locations. Thus, the non-linear and non-unique nature of unified imaging as a whole calls for close monitoring.

A combination of preferred velocity model (Vel3; Figure 8d) and the corresponding depth image is displayed in Figure 10. Region shaded in blue above the BSR could represent hydrate bearing sediments. The dark blue patch at CDP ~900 coincides with a zone of low reflectivity and could represent concentrated hydrate deposits. The exact character of the resistivity log cannot be explained with the velocity model from UI. It could be partly due to lateral changes in hydrate concentration that do not allow a proper well projection on the seismic line or low resolution of the velocity model itself. The resolution of the velocity model is improved using waveform inversion.

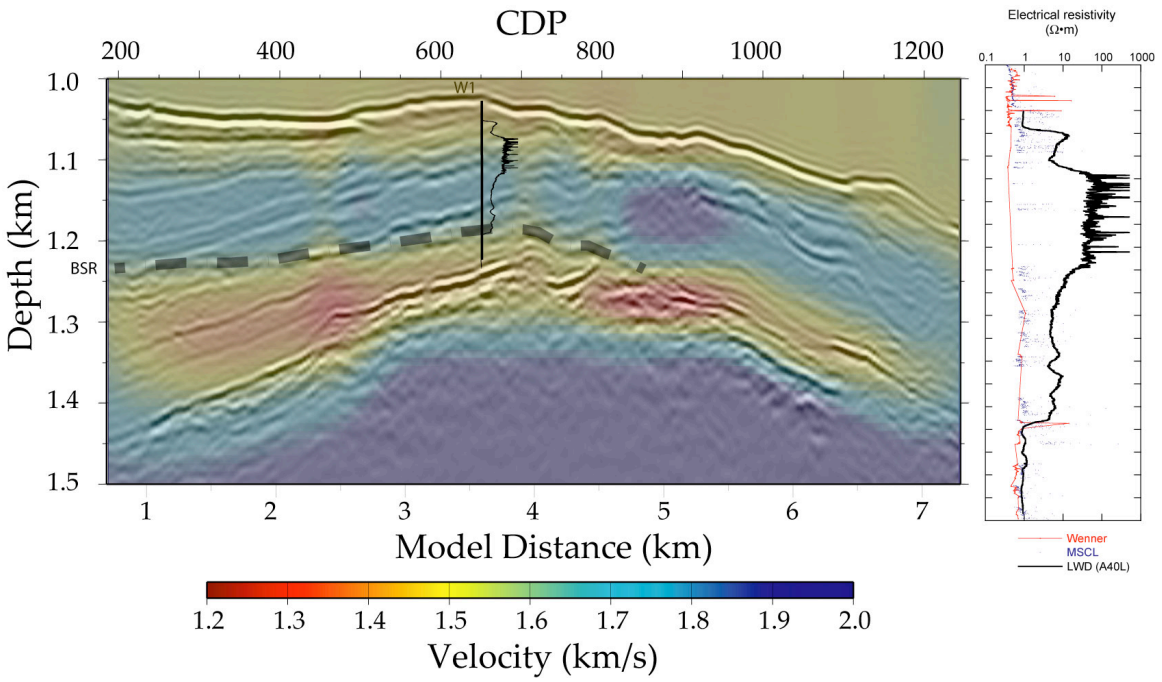

Figure 10. Composite of preferred velocity model and the corresponding depth image from Unified Imaging. BSR is marked in grey dashed line. The resistivity log from 10D is overlaid. The BSR in the log coincides with the BSR in seismic image validating the velocity model. The well log is displayed beside the composite image.

2-D visco-acoustic waveform inversion

Similar to traveltime inversion, full waveform inversion (FWI) estimates an earth model that will simulate a seismogram that matches the observed seismogram. In this work, waveform inversion is performed in the frequency domain. This paper uses the (*Pratt*, 1999) method of waveform inversion. The method begins with an initial guess of the earth model, known as the starting model, and iteratively improves it based on the differences between the predicted and real wavefield, known as the data errors. Model updates in the method are estimated by correlating the back-propagating data residuals with the forward-propagated wavefields. The method operates in the frequency domain. We use the FWI method to compute P-wave velocity (V_P) and P-wave attenuation (Q_P).

The wavefield in the forward problem is computed by solving the wave equation in the frequency domain using the finite-difference mixed-grid approach of (*Jo et al.*, 1996). The wave equation used in the Pratt (1999) method automatically accounts for backscattering and wide-angle effects. For an individual angular frequency ω, the wave equation is expressed as:

$$\mathbf{d}_{\mathbf{pre}}(\omega)=\mathbf{S}^{-1}(\omega)\mathbf{f}(\omega) \qquad (7)$$

In equation (7), $\mathbf{d_{pre}}$ is the complex-valued predicted wavefield vector from the model vector **m**, **S** is a complex valued impedance matrix that contains information about the physical properties of **m**, and **f** is the source term vector. In this paper a 2-D acoustic, isotropic approximation of the wave equation is made. Additionally, a relation between density and velocity was estimated from the well logs and attenuation is ignored.

The inverse problem minimizes the L_2 norm of the data errors, expressed in an objective function, *E*.

$$E(\mathbf{m})=\frac{1}{2}\delta\mathbf{d}^{t}\delta\mathbf{d}^{*} \quad (8)$$

In equation (8), the data errors $\delta\mathbf{d}=\mathbf{d_{pre}}-\mathbf{d_{obs}}$ where $\mathbf{d_{obs}}$ is the observed wavefield. In equation (8) **d** is a vector comprising strength of the frequency components obtained by a Fourier transform of the time domain data, the superscript *t* represents matrix transpose, and the superscript * represents the complex conjugate. The Talyor series expansion and simplification of equation (8) in the neighborhood of the model, **m**, leads to the following relationship in the k^{th} iteration between the starting, $\mathbf{m}^{k}$, and the updated, $\mathbf{m}^{k+1}$, model:

$$\mathbf{m}^{k+1}=\mathbf{m}^{k}-\alpha^{k}\nabla E^{k}(\mathbf{m}) \quad (9)$$

In equation (9), $\nabla E(\mathbf{m})$ is the gradient direction and α is the step length that is chosen by a line search method. The key in the Pratt (1999) method is to express the gradient direction as:

$$\nabla E(\mathbf{m}) = \frac{\partial E}{\partial \mathbf{m}} = Real\{\mathbf{F}^{t}[\mathbf{S}^{-1}]^{t}\delta\mathbf{d}^{*}\} \quad (10)$$

In equation (10), **F** is known as a virtual source which can be understood as the interaction of the observed wavefield, $\mathbf{d_{obs}}$, with the perturbations in the model, **m**. Individual elements of the virtual source are defined as $\mathbf{f}^{i}=-\frac{\partial \mathbf{S}}{\partial \mathbf{m}_{i}}\mathbf{d}_{obs}$, where $\mathbf{f}^{i}$ and $\mathbf{m}_{i}$ are the i^{th} virtual source and model parameter. Equation (10) is the mathematical expression of the back-propagated residual wavefield, $\left[\mathbf{S}^{-1}\right]\delta\mathbf{d}$, being correlated with the forward propagated wavefield, *F*. The computational complexity in waveform inversion dominantly rests on the computation of $\mathbf{S}^{-1}$. For multiple source problems, $\mathbf{S}^{-1}$ is best solved using LU decomposition (*Press et al.*, 1992) and ordering schemes such as nested dissection that take advantage of the sparse nature of **S** (*Marfurt and Shin*, 1989).

Attenuation in Pratt (1999) method is mainly reflective of absorption which is a characteristic of the material such the grain size, the mineralogy and fluid saturation as well as the propagation frequency. Attenuation is included in inversion by specifying the

velocity model (**m**) as a complex quantity (**m = m$_r$ + *i*m$_i$**), where the imaginary (**m$_i$**) and the real (**m$_r$**) parts are related as through the seismic quality factor **Q**, which is the inverse of attenuation, as:

$$m_i = -\frac{m_r}{2Q} \tag{11}$$

The stopping criteria in waveform inversion are somewhat qualitative. The waveform inversion seeks a model that can explain as many features of the real wavefield as possible within the range of the wavenumbers being accounted for. In general, for a given frequency (or a group of frequencies), iterations are halted when the objective function ceases to reduce any further. In the multiscale implementation, the inversion process is halted when incorporating higher frequencies appears to make the model noisy. In the end, a visual assessment of the updated model for its compatibility with the expected stratigraphy and comparison of the predicted wavefield for their similarity to the real wavefield serve as stopping criteria.

Waveform inversion also requires a source function to compute the model updates. The Pratt (1999) method estimates the source function with the help of the current model. Thus, waveform inversion begins not only with a starting V_P and Q_P^{-1} model but also a starting source signature. For a given data bandwidth, the V_P and Q_p^{-1} models are updated using the *a priori* source signature, following which the source signature is updated using the updated models. As waveform inversion iteratively incorporates higher wavenumbers, higher frequencies are incorporated in the source signature and the resolution of the recovered model is enhanced.

Imaging through waveform inversion requires that wavenumbers from zero to the highest value in the data be present in a continuum. (*Wu and Toksoz*, 1987) demonstrated that inversion of a single frequency covers a finite range of wavenumbers. Following their results, (*Sirgue and Pratt*, 2004) demonstrated that inverting a few carefully chosen frequencies is equivalent to inverting all frequencies available in the seismic survey (efficient waveform inversion). We have used a similar strategy to determine groups of frequencies (Table 1) that can be inverted to image the required range of wavenumbers.

Table 1. Frequency groups used for visco-acoustic waveform inversion (Figures 11 and 12)

Group	Frequencies (Hz)
1	8.4, 8.8, 9.2
2	9.6, 10.0, 10.4
3	11.2, 11.6, 12.0
4	13.2, 13.6, 14.0
5	15.6, 16.0, 16.4
6	17.6, 17.2, 17.6

Waveform inversion also requires a source function to compute the model updates. The Pratt (1999) method estimates the source function with the help of the current model. Thus, waveform inversion begins not only with a starting model but also a starting source signature. For a given data bandwidth, the velocity model is updated using the *a priori* source signature, following which the source signature is updated using the updated velocity model. As waveform inversion iteratively incorporates higher wave numbers, higher frequencies are incorporated in the source signature and the resolution of the recovered model is enhanced.

FWI began with a determination of the source signature using the starting model and the scaled real data. Following this, 8.4 - 18.4 Hz data were successively inverted in 6 steps (Figure 11). In each step, 3 frequencies spaced 0.4 Hz apart were inverted simultaneously. Selection of frequency groups was selected by closely monitoring the evolving FWI models. The updated model from each step was used as starting model for the next step. Prior to updating the model in each step, the source signature was recalculated using the updated model from the previous step. While model updates are obtained using limited frequency bandwidth, all frequencies are inverted for the recalculation of the source signature. Iterations were continued in each step until the reduction in the objective function's value was less than 0.1%. Successive incorporation of higher frequencies in each step yielded a higher wave number solution of V_P.

Inversion of the lowest frequency group (8.4-9.2 Hz) yields a smooth and coherent V_P model (Figure 2b). We interpret high V_P (> 1.7 km/s) features within top 200m of the sediment column as hydrate bearing sediments. Successive inversion of higher frequencies localizes these high V_P features but also makes it increasingly difficult to distinguish between genuine stratigraphy and model artifacts (Figures 11b through g). We lose confidence on our model starting with inversion of 17.6 Hz (Figure 11g). The source updates obtained in each step of inversion was found to be minimal most likely due to the presence of dominating synthetic transmission coda in the water column that remains unchanged throughout inversion.

The final model from V_P inversion (Figure 12f) was used estimating Q_P^{-1}. The initial Q_P^{-1} model is set to imply zero attenuation. Inversion of the lowest frequency group (8.4-9.2 Hz) yields a smooth Q_P^{-1} model (Figure 3a). Successive inversion of higher frequencies localizes the Q_P^{-1} features (Figures 3b through f). For consistency, the inversion frequency groups were kept same as in the V_P inversion. As with the V_P inversion we loose confidence staring inversion of 17.6Hz (Figure 3f). Both source and V_P model updates obtained in each step of Q_P^{-1} inversion was found to be minimal most likely due to the higher sensitivity of FWI towards Q_P^{-1}.

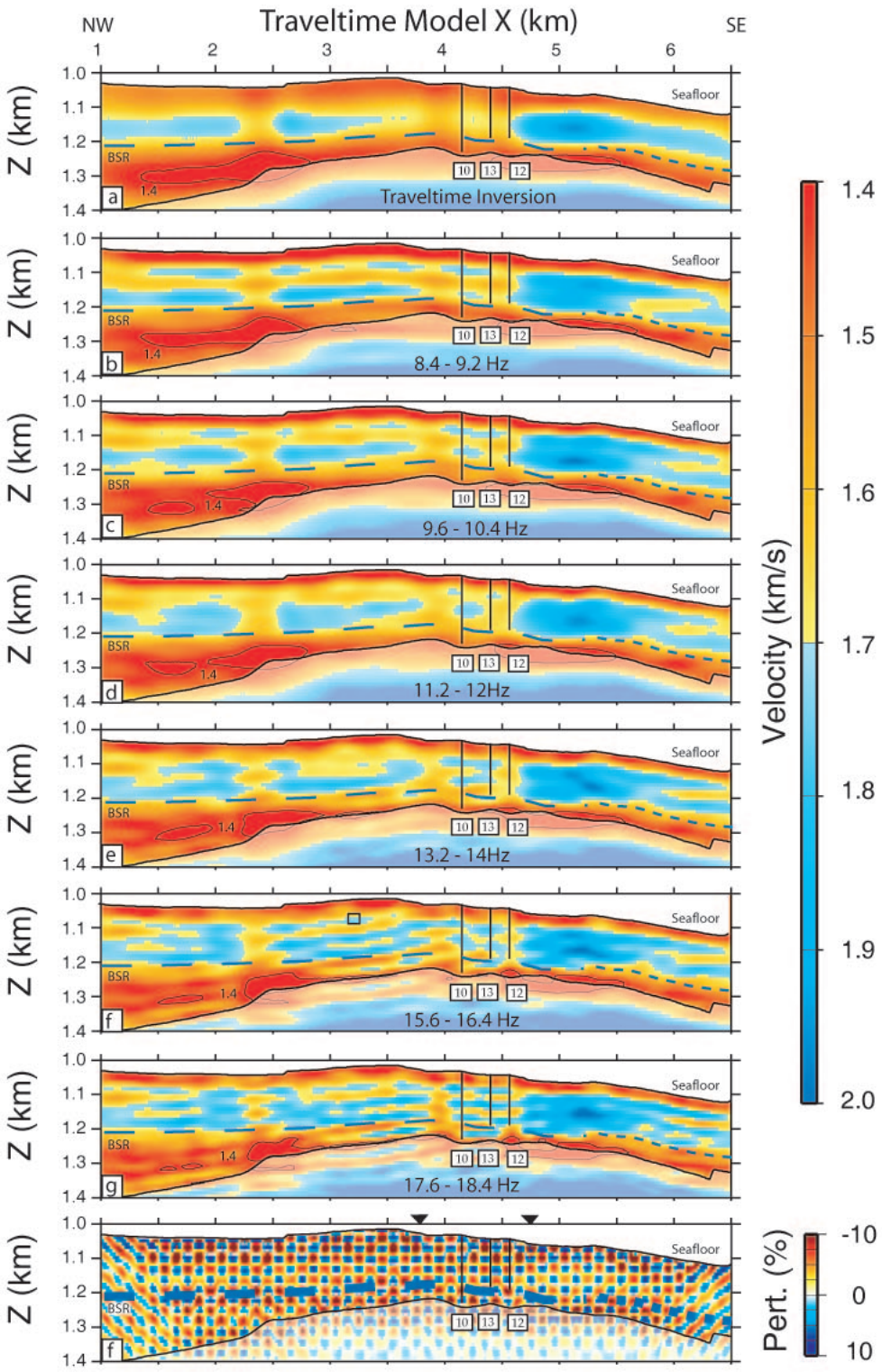

Figure 11. V_P Models from waveform inversion. Model from inversion of 15.6 – 16.4 Hz is chosen as the preferred model.

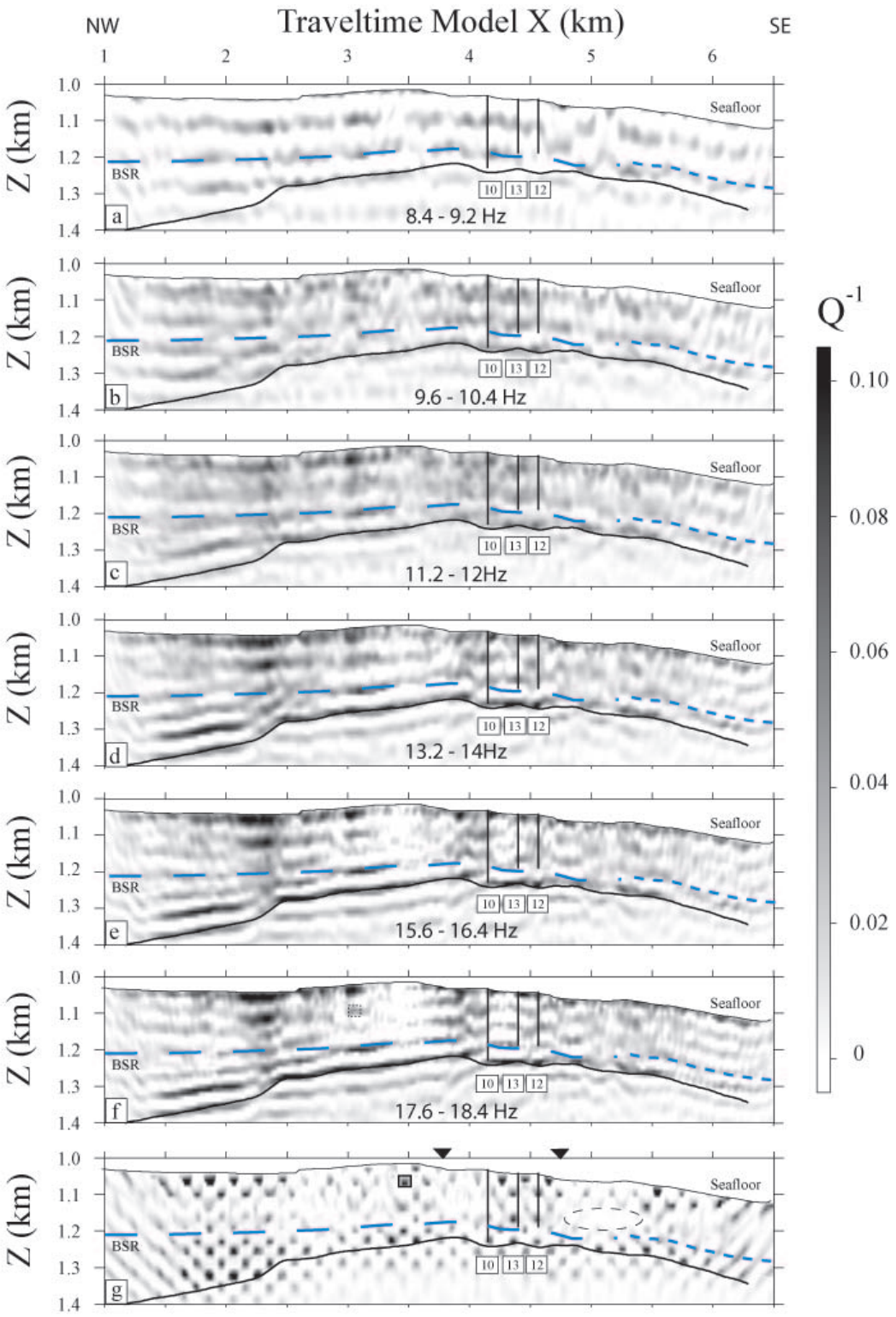

Figure 12. Q_P models from waveform inversion. Model from inversion of 15.6 – 16.4 Hz is chosen as the preferred model.

The preferred waveform model (Figure 11f) is jointly interpreted with the depth image (Figure 9d). The composite image suggests that in parts of the model between CDPs 500 and 900 a) hydrates prefer certain stratigraphic sections; and b) some parts appear to be hydrate-free. The reasons behind variation of hydrate concentration are currently under investigation however some speculations are presented below.

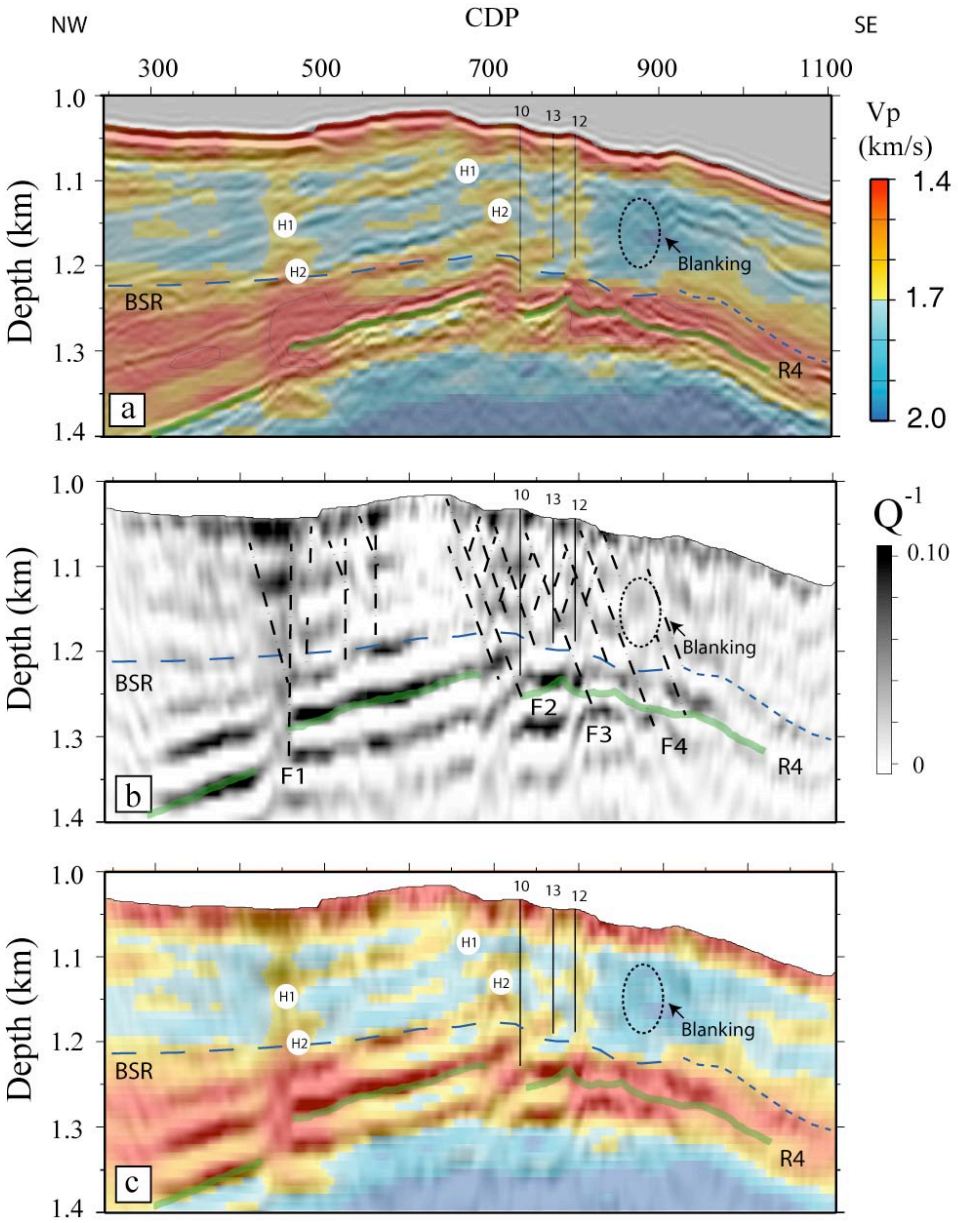

Figure 13. Composite interpretation. (a) V_P (Figure 11f) and reflectivity (Figure 9d) overlay. High amplitude horizons H1 and H2 are labeled. High velocity is associated with high reflectivity along H1 and H2 and well as low reflectivity in the seismic blanked zone, outlined in dashed line. (b) Q_P (Figure 12e) and fault structure (Interpretation from Figure 4) overlay. Q_P is proportional to fault density. (c) V_P and Q_P overlay. In general, V_P is proportional to Q_P, except along H1 and H2 suggesting hydrates saturating the

pore spaces may reduce Q_P. In (a) – (c) the BSR is interpreted after Figure 10 and the projected sites NGHP-01-10 – 13 are labeled.

V_P and reflectivity overlay

We interpret V_P higher than 1.7km/s within the GHSZ to indicate hydrates and velocities lower than 1.4km/s below the GHSZ to indicate free gas. The final FWI V_P model (Figure 11f) shows that hydrate bearing sediments have a patchy distribution. The hydrate distribution is be genuine because the projected Site NGHP-01-10 is associated with hydrate bearing sediments while the projected Site NGHP-01-12 is associated with hydrate free sediments which is consistent with the lower volume of hydrates recovered at Site NGHP-01-12 compared to Site NGHP-01-10 (2% versus 20% by pore volume). V_P of 1.5 km/s or less within the top 20 m of the seafloor along the model could represent the sulfate – methane reduction zone.

A composite of the final V_P model (Figure 11f) and depth image (Figure 9d) shows hydrates have no apparent relation with the stratigraphy except below the bathymetric mound in particular with high amplitude horizons H1 and H2 (Figure 13a). We suspect that H1 and H2 have high amplitudes due high hydrate saturation. Unfortunately, the FWI V_P model does not have enough resolution to confirm this. We speculate that H1 and H2 are coarser grained (possible diatom bloom) in an otherwise fine-grained background making them relatively preferable for hydrate precipitation within pore spaces (Rempel, 2011). While high velocities are associated with high amplitudes along H1 and H2, they are also associated with the seismic blank zone (CMP 825 – 925 and model depth 1.1 – 1.2 km) which is nominally attributed to grain cementing hydrates (Holbrook *et al.*, 1996; Hornbach *et al.*, 2003). It is likely that hydrates are present in at least two states along the seismic profile.

Attenuation and fault overlay

Within the GHSZ, attenuation can be potentially affected by at least three aspects of the geology – free gas, faults, and hydrates. It is difficult to analyze the effect of individual factors from a common Q_P^{-1} (Figure 12; hereafter referred to as attenuation only) model but different parts of the attenuation model may have more influence from one factor than the other. While free gas and faults are known to enhance attenuation, the effect of hydrate is debatable. In general, attenuation is higher below the BSR which is consistent with the presence of free gas. Attenuation below the BSR has a layered appearance which closely agrees with the stratigraphy (Figure 13b) suggesting that the free gas distribution may have stratigraphic control. This feature of the geology was not evident in the FWI V_P model is new information provided by attenuation inversion. The overall attenuation reduces within the GHSZ but maintains a layered appearance which is occasionally interrupted by faults (Figure 13b). The layered structure of the attenuation can be linked with hydrates (see below). With current resolution, it is difficult to examine of effect of individual fault gauges on attenuation. However, the fact that faults increase attenuation is suggestive from the zone below the mound (CMP ~600 – 650) within the GHSZ where a decrease in attenuation is accompanied by a decrease in fault density.

Q_P^{-1} (attenuation) and V_P overlay

Attenuation and V_P do not have a consistent relation within the GHSZ (Figure 13c). In general, little to no deviation of attenuation from an initial zero value is associated with hydrate bearing sediments (V_P >1.7 km/s); this is most apparent below the mound such as along H1 and H2 (Figure 13c). However, at projected Site NGHP-01-10, where elevated velocities are most confidently linked to hydrates, a reasonable attenuation is observed. A similar attenuation at the projected Site NGHP-01-12 which associated with low hydrate saturation is also observed. We conclude the attenuation between CMP 650 – 850 (vicinity of Site NGHP-01-10) and similarly between CMP 450 – 600 is mainly due to faults with no implications on hydrates. We suspect high attenuation along F1 is also due to free gas (see below). High attenuation due to faulting and fluid migration associated with diapirism has also been observed in the Blake Ridge (Taylor *et al.*, 2000). At the seismic blank zone (Figure 13c), which is being attributed to grain cementing hydrates, although attenuation in this zone is not fully resolved (Figure 12g) an increase in attenuation is likely.

A possible explanation of attenuation variations within the GHSZ could be the changing state of hydrates within their host sediments. It is less likely that hydrates are present as cement other than at the seismic blank zone. In other parts of the model, hydrates either nucleate and grow within the faults or saturate the pore-spaces. We posit that in fine grain sediments, such as in the study area, small volume of hydrates can completely clog the pore throats thereby increasing the rigidity of the sediment matrix and decreasing the attenuation. Hydrates present as pore-filling components will not increase the V_P significantly over the background if the overall porosity is low. However, similar volume of hydrates as grain-coating cement can lead to a relatively higher V_P such as that observed in the seismic blank zone and at the same time increase attenuation depending on their saturation (Priest et al., 2006).

Free gas within the GHSZ

The NW termination of hydrate bearing horizons H1 and H2 occur near CMP ~450 at a near-vertical hydrate-free zone which appears to be immediately underlain by free gas bearing sediments (Figure 13a). High attenuation within the GHSZ at this location could be suggestive of free gas. We propose the following explanation: faults penetrating through the sediment column at this location could be channeling saline, gas-rich fluids from a deeper source into the GHSZ which. Liu and Flemings (2006) also show that it is possible to elevate salinity with hydrate formation such that free gas, water and hydrate can coexist in the GHSZ.

General applicability of FWI

FWI has at least three advantages over traveltime inversion in this application. First, significant gain in terms vertical resolution is achieved from FWI. For example, the final FWI V_P model suggests at least two distinct hydrate-bearing stratigraphic units below the bathymetric high with were not resolved in the traveltime model. Although these units are present in the depth image, they could only be interpreted as hydrate bearing using the FWI V_P model. Second, FWI model estimates the V_P magnitude more accurately than traveltime inversion as shown by the V_P comparison in Figure 1 inset. Third, traveltime inversion cannot estimate attenuation. Attenuation effects the phase of the seismic data and occasionally, when free surface is involved, the phase changes can create significant shifts in arrival times. However, in this application, attenuation updates are subtle and to the best of our estimate the uncertainty assigned to traveltime picks will include shifts due to phase changes. The amplitudes, on the other hand, are sensitive to attenuation making the use of FWI a necessity.

In a recent experiment Delescluse et al. (2011) apply nonlinear acoustic inversion to long offset (9 km long streamer) data from the Scotia margin to image hydrate bearing sediments within 300 m of the seafloor in water depths 1600m. They invert 8 – 24 Hz data and achieve ~30m vertical resolution. Authors such as Cheng *et al.* (2006), LeBlanca *et al.* (2007), Petersen *et al.* (2007), Schnurle *et al.* (2004), Zillmer *et al.* (2005b) and Wang *et al.* (2010) show the utility of long-offset data in imaging gas hydrates. In this paper we show that high (~30m) vertical resolution can be obtained with narrow aperture (offset = 1.2 X target depth) survey. The main difference could be in the methodology of creating our starting model. Most of the references cited above which use starting model and a local decent method create their starting models using turning rays tomography from first arrivals in OBS or stacking velocity analysis of MCS data. Our model building method for starting model (Paper I) includes reflection ray-paths from multiple horizons providing a better ray coverage of the tomography grid, but more importantly the combination of reflection tomography with depth migration ensures that the starting model is kinematically correct. Further our method for windowing the starting model ensure a continuous wavenumber converge in FWI.

Basin-wide prediction of hydrates based on V_P and attenuation attributes could have wider implications on their global estimates. Volumetric measurements of hydrates have either been statistically driven based on average extent and thickness of the GHSZ, porosity, gas yield, total organic carbon, or more simply, the BSR amplitudes (Milkov, 2004). In faulted sediments, such as in the KG basin hydrates and BSR cannot be correlated. Further, hydrates appear to be changing their state along the seismic profile. In such case, V_P and Q_P models provide better opportunities of constraining the rock physics model of hydrates in turn leading to a more appropriate quantification.

Rock physics modeling

Nomenclature

R: Average radius of the grain

ρ_S: Bulk density of solid phase.

ρ_f: Bulk density of fluid (brine).

ρ_h: Bulk density of hydrate.

$\overline{\rho}_f$: New bulk density of the pore fluid mixture.

ρ_b: Total bulk density of saturated sediments.

ϕ_t: Original total porosity

$\overline{\phi}$: New total porosity (after hydrate is added to the mineral frame).

ϕ_c : Critical porosity

S_h: Hydrate saturation of the pore space

C_h: Volumetric concentration of hydrate in a unit volume of rock

K_S: Bulk modulus of solid phase

K_h : Bulk modulus of hydrate

K_f : Bulk modulus of fluid (brine)

$\overline{K}_f$: New bulk modulus of the pore fluid mixture.

K_{HM}: Effective bulk modulus

K_{dry}: Bulk modulus of dry frame

K_{sat}: Bulk modulus of saturated sediments

G_S: Shear modulus of solid phase

G_{HM} : Effective shear modulus

G_{dry} : Shear modulus of dry frame

G_{sat} : Shear modulus of saturated sediments

S_N : Normal stiffness between two grains in contact

S_T : Tangential stiffness between two grains in contact

ν_s : Poisons ratio of solid phase

ν_{HM} : Effective poisons ratio

P: Hydrostatic confining stress

V_p : Compressional (P)-wave velocity

V_s : Shear (S)-wave velocity

M : Compressional modulus

Background

Pure gas hydrates have a P-wave velocity of about 3.27 km/s (Waite et al., 2000) The velocity of marine sediments within 300 m of water depth is generally accepted as 1.5 – 1.7 km/s. Presence of gas hydrates in marine sediments will therefore result in higher bulk P-wave velocity. However, unlike hydrocarbons that reside in the pore spaces of the sediments, hydrates can exist in at least three states (Helgerud *et al.*, 1999). It could be a) cement coat binding the grains (can also be modeled as hydrate being part of the mineral frame), b) non-cementing part of mineral frame which reduces porosity and affect on the solid phase elastic properties, and c) constituent of the pore fluid. These arrangements are illustrated in Figure 14.

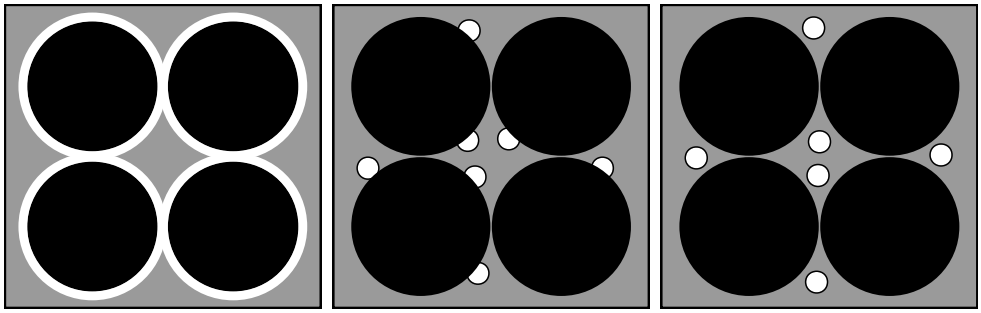

Figure 14: Three possible arrangement of methane hydrate in pore space (after Dvorkin *et al.*, 2003). The mineral grains are black; brine is gray; and hydrate is white.

In cases a) and b) hydrate is attached to the grains and therefore considered as mineral frame. The total porosity changes with the saturation, S_h, as:

$$\bar{\phi} = \phi_t - C_h = \phi_t (1 - S_h).$$

In case c) hydrate is not connected to grains and therefore considered as part of the pore fluid mainly affecting on the pore fluid elastic properties. The total porosity of the solid frame does not change with respect to S_h and therefore remains the same.

$$\bar{\phi} = \phi_t$$

However, the bulk modulus $\left(\overline{K_f}\right)$of pore fluid changes as the harmonic average of hydrate (K_h) and fluid (K_f):

$$\overline{K}_f = \left[S_h / K_h + (1 - S_h) / K_f\right]^{-1},$$

Since the matrix remains unaffected, the shear modulus of the sediment remains unchanged but the bulk density ($\overline{\rho}_f$) changes as the arithmetic average of hydrate (ρ_h) and fluid (ρ_f):

$$\overline{\rho}_f = S_h \rho_h + (1 - S_h)\rho_f .$$

This implies that morphology of grain to grain contact through hydrate cementing impacts the elastic moduli differently than grain to grain contact with hydrate in suspension. Thus, the same rock type with same porosity and identical mineralogy may be much stiffer in cemented case than those with no cement (Dvorkin *et al.*, 2003).

Helgerud et al. (1999) developed a method for modeling different hydrate arrangements in marine sediments known as “Effective Medium Modeling (EMM);” it is the method of choice in this applications. EMM is performed in two steps. First, elastic moduli of the dry sediment frame are estimated and second, the fluid is placed in the frame to compute the bulk elastic moduli of the system. The two steps are explained below:

1) Building dry frame:

First, Bulk (K) and shear (G) modulus and density of solid phase are calculated using Hill's (1952) average and mass balance equations:

$$K_s = 0.5 \cdot [\sum_{i=1}^{m} f_i K_i + (\sum_{i=1}^{m} f_i / K_i)^{-1}],$$

$$G_s = 0.5 \cdot [\sum_{i=1}^{m} f_i G_i + (\sum_{i=1}^{m} f_i / G_i)^{-1}],$$

$$\rho_s = \sum_{i=1}^{m} f_i \rho_i,$$

Where m is the number of the mineral components. f_i is fraction of i^{th} component in the mineral frame. K_i, G_i & ρ_i are the bulk, shear modulus and density of i^{th} component respectively.

Then, effective bulk (K_{HM}) and shear (G_{HM}) modulus are calculated to account for the effective pressure, porosity and mineralogy of the sediment. For this purpose, S_N and S_T; the normal and tangential stiffnesses between two grains in contact respectively, are calculated.

$$S_N = \frac{4aG_s}{1-\nu_s}, \quad S_T = f\frac{8aG_s}{2-\nu_s}.$$

Where a is the radius of the circular contact area between the spheres and G_s and ν_s are the shear modulus and Poisson's ratio of the material of the grains, respectively. f is a frictionless coefficient used to indicate grain contact type. It varies between 0 and 1. For instance, for 100% cement contact case (frictionless contact) f=0. As cement contacts decreases, f increases to maximum value of 1 indicating hydrates are in pore-filling mode (perfect adhesion).

$$K_{HM} = \frac{n(1-\phi_c)}{12\pi R} S_N, \quad G_{HM} = \frac{n(1-\phi_c)}{20\pi R}(S_N + \frac{3}{2}S_T),$$

Substitution S_N and S_T in effective moduli equation results the following:

$$K_{HM} = \left[\frac{n^2(1-\phi_c)^2 G_s^2}{18\pi^2(1-\nu_s)^2} P\right]^{\frac{1}{3}},$$

$$G_{HM} = \frac{2+3f-\nu_s(1+3f)}{5(2-\nu_s)}\left[\frac{3n^2(1-\phi_c)^2 G_s^2}{2\pi^2(1-\nu_s)^2} P\right]^{\frac{1}{3}},$$

$$\nu_{HM} = \frac{2-2f+\nu_s(2f-1)}{2[4+f-\nu_s(2+f)]}.$$

Where ϕ_c is critical porosity (limit of the porosity at which the mineral grains can be viewed as being in suspension) which is estimated to be 0.35 to 0.4 for clastics (Nur *et al.*,1998), n is the coordination number (the average number of contacts per grain) which is estimated by Dvorkin and Nur (1996) to be about 6 at critical porosity, R is the average radius of the grain, and S_N and S_T are the normal and tangential stiffnesses between two grains in contact respectively. P is hydrostatic confining stress.

In case of grains that are in perfect contact (frictionless spheres):

$$S_N = \frac{4aG_S}{1-\upsilon_s}\ ,\ \ S_T = 0$$

$$K_{HM} = \left[\frac{n^2(1-\phi_c)^2 G_S^2}{18\pi^2(1-\upsilon_S)^2} P\right]^{\frac{1}{3}},\ G_{HM} = \frac{1}{5}\left[\frac{3n^2(1-\phi_c)^2 G_S^2}{2\pi^2(1-\upsilon_S)^2} P\right]^{\frac{1}{3}}$$

$$\nu_{HM} = \frac{1}{2}\frac{(V_p/V_s)^2-2}{(V_p/V_s)^2-1} = \frac{1}{2}\left(1-\frac{3}{3K_{HM}/G_{HM}+1}\right) = 0.25.$$

The effective poisons ratio is constant and does not depend on the material of grains.

In case of grains that are in least contact (perfect adhesion; Mindlin, 1949):

$$S_N = \frac{4aG_s}{1-\nu_s}, S_T = \frac{8aG_s}{2-\nu_s},$$

$$K_{HM} = \left[\frac{n^2(1-\phi_c)^2 G_s^2}{18\pi^2(1-\nu_s)^2} P\right]^{\frac{1}{3}},\ \ G_{HM} = \frac{5-4\nu_s}{5(2-\nu_s)}\left[\frac{3n^2(1-\phi_c)^2 G_s^2}{2\pi^2(1-\nu_s)^2} P\right]^{\frac{1}{3}}.$$

$$\upsilon_{HM} = \frac{\upsilon_S}{2(5-3\upsilon_S)}$$

In case a combined situation comprising cemented and uncemented contacts between grains, original equations are used with a fractionaless coefficient f :

$$S_N = \frac{4aG_s}{1-\nu_s}, \quad S_T = f\,\frac{8aG_s}{2-\nu_s}.$$

For porosity reduction effects on elastic moduli the two porosity states - critical porosity and porosity after hydrates inclusion – are connected using a rock model of choice for hydrates (pore filling, etc.). Three basic rock models can be envisioned (Dvorkin and Nur, 1996):

a) Stiff rock model: It is suited when hydrates are modeled as cement. This model adds hydrates as additional material within original grains affecting on grain to grain contact. This increases the elastic moduli and velocity rapidly even with small reduction in porosity as shown in Figure 15. This model implement the upper Hashin-Shtrikman bound.

$$K_{Dry} = \left[\frac{\phi/\phi_c}{K_{HM} + \frac{4}{3}G_s} + \frac{1-\phi/\phi_c}{K_s + \frac{4}{3}G_s}\right]^{-1} - \frac{4}{3}G_s,$$

$$G_{Dry} = \left[\frac{\phi/\phi_c}{G_{HM} + Z} + \frac{1-\phi/\phi_c}{G_s + Z}\right]^{-1} - Z,$$

$$Z = \frac{G_s}{6}\left(\frac{9K_s + 8G_s}{K_s + 2G_s}\right).$$

b) Soft rock model: This model is suited for un-cemented hydrates in pore-filling mode. This model assumes small particles of hydrates fill pore spaces reducing the total porosity. In this case increment in velocity is relatively modest (Figure 4). This model applies the lower Hashin-Shtrikman bound to indicate elastic moduli versus porosity reduction.

$$K_{Dry} = \left[\frac{\phi/\phi_c}{K_{HM} + \frac{4}{3}G_{HM}} + \frac{1-\phi/\phi_c}{K_s + \frac{4}{3}G_{HM}}\right]^{-1} - \frac{4}{3}G_{HM},$$

$$G_{Dry} = \left[\frac{\phi/\phi_c}{G_{HM} + Z} + \frac{1-\phi/\phi_c}{G_s + Z}\right]^{-1} - Z,$$

$$Z = \frac{G_{HM}}{6}\left(\frac{9K_{HM} + 8G_{HM}}{K_{HM} + 2G_{HM}}\right).$$

c) Constant cement model: This model is suited for a hybrid case. This model is used for partially cemented grains with hydrate in pore-filling mode. This model uses lower Hashin –Shtrikman bound but the high porosity end-point lies on the cement model curve (figure4).

$$K_{Dry} = [\frac{\phi/\phi_c}{K_{HM} + \frac{4}{3}G_{HM}} + \frac{1-\phi/\phi_c}{K_s + \frac{4}{3}G_{HM}}]^{-1} - \frac{4}{3}G_{HM},$$

$$G_{Dry} = [\frac{\phi/\phi_c}{G_{HM} + Z} + \frac{1-\phi/\phi_c}{G_s + Z}]^{-1} - Z,$$

$$Z = \frac{G_{HM}}{6}\left(\frac{9K_{HM} + 8G_{HM}}{K_{HM} + 2G_{HM}}\right).$$

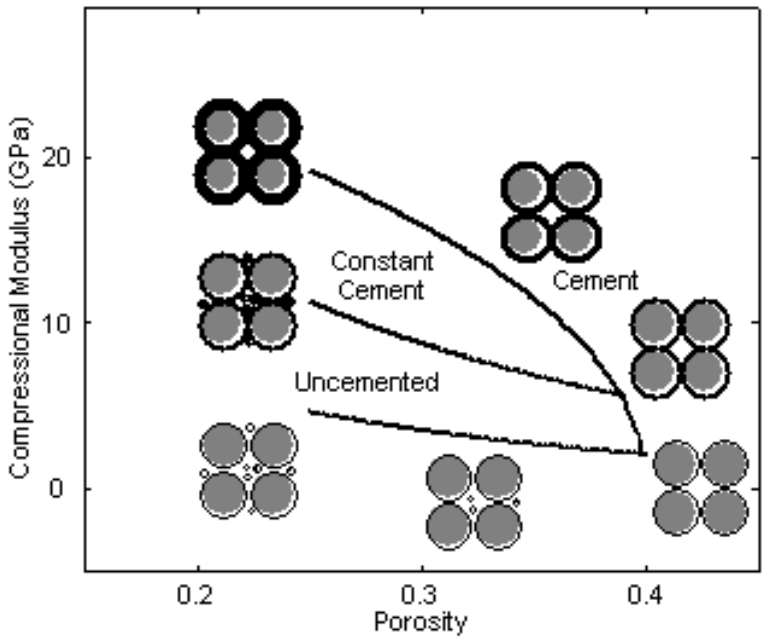

Figure 15: Compressional modulus versus porosity for three modes of porosity reduction (bold curves) for a dry pure-quartz porous system (after Dvorkin *et al.*, 2003).

2) Fluid emplacement

This step mainly comprises placing fluid in the dry frame to account for saturated sediments using Gassmann's (1951) equation for Bulk (K) and Shear (G) moduli and Mavko *et al.* (1998) equation for compressional (M) modulus:

$$K_{Sat} = K_s \frac{\phi K_{Dry} - (1+\phi)K_f K_{Dry}/K_s + K_f}{(1-\phi)K_f + \phi K_s - K_f K_{Dry}/K_s}, \quad G_{Sat} = G_{Dry},$$

$$M_{Sat} = M_s \frac{\phi M_{Dry} - (1+\phi)K_f M_{Dry}/M_s + K_f}{(1-\phi)K_f + \phi M_s - K_f M_{Dry}/M_s},$$

Finally, the elastic-wave velocities, V_p and V_s, can be computed using the elastic moduli (K, G and M) and density (ρ) as:

$$M = \rho V_p^2, \quad G = \rho V_s^2, \quad K = M - \tfrac{4}{3}G,$$

Where the bulk density can be defined as: $\rho_b = (1-\phi)\rho_s + \phi\rho_f$. In the current application only V_P is being modeled.

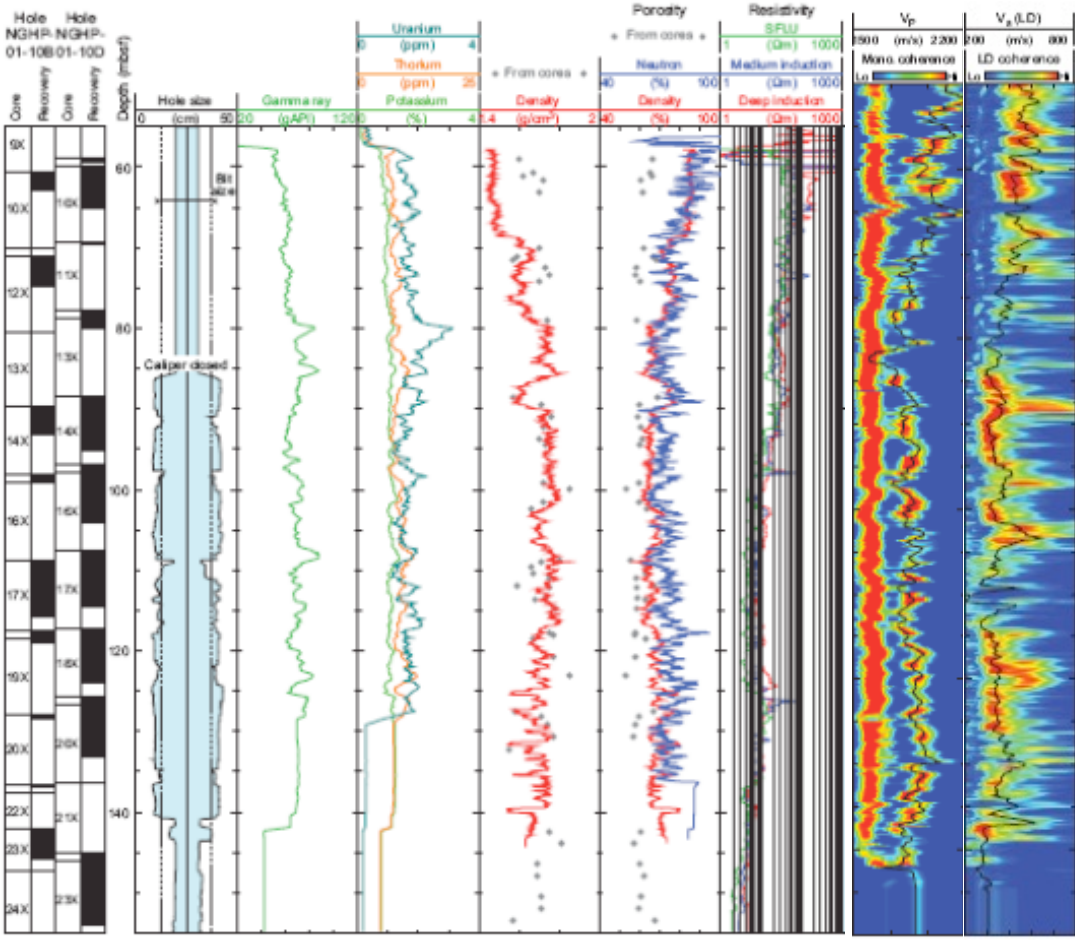

Figure 16. Log suite from well W (NGHP-01-10).

Hydrates in fracture

We have modeled faulted stratigraphy by introducing dimensionless cracks within a sediment matrix. In our approach geometry of fractures is not required. Rather, fracture density is important. The modulus-porosity relation of the faulted stratigraphy is predicted using the the Hashin Shtrikman bounds (Hashin and Shtrikman, 1963); the lower bound assumes fractures are disconnected and therefore in the foreground and the upper bound assumes that factures are interconnected and in the background.

We break down the system into three phases; the first two phases are shale (clay and quartz) as matrix and water as pore-filling fluid. The third phase is faults which are

completely filled with hydrates. Soft rock model is used to estimate the moduli of the two-phase component (shale filled with 100% water) and the third phase is tested with both upper and lower Hashin-Shtrikman bounds. The upper bound physically implies that the framework material is the stiffest material and the inclusions are filled with soft material. Since hydrates is the stiffest component we can apply the Upper Hashin-Shtrikman bound to indicate fractures in connected mode.

The lower Hashin-Shtrikman bound indicates the original framework material in the system is the softest material, whereas the inclusions are filled with stiff material. Shale saturated with water is the softest component in the system, therefore, we can use this bound to best estimate hydrates mode in non-connected fractures (isolated fractures).

We apply the models with data from Well 10D in the KG Basin (Figure 16). We show the effect of hydrates filled fractures and its style (connected vs. disconnected) on V_P and compare it with the familiar forms of hydrates states (hydrates in suspension, loadbearing case). Figure 17 shows schematic draw of four possible hydrates arrangement in macrostructure. Using rock physics model we were able to calculate the theoretical values of compressional velocity as hydrates been added to the system for different arrangements and the results are plotted in figure 18.

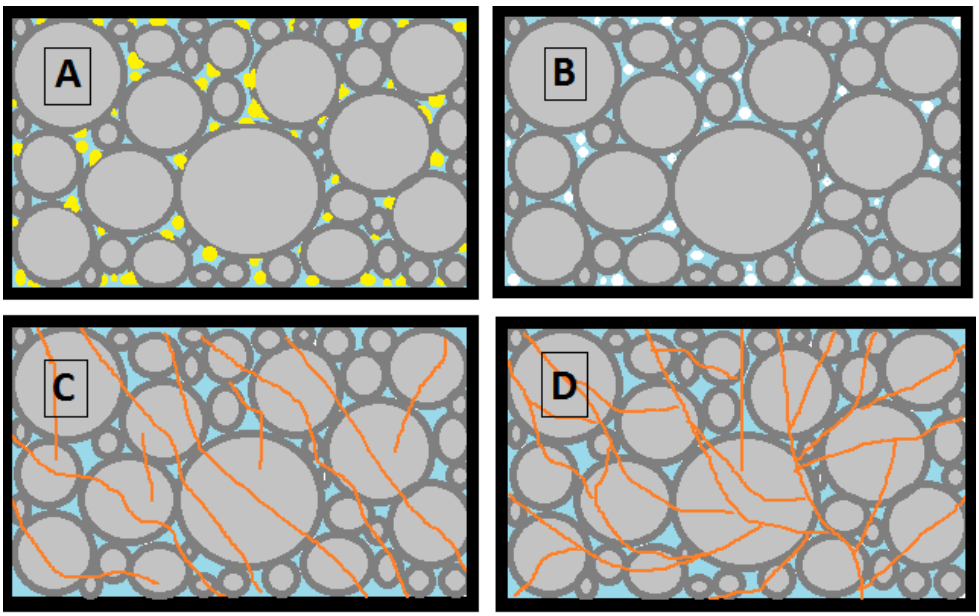

Figure 17: Schematics. (A) Hydrates in load-bearing state; (B) Hydrates in suspension with pore fluid; (C) Hydrates in non-connected fractures; and (D)Hydrates in interconnected fractures. The quartz grains are gray; brine is blue; and hydrate is yellow, white, brown in A, B and C, D respectively.

For modeling, parameters such as porosity and clay content is read from the logs (Figure 16) and used to estimate the elastic moduli and in turn ρ, V_P and V_S curves with different rock-physics models of hydrate. The most appropriate model will give the

closest match to the observed density, V_P and V_S. However, this approach will lead to quantification of hydrate at the well location only. The key question is can the rock physics model at well be extended regionally? Further, Well-10D core was observed to comprise fractured sediments. We are aware that none of the models discussed above fits fractures sediments. We therefore introduce a new parameter "connectivity index" to lead from one rock model to another.

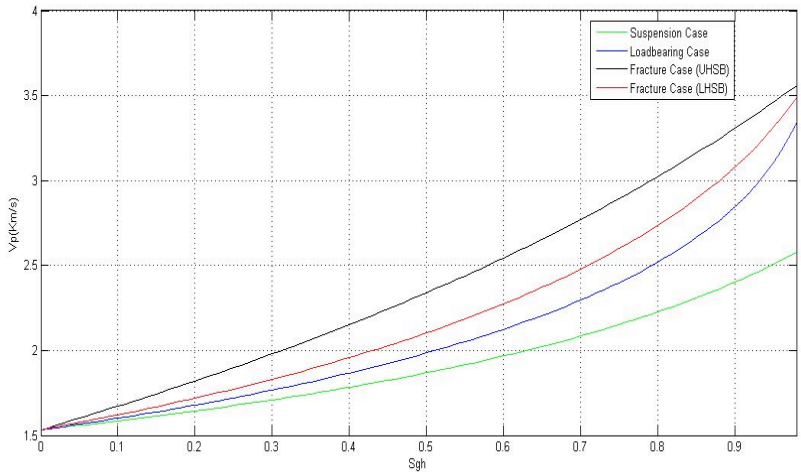

Figure 18: Theoretical values of velocities with respect to Hydrate saturation based on different rock physics models for KG Basin (porosity=0.65 and clay=80%). Curves coded with colors: (Green) outcome curve using soft rock model adjusted for Hydrates in suspension state; (Blue) outcome curve using soft rock model adjusted for Hydrates in loadbearing state; (Red) outcome curve using fracture model (Lower Hashin Shtrikman bound) for hydrates filling non-connected fractures; and (Black) outcome curve using fracture model (Upper Hashin Shtrikman bound) for hydrates filling interconnected fractures.

Introduction of Connectivity Index

The nature is more complex than what we determine theoretically and we cannot ignore the fact that the heterogeneity exists in subsurfaces , therefore we would expect that the fractures may exist in two schemes interchangeably. Therefore we introduce connectivity index to show that the system may vary in the fractions of connected fractures versus non-connected fractures (isolated). We calculate it as follow:

$$CI = A + \beta \times Sat$$

where CI , A , β and Sat are Connectivity Index, constant, change rate and saturation respectively. This is calculated using the following assumptions for our case:

We assume maximum connectivity for the system is 1 which is valid for 100% connected fructures. This is assumed to be at the lowest possible saturation resulted from Upper Hashin Shtrikman bound. We assume minimum connectivity for the system is 0 which is valid only for 0% connectivity fractures. This is assumed to be at the high possible saturation resulted from Lower Hashin Shtrikman bound.

Application and Results:

For application we assume the KG Basin to comprise unconsolidated clay rich sediments with total clay content of about 70-100% with 0-30% quartz saturated with brine. We assumed critical porosity of 50% and coordination number N of 6. The effective pressure is calculated to be 1.2 MPa. The predicted hydrate saturation for different hydrate schemes using different rock physics models is shown in figure 4 with respect to P-wave velocity and porosity logs. The elastic parameters of methane hydrates used in the modeling are as follow: the bulk modulus K= 7.7 GPa, G=3.2 GPa, Density=0.91 g/cc. Furthermore we visualize the concept of connectivity index with respect to hydrates filled in different style fractures. Average of connectivity might be taken as indicative parameter of fractures styles.

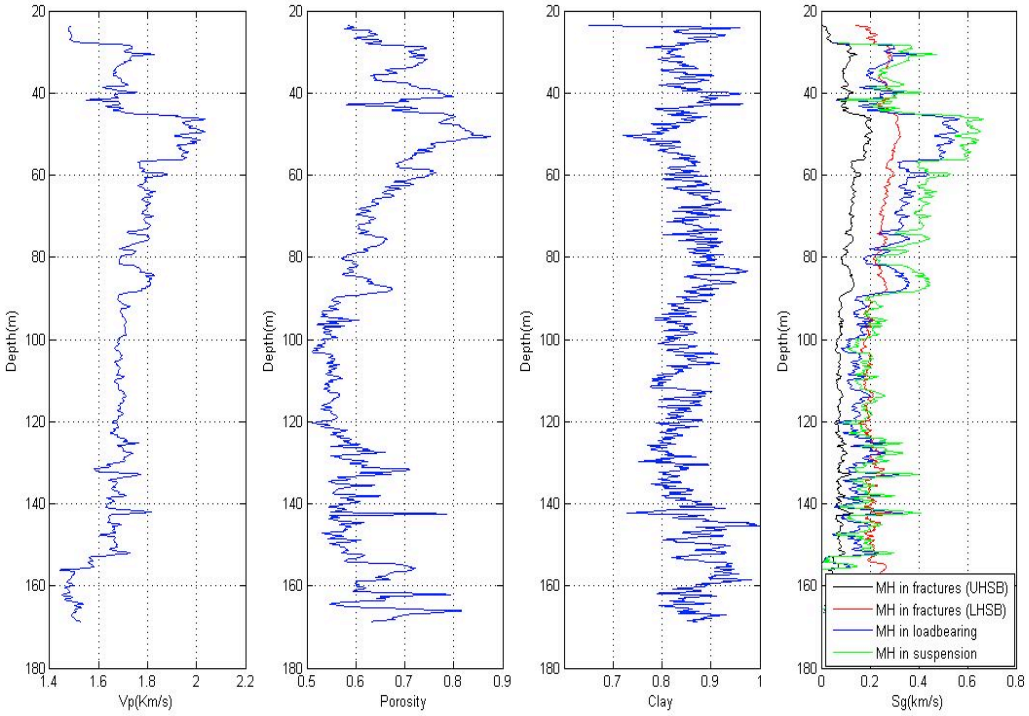

Figure 19: Results from Krishna-Godavari Basin offshore East Cost India. From left to Right: (A) compressional wave velocity (Km/s) with respect to depth (m); (B) Porosity with respect to depth (m);(C) Clay content with respect to depth (D) Hydrate saturation with respect to depth(m) using different rock physics models: (green) soft rock model adjusted for suspension state.(Blue) soft rock model adjusted for loadbearing state.

(Red) non-connected Fracture model using Lower Hashin Shtrikman Bound. (Black) inter-connected fracture model using Upper Hashin Shtrikman Bound.

Conclusions

In this DOE funded project we have developed two new concepts: a) application of traveltime and waveform tomography with early arrivals (near seafloor reflection) to image velocity and attenuation contrasts in the shallow marine sediments; b) development of a hydrate-saturated fracture theory; and c) introduction of *connectivity index* to simulate the transformation of geology from one rock physics model to another.

V_P estimate of hydrate-bearing sediments can be objectively obtained using unified imaging (UI) which develops a structurally consistent velocity model and depth image by cyclic implementation of traveltime inversion and depth migration; the structural consistency in this paper is measured using a set of reflectors within and outside the gas hydrate stability zone. UI is kept objective by not including the BSR in the traveltime inversion. In three cycles, UI improves the spatial resolution of a simple starting V_P model, Vel0, estimated by SVA. The final depth image, Image3, suggests that syn-tectonic sedimentation suppresses seafloor failure in the NW part of the seismic profile maintaining a sub-horizontal seafloor and creating a continuous BSR. Lack of sedimentation in the SE part along with the tectonic uplift creates rugged seafloor topography. Two dominant sets of faults and their conjugate can be identified along the line. An otherwise continuous BSR becomes patchy in fault dominated sediments most likely due to focused fluid flow from the deeper subsurface which perturbs the thermodynamic conditions locally. Even in the presence of a patchy BSR, elevated (>1.7 km/s) velocities in Vel3 allow first-order hydrate detection suggesting that V_P is a better hydrate proxy than BSR amplitudes in faulted sediments.

FWI yields reliable estimates of sediment V_P and attenuation even in acoustic approximation to elastic data most likely due to the narrow aperture of the seismic survey which restricts mode conversion. Success of FWI depends both on the starting model as well as data preconditioning; only the amount of coda that can be predicted by the starting model should be included in FWI discounting for effects of non-physical factors on amplitudes that are beyond the physics of modeling. The reliability of evolving V_P and attenuation perturbations, similarity of the real and simulated data, and the objective function convergence serve as stopping criteria. In general, PSDM images geological features in higher resolution than FWI, but FWI provides complementary information on physical properties of sediment properties. Thus, although both FWI models and PSDM images that are directly interpretable, a composite of the two appear to be optimal for interpretation in the KG Basin.

A combination of V_P model and the reflectivity images suggests that hydrates may exist in both pore-filling and gain-cementing state along the seismic profile. A combination of attenuation model and fault structures (interpreted on the reflectivity image) suggests that faults enhance attenuation. A combination of V_P and attenuation models suggest that while free gas enhances attenuation and hydrates can increases or decreases

attenuation depending on their state. Rock physics modeling developed for fractured sediments reasonably reflects hydrate saturation observed in the NGHP-01-10 Well.

References

Bhatnagar, G., W.G., Chapman, G.R., Dickens, B., Dugan, and G.J., Hirasaki (2007), Generalization of gas hydrate distribution and saturation in marine sediments by scaling of thermodynamic and transport processes, *American Journal of Science, 307(6)*, 861-900, doi:10.2475/06.2007.01.

Carroll J. J., Mather A. E., (1992), The System Carbon Dioxide-Water and the Krichevsky-Kasarnovsky Equation. *J. of Solution Chemistry*, 21(7), 606-621.

Chatterjee S., G.R., Dickens, G., Bhatnagar, W.G., Chapman, B., Dugan, G.T., Snyder and G.J., Hirasaki (2011), Pore water sulfate, alkalinity and carbon isotope profiles in shallow sediment above marine gas hydrate systems: A numerical modeling perspective*, Journal of Geophysical Research - Solid Earth, 116, B09103*, doi: 10.1029/2011JB008290.

Civan, F. C. (2002a). Relating Permeability to Pore Connectivity Using a Power-law Flow Unit Equation. *Petrophysics*, 43 (6), 457-476.

Clarke, M., and Bishnoi, P. R. (2001). Determination of the activation energy and intrinsic rate constant of methane gas hydrate decomposition. *The Canadian J. of Chem. Eng.*, 79, 143-147.

Clarke, M., and Bishnoi, P. R. (2004). Determination of the activation energy and intrinsic rate constant of CO2 gas hydrate decomposition using in-situ particle size analysis. *Chem. Eng Sci.*, 59, 2983-2993

Collett, T., Riedel, M., Cochran, J., Boswell, R., Presley, J., Kumar, P., Sathe, A., Sethi, A., Lall, M.V., Sibal, V., 2006. Expedition 01 Initial Reports, Indian National Gas Hydrate Program.

Delescluse, M., Nedimovic, M.R., Louden, K.E., 2011. 2D waveform tomography applied to long-streamer MCS data from the Scotian Slope. *Geophys,* 76, B151-B163.

Daigle, H., Dugan, B., (2009), Extending NMR data for permeability estimation in fine-grained sediments. *Marine and Petroleum Geology*, 26(8), 1419-1427, doi:10.1016/j.marpetgeo.2009.02.008.

Davie, M.K. and B.A. Buffett (2001), A numerical model for the formation of gas hydrate below the seafloor, *J. Geophys. Res*., *106*, 497-514. Davie, M. K., and B. A. Buffett (2003a), Sources of methane for marine gas hydrate: Inferences from a

comparison of observations and numerical models, Earth Planet. Sci. Lett., 206, 51-63, doi:10.1016/S0012-821X(02)01064-6.

Davie, M.K., and B.A. Buffett (2003), Sources of methane for marine gas hydrate: Inferences from a comparison of observations and numerical models, Earth Planet. Sci. Lett., 206, 51-63, doi:10.1016/S0012-821X(02)01064-6.

Dickens, G. R., and G. T. Snyder (2009), Interpreting upward methane flux, *Fire in the Ice, Winter,* 7-10.

Dix, C. H. (1955), Seismic velocities from surface measurements., *Geophys*, 20, 68 - 86.

Dvorkin, J., and Nur, A., (1996), Elasticity of high-porosity sandstones: Theory for two north-sea datasets.

Dvorkin, J., Nur, A., Uden, R., and Taner, T., (2003), Rock physics of gas hydrate reservoir, *The Leading Edge*.

Dvorkin, J., (2010), Seismic reflections of gas hydrates: a rock physics tutorial.

Egeberg, P.K., and G.R. Dickens (1999), Thermodynamic and pore water halogen constraints on gas hydrate distribution at ODP Site 997 (Blake Ridge), Chem. Geol., 153, 53-79, doi:10.1016/S0009-2541(98)00152-1.

Englezos, P., Kalogerakis, N., Dholabhai, P. D., and. Bishnoi, P. R. (1987a). Kinetics of Formation of Methane and Ethane Gas Hydrates, *Chem. Eng. Sci.* 42, 2647-2658.

Fong, W. S., Sandler, S. I., Emanuel, A. S. (1993). A Simple Predictive Calculation for the Viscosity of Liquid Phase Reservoir Fluids with High Accuracy for CO2 Mixtures, SPE 26645, Proceedings of SPE ATCE, Houston, 3-6 Oct.

G. Gu, G. R. Dickens, G. Bhatnagar, F. S. Colwell, G. J. Hirasaki, W. G. Chapman, Abundant Early Palaeogene marine gas hydrates despite warm deep ocean temperatures, *Nature Geoscience*, 4, 848–851 (2011), doi:10.1038/ngeo1301.

Hole, J. A., and B. C. Zelt (1995), 3D finite-difference reflection traveltimes, *Geophys. J. Intl*. 121, 427-434

Hashin, Z., Shtrikman, S., (1963), A variational approach to the theory of the elastic behaviour of multiphase materials. *J. Mech. Phys. Sol*., 11, 127-140.

Helgerud, M., Dvorkin, J., Nur, A., Sakai, A., and Collett, T., (1999), Elastic-wave velocity in marine sediments with gas hydrates: Effective medium modeling.

Hill, R., (1952), The elastic behavior of crystalline aggregate, *Proc. Physical Soc*., London, A65, 349-354.

Jaiswal, P., and C. A. Zelt (2008), Unified imaging of multichannel seismic data: combining traveltime inversion and pre-stack depth migration, *Geophys.*, 73, doi: 10.1190/1.2957761.

Jo, C.-H., C. Shin, and J. H. Suh (1996), An optimal 9-point, finite-difference, frequency-space, 2-D scalar wave extrapolator, *Geophys.*, 61(2), 529-537.

Kastner, M., M. E. Torres, E. Solomon, and A. J. Spivack (2008), Marine pore fluid profiles of dissolved sulfate: Do they reflect *in situ* methane fluxes?, *Fire in the Ice, Summer*, 6–8.

Kim, H.C., Bishnoi, P. R., Heidemann, R. A. and Rizvi, S. S. H. (1987). Kinetics of Methane Hydrate Dissociation, *Chem. Eng. Sci.*, 42 (7), 1645-1653.

Lake, L. W. (1989). Enhanced Oil Recovery. Prentice-Hall Inc. Upper Saddle River, NJ.

Liu, X. and P.B. Flemings (2006), Passing gas through the hydrate stability zone at southern Hydrate Ridge, offshore Oregon*, Earth Planet. Sci. Lett*., *67*:3403-3421.

Liu, X. and P.B. Flemings (2007), Dynamic multiphase flow model of hydrate formation in marine sediments. *J. Geophys. Res., 112*, B03101, doi:10.1029/2005JB004227.

Malegaonkar, M. B., Dholabhai, P. D., and. Bishnoi, P. R. (1997). Kinetics of Carbon Dioxide and Methane Hydrate Formation, *Canadian J. Chem. Eng.*, 75, 1090-1099.

Marfurt, K. J., and C. S. Shin (1989), The future of iterative modeling of geophysical exploration, Livrenoir, Brooklyn, NY.

Mavko, G., T. Mukerji, J. Dvorkin, (1998), The Rock Physics Handbook: Tools for Seismic Analysis in Porous Media, Cambridge University Press, New York, 329.

Milkov, A. V., G.R., Dickens, G.E., Claypool, Y.J., Lee, W.S., Borowski, M.E., Torres, W., Xu, H., Tomaru, A.M., Tréhu and P., Schultheiss (2004), Co-existence of gas hydrate, free gas, and brine within the regional gas hydrate stability zone at Hydrate Ridge (Oregon margin): evidence from prolonged degassing of a pressurized core, *Earth Planet. Sci. Lett.*, *222*, 829–843.

Mindlin, R. D., (1949), Compliance of elastic bodies in contact, Trans.SDME,71, A-259.

Moridis, G.J. (2003), Numerical Studies of Gas Production from Methane Hydrates, *SPE J.*, 8(4), 359-370.

Nur, A., Mavko, G., Dvorkin,J., Galmudi,D., (1998), Critical porosity: A key to Relating Physical Properties to porosity in Rocks, *The Leading Edge*.

Phirani, J., Hirasaki, G. J., Mohanty, K. K. (2009a), Warm Water Flooding of Unconfined Gas Hydrate Reservoirs, *Energy and Fuels,* 23 (9), 4507-4514.

Phirani, J., Mohanty, K. K., (2009). Warm Water Flooding of Confined Gas Hydrate Reservoirs, *Chem. Eng. Sci.,* 64 (10), 2361-2369.

Pratt, R. G. (1999), Seismic waveform inversion in the frequency domain, Part 1: Theory and verification in a physical scale model, *Geophys*., 64(3), 888-901

Press, W. H., S. A. Teukolsky, W. T. Vetterling, and B. P. Flannery (1992), Numerical Recipes in C : the art of scientific computing, 2nd ed., Univ. Press.

Petersen, C. J., C. Papenberg, and D. Klaeschen, (2007), Local seismic quantification of gas hydrates and BSR characterization from multi-frequency OBS data at northern Hydrate Ridge: *Earth Planet. Sci. Lett.*, 255, 414-431, doi: 10.1016/j.epsl.2007.01.002.

Riedel, M., T. S. Collett, P. Kumar, et al., (2010), Seismic imaging of a fractured gas hydrate system in the Krishna-Godavari Basin offshore India: *Mar. Petr. Geol.*, 27, 1476-1493, doi: 10.1016/j.marpetgeo.2010.06.002.

Riedel, M., T. S. Collett, and U. Shankar, (2011), Documenting channel features associated with gas hydrates in the Krishna-Godavari Basin, offshore India: *Mar. Geol.*, 279, 1-11, doi: 10.1016/j.margeo.2010.10.008.

Scales, J. A., P. Docherty, and A. Gersztenkorn (1990), Regularization of nonlinear inverse problems-imaging the near-surface weathering layer, *Inverse Problems*, 6, 115-131.

Sirgue, L., and R. G. Pratt (2004), Efficient waveform inversion and imaging: A strategy for selecting temporal frequencies, *Geophys.*, 69(1), 231-248.

Sloan, E.D. (1998), Clathrate Hydrates of Natural Gases. 2nd edition, Marcel Dekker Inc., New York.

Snyder, G. T., A. Hiruta, R. Matsumoto, G. R. Dickens, H. Tomaru, R. Takeuchi, J. Komatsubara, Y. Ishida, and H. Yu (2007), Pore water profiles and authigenic mineralization in shallow marine sediments above the methane-charged system on Umitaka Spur, Japan Sea, *Deep-Sea Res. II*, *54*, 1216-1239, 10.1016/j.dsr2.2007.04.001.

Sun, X. and Mohanty, K. K. (2006). Kinetic Simulation of Methane Hydrate Formation and Dissociation in Porous Media. *Chem. Eng. Sci*., 61, 3476-3495.

Vidale, J. (1988), Finite-difference travel time calculation, *Bull. Seism. Soc. Am.,* 78(8), 2062-2076.

Waite, W. F., M. B. Helgerud, A. Nur, et al., (2000), Laboratory measurements of compressional and shear wave speeds through methane hydrate: Gas Hydrates: *Challenges for the Future*, 912, 1003-1010.

Westbrook, G. K., S. Chand, G. Rossi, et al., (2008), Estimation of gas hydrate concentration from multi-component seismic data at sites on the continental margins of NW Svalbard and the Storegga region of Norway: *Mar. Petr. Geol.*, 25, 744-758, doi: 10.1016/j.marpetgeo.2008.02.003.

Wu, R.-S., and M. N. Toksoz (1987), Diffraction tomography and multisource holography applied to seismic imaging, *Geophys*., 52(1), 11-25.

Zatsepina, O.Y., and B.A., Buffett (1998), Thermodynamic conditions for the stability of gas hydrate in the seafloor. *J. Geophys. Res., 103*, 24127-24139.

Zelt, C. A. (1999), Modeling strategies and model assessment for wide-angle seismic travel time data, *Geophys. J. Intl*., 139(1), 183-204.

Zelt, C. A., R. M. Ellis, and B. C. Zelt (2006), Three-dimensional structure across the Tintina strike-slip fault, northern Canadian Cordillera, from seismic refraction and reflection tomography, *Geophys. J. Intl.,* 167(3), 1292-1308, 10.1111/j.1365-246X.2006.03090.x.

Publications

Task 5: Carbon Inputs and Outputs to Gas Hydrate Systems

Dickens, G. R., and G. T. Snyder (2009), Interpreting upward methane flux, *Fire in the Ice, Winter,* 7-10.

Dickens, G. R. (2011), Down the Rabbit Hole: toward appropriate discussion of methane release from gas hydrate systems during the Paleocene-Eocene thermal maximum and other past hyperthermal events, *Clim. Past, 7*, 831-846, doi:10.5194/cp-7-831-2011.

G. Gu, G. R. Dickens, G. Bhatnagar, F. S. Colwell, G. J. Hirasaki, W. G. Chapman, Abundant Early Palaeogene marine gas hydrates despite warm deep ocean temperatures, *Nature Geoscience*, 4, 848–851 (2011), doi:10.1038/ngeo1301. Highlighted by *Nature Asia-Pacific*.

Snyder, G. T., A. Hiruta, R. Matsumoto, G. R. Dickens, H. Tomaru, R. Takeuchi, J. Komatsubara, Y. Ishida, and H. Yu (2007), Pore water profiles and authigenic mineralization in shallow marine sediments above the methane-charged system on Umitaka Spur, Japan Sea, *Deep-Sea Res. II*, *54*, 1216-1239, 10.1016/j.dsr2.2007.04.001.

Task 6: Numerical Models for Quantification of Hydrate and Free Gas Accumulations

Bhatnagar, G., W.G., Chapman, G.R., Dickens, B., Dugan and G.J., Hirasaki (2006), Scaling of thermodynamic and transport processes for predicting methane hydrate saturation in marine sediments worldwide, *Society of Petroleum Engineers (SPE) Annual Technical Conference and Exhibition, 24-27 September 2006, San Antonio, Texas, USA*, SPE 106519-STU, 10.2118/106519-STU.

Bhatnagar, G., W.G., Chapman, G.R., Dickens, B., Dugan, and G.J., Hirasaki (2007), Generalization of gas hydrate distribution and saturation in marine sediments by scaling of thermodynamic and transport processes, *American Journal of Science, 307(6)*, 861-900, doi:10.2475/06.2007.01.

Bhatnagar, G., W.G., Chapman, G.J., Hirasaki, G.R., Dickens and B., Dugan (2008), Effect of overpressure on gas hydrate distribution, *Proceedings of the 6th International Conference on Gas Hydrates (ICGH 2008), Vancouver, British Columbia, Canada,* July 6-10, 2008.

Bhatnagar, G., W.G., Chapman, G.J., Hirasaki, G.R., Dickens and B., Dugan (2008), Relating gas hydrate saturation to depth of sulfate-methane transition, *Proceedings of the 6th International Conference on Gas Hydrates (ICGH 2008), Vancouver, British Columbia, Canada,* July 6-10, 2008.

Bhatnagar, G., W.G., Chapman, G.R., Dickens, B., Dugan and G.J., Hirasaki (2008), The sulfate-methane transition as a proxy for average methane hydrate saturation in marine sediments, *Geophysical Research Letters*, *35, L03611*, doi:10.1029/2007GL032500.

Bhatnagar G. (2008), Accumulation of gas hydrates in marine sediments, *Ph.D. dissertation*, Rice University.

Bhatnagar G., S., Chatterjee, W.G., Chapman, B., Dugan, G.R., Dickens and G.J., Hirasaki (2011), Analytical theory relating the depth of the sulfate-methane transition to gas hydrate distribution and saturation*, Geochemistry, Geophysics, Geosystems, 12, Q03003*, doi: 10.1029/2010GC003397.

Chatterjee S., G., Gu, G., Bhatnagar, W.G., Chapman, B., Dugan, G.R., Dickens and G.J., Hirasaki (2011), Effects of heterogeneous lithology and focused fluid flow on gas hydrate distribution in marine sediments, *Proceedings of the 7th International Conference on Gas Hydrates (ICGH 2011), Edinburgh, Scotland, United Kingdom*, July 17-21, 2011.

Chatterjee S., G.R., Dickens, G., Bhatnagar, W.G., Chapman, B., Dugan, G.T., Snyder and G.J., Hirasaki (2011), Pore water sulfate, alkalinity and carbon isotope profiles in shallow sediment above marine gas hydrate systems: A numerical modeling perspective*, Journal of Geophysical Research - Solid Earth, 116, B09103*, doi: 10.1029/2011JB008290.

Task 7: Analysis of Production Strategy

Phirani, J., Pitchumani, R., & Mohanty, K. K., "Transport Properties of Hydrate Bearing Formations from Pore-Scale Modeling," SPE 124882, Proceedings of SPE ATCE, New Orleans, LA, Oct. 4-7, 2009.

Phirani, J., Mohanty, K. K. & G. Hirasaki, "Warm Water Flooding of Unconfined Gas Hydrate Reservoirs," *Energy & Fuels* (2009), doi:10.1021/ef900291j.

Phirani, J., Hirasaki, G., & Mohanty, K. K., "Strategy for Gas Production from an Unconfined Marine Hydrate Reservoir," submitted to *JPSE* (2011).

Phirani, J. & Mohanty, K. K., "Warm Water Flooding of Confined Gas Hydrate Reservoirs," *Chem. Eng. Sci.*, 64, 2361-2369 (2009). doi:10.1016/j.ces.2009.02.019.

Task 8: Seafloor and Borehole Stability

Daigle, H., Bangs, N., Dugan, B., (2011), Transient hydraulic fracturing and gas release in methane hydrate settings: A case study from southern Hydrate Ridge, *Geochemistry, Geophysics, Geosystems*, doi:10.1029/2011GC003841.

Daigle, H., Dugan, B., (2011), Permeability anisotropy and fabric development: A mechanistic explanation. *Water Resources Research*, 47, W12517, doi:10.1029/2011WR011110.

Daigle, H., Bangs, N., Dugan, B., (2011), Transient pressures, hydraulic fracturing, and gas migration at southern Hydrate Ridge: geophysical observations and flow modeling, *Proc. 7th International Conf. Gas Hydrates*, 17-21 July 2011, Edinburgh, Scotland.

Daigle, H., Dugan, B., (2011), An improved technique for computing permeability from NMR measurements in mudstones, *Journal of Geophysical Research*, 116, B08101, doi:10.1029/2011JB008353

Daigle, H., Dugan, B., (2011), Capillary controls on methane hydrate distribution and fracturing in advective systems. *Geochemistry, Geophysics, Geosystems*, 12, Q01003, doi:10.1029/2010GC003392.

Daigle, H., Dugan, B., (2010), Origin and evolution of fracture-hosted methane hydrate deposits. *Journal of Geophysical Research*, 115, B11103, doi:10.1029/2010JB007492.

Daigle, H., Dugan, B., (2010), Effects of multiphase methane supply on hydrate accumulation and fracture generation. *Geophysical Research Letters*, 37, L20301, doi:10.1029/2010GL044970.

Daigle, H., Dugan, B., (2009), Extending NMR data for permeability estimation in fine-grained sediments. *Marine and Petroleum Geology*, 26(8), 1419-1427, doi:10.1016/j.marpetgeo.2009.02.008.

Dugan, B., Sheahan, T.C., in review, Offshore Sediment Overpressures: Mechanisms, Measurement and Models, *Reviews of Geophysics*, 2011RG000379.

Dugan, B., (2012), A Review of Overpressure, Flow Focusing, and Slope Failure, in Yamada et al. (eds.), *Submarine Mass Movements and Their Consequences*: *Advances in Natural and Technological Hazards Research*, 31, doi:10.1007/978-94-007-2162-3_24, Springer Science+Business Media, 267-276.

Dugan, B., Sheahan, T.C., Thibault, J., Evans, T., (2011), Offshore Sediment Overpressures: Overview of Mechanisms, Measurement and Modeling, in Gourvenec, S., White, D. (eds), *Frontiers in Offshore Geotechnics II*, Taylor & Francis Group, London, 271-276.

Dugan, B., (2008), Fluid Flow in the Keathley Canyon 151 Mini-Basin, Northern Gulf of Mexico, *Marine and Petroleum Geology*, 25, 919-923, doi:10.1016/j.marpetgeo.2007.12.005.

Hustoft, S., Dugan, B., Mienert, J., (2009), Effects of rapid sedimentation on developing the Nyegga pockmark-field; Constraints from hydrological modeling and 3-D

seismic data, offshore mid-Norway, *Geochemistry, Geophysics, Geosystems*, 10(6), Q06012, doi:10.1029/2009GC002409.

Hutchinson, D.R., Hart, P.E., Ruppel, C.D., Snyder, F., Dugan, B., (2009), Seismic and thermal characterization of a bottom-simulating reflection in the northern Gulf of Mexico, in Collett, T., Johnson, A., Knapp, C., Boswell, R. (eds), *Natural gas hydrates – energy resource potential and associated geologic hazards*, AAPG Memoir, 89, 266-286, doi:10.1306/13201105M893343.

Jones, E., Latham, T., McConnell, D., Frye, M., Hunt Jr., J., Shedd, W., Shelander, D., Boswell, R., Rose, K., Ruppel, C., Hutchinson, D., Collett, T., Dugan, B., Wood, W., (2008), Scientific Objectives of the Gulf of Mexico Gas Hydrate JIP Leg II Drilling, Paper OTC 19501, *Proceedings 2009 Offshore Technology Conference*, Houston TX, 5-8 May 2008.

Scholz, N.A., Riedel, M., Spence, G.D., Hyndman, R.D., James, T., Naegeli, K., Dugan, B., Pohlman, J., Hamilton, T., (2011), Do dissociating gas hydrates play a role in triggering submarine slope failures? A case study from the northern Cascadia margin, *Proc. 7th International Conf. Gas Hydrates*, 17-21 July 2011, Edinburgh, Scotland.

Waite, W.F, Santamarina, C., Cortes, D., Dugan, B., Espinoza, N., Germaine, J., Jang, J., Jung, J., Kneafsey, T., Shin, H., Soga, K., Winters, W., Yun, T-S., (2009), Physical properties of hydrate-bearing sediments, *Reviews of Geophysics*, 47, RG4003, doi:10.1029/2008RG000279.

Winters, W.J., Dugan, B., Collett, T.S., (2008), Physical Properties of Sediments from Keathley Canyon and Atwater Valley, JIP Gulf of Mexico Gas Hydrate Drilling Program, *Marine and Petroleum Geology*, 25, 896-905, doi:10.1016/j.marpetgeo.2008.01.018.

Manuscripts in preparation

Task 6: Numerical Models for Quantification of Hydrate and Free Gas Accumulations

Chatterjee S., G.R., Dickens, G., Bhatnagar, W.G., Chapman, B., Dugan, G.T., Snyder and G.J., Hirasaki, Modeling pore water profiles of marine gas hydrate systems: the extreme case OF ODP Site 685/1230, Peru Trench, *to be submitted to Geochimica Cosmochimica Acta by May 2012*.

Chatterjee S., et al., Lithologic heterogeneity, salinity and localized fluid flow governing localized gas hydrate distribution in marine sediments, *to be submitted to Geochemistry, Geophysics, Geosystems by May 2012*.

Gu G., P., Jaiswal, W.G., Chapman, C., Zelt and G.J., Hirasaki, Role of Multiple Gas Components on Hydrate/Free Gas Distribution and BSR, to be submitted.

Presentations

Task 6: Numerical Models for Quantification of Hydrate and Free Gas Accumulations

Bhatnagar G., G.J., Hirasaki, W.G., Chapman, B., Dugan and G.R., Dickens, Scaling of thermodynamic and transport processes for predicting gas hydrate distribution in marine sediments, *Annual General Meeting - Asia Oceania Geosciences Society, Singapore*, 2006 (oral presentation).

Bhatnagar G., G.J., Hirasaki, W.G., Chapman, B., Dugan and G.R., Dickens, Accumulation of natural gas hydrates in marine sediments, *5th International Workshop on Methane Hydrate Research and Development, Edinburgh, Scotland, United Kingdom*, 2006 (oral presentation).

Bhatnagar, G., W.G., Chapman, G.R., Dickens, B., Dugan and G.J., Hirasaki, Scaling of thermodynamic and transport processes for predicting methane hydrate saturation in marine sediments worldwide, *Society of Petroleum Engineers (SPE) Annual Technical Conference and Exhibition, San Antonio, Texas, USA*, 24-27 September 2006, (oral presentation); Awarded 1st prize in the regional and international student paper contests.

Bhatnagar G., G.J., Hirasaki, W.G., Chapman, B., Dugan and G.R., Dickens, Quantifying methane hydrate saturation in different geologic settings*, American Geophysical Union (AGU) Fall Meeting, San Francisco, California, USA,* December 2006, (oral presentation); Awarded outstanding student paper.

Bhatnagar G., G.J., Hirasaki, W.G., Chapman, B., Dugan and G.R., Dickens, Quantifying methane hydrate saturation in worldwide marine sediments, *Science and Technology Issues in Methane Hydrate R&D, Kauai, Hawaii*, *USA*, 2007 (oral presentation).

Bhatnagar G., W.G., Chapman, G.R., Dickens, B., Dugan and G.J., Hirasaki, Gas hydrate saturation in marine sediment: Basic Relationships to methane flux and depth of SMT, *American Geophysical Union (AGU) Joint Assembly meeting, Acapulco, Mexico*, May 2007 (oral presentation).

Bhatnagar G., G.J., Hirasaki, W.G., Chapman, B., Dugan and G.R., Dickens, Gas hydrate abundance: relationship to anaerobic oxidation of methane and the sulfate-methane transition, *Marine Biogeochemistry Seminar, Corvallis, Oregon*, *USA*, 2007 (oral presentation).

Bhatnagar, G., W.G., Chapman, G.J., Hirasaki, G.R., Dickens and B., Dugan Effect of overpressure on gas hydrate distribution, *6th International Conference on Gas Hydrates (ICGH 2008), Vancouver, British Columbia, Canada,* July 6-10, 2008 (poster).

Bhatnagar, G., W.G., Chapman, G.J., Hirasaki, G.R., Dickens and B., Dugan, Relating gas hydrate saturation to depth of sulfate-methane transition, *6th International Conference on Gas Hydrates (ICGH 2008), Vancouver, British Columbia, Canada,* July 6-10, 2008 (oral presentation).

Chatterjee S., G., Bhatnagar, W.G., Chapman, G.R., Dickens, B., Dugan and G.J., Hirasaki, Effect of lithologic heterogeneities on gas hydrate distribution, *American Geophysical Union (AGU) Fall meeting, San Francisco, California*, *USA*, December 2008 (poster).

Chatterjee S., G., Bhatnagar, W.G., Chapman, G.R., Dickens, B., Dugan and G.J., Hirasaki, Sulfate, alkalinity, calcium and carbon isotope $\delta^{13}C$ profiles as an indicator of upward methane flux, *American Geophysical Union (AGU) Fall meeting, San Francisco, California*, USA, December 2009 (oral presentation).

Chatterjee S., G., Bhatnagar, W.G., Chapman, B., Dugan, G.R., Dickens and G.J., Hirasaki, Carbon cycling across SMT above marine gas hydrates systems: A numerical modeling perspective*, Department of Energy Methane Hydrate Research Meeting, Georgia Tech University, Atlanta, Georgia*, *USA*, January 25-29, 2010 (oral presentation).

Chatterjee S., G., Bhatnagar, W.G., Chapman, B., Dugan, G.R., Dickens and G.J., Hirasaki, Effect of lithologic heterogeneities on gas hydrate distribution*, Department of Energy Methane Hydrate Research Meeting, Georgia Tech University, Atlanta, Georgia*, *USA*, January 25-29, 2010 (oral presentation).

Chatterjee S., G., Bhatnagar, W.G., Chapman, B., Dugan, G.R., Dickens and G.J., Hirasaki, Pore water chemistry profiles across the sulfate-methane transition above marine gas hydrate systems, *Society of Petroleum Engineers (SPE) Gulf Coast Regional Student Paper Contest, Lubbock, Texas, USA,* April 2010 (oral presentation).

Chatterjee S., G., Bhatnagar, W.G., Chapman, B., Dugan, G.R., Dickens and G.J., Hirasaki, Sulfate-methane transition depth as a proxy for methane flux above gas hydrate systems, *Gordon Research Conference on Natural Gas Hydrate Systems, Waterville, Maine, USA*, June 6-11, 2010 (poster).

Chatterjee S., G., Gu, G., Bhatnagar, W.G., Chapman, G.R., Dickens, B., Dugan and G.J., Hirasaki, Focused fluid flow and gas hydrate distribution in heterogeneous marine sediments, *American Geophysical Union (AGU) Fall meeting, San Francisco, California*, *USA,* December 2010 (oral presentation).

Chatterjee S., G., Bhatnagar, W.G., Chapman, B., Dugan, G.R., Dickens and G.J., Hirasaki, Effects of heterogeneous lithology and focused fluid flow on gas hydrate distribution in marine sediments, *Society of Petroleum Engineers (SPE) Gulf Coast Regional Student Paper Contest, Texas A&M University, College Station, Texas, USA,* April 2011 (oral presentation); Awarded 2nd prize in Ph.D. division.

Chatterjee S., G., Bhatnagar, W.G., Chapman, G.R., Dickens, B., Dugan and G.J., Hirasaki, Lithologic heterogeneity, focused fluid flow and gas hydrate distribution in marine sediments, *Offshore Technology Conference (OTC) University R&D Showcase, Houston, Texas, USA*, May 2011 (poster).

Chatterjee S., G., Bhatnagar, W.G., Chapman, G.R., Dickens, B., Dugan and G.J., Hirasaki, Lithologic heterogeneity, focused fluid flow and gas hydrate distribution in marine sediments, *Society of Petroleum Engineers Gulf Coast Section Emerging Engineers Conference (EEC), Houston, Texas*, *USA,* June 2011 (poster); Awarded best poster.

Chatterjee S., G., Gu, G., Bhatnagar, W.G., Chapman, B., Dugan, G.R., Dickens and G.J., Hirasaki, Effects of heterogeneous lithology and focused fluid flow on gas hydrate distribution in marine sediments, *7th International Conference on Gas Hydrates (ICGH 2011), Edinburgh, Scotland, United Kingdom*, July 17-21, 2011 (oral presentation).

Dugan B., H., Daigle, S., Chatterjee, G., Gu and G.J., Hirasaki, Continuum models of large-scale phenomena associated with hydrate-bearing sediments, *Gordon Research Conference on Natural Gas Hydrate Systems, Waterville, Maine*, *USA,* June 6-11, 2010 (oral presentation).

Dugan B., S., Chatterjee, H., Daigle, G., Bhatnagar, G., Gu, G.R., Dickens, G.J., Hirasaki and W.G., Chapman, Effects of flow focusing and geologic structures on gas hydrate saturation and distribution, *Geological Society of America (GSA) Annual Meeting, Minneapolis, Minnesota*, *USA,* October 2011 (oral presentation).

Gu G., P., Jaiswal, W.G., Chapman, C., Zelt and G.J., Hirasaki, Compositional effect on hydrate/free gas transition and BSR, *American Geophysical Union (AGU) Fall Meeting, San Francisco, California, USA, December,* 2008 (poster).

Gu G., P., Jaiswal, W.G., Chapman and G.J., Hirasaki, Effect of Hydrocarbon Components on Hydrate/Gas Distribution and BSR, *Society of Petroleum Engineers (SPE) Gulf Coast Section Regional Student Paper Cont*est, *Houston, Texas*, USA, April 17-18, 2009, (oral presentation).

Gu G., P., Jaiswal, W.G., Chapman and G.J., Hirasaki, Effect of Hydrocarbon Components on Hydrate/Gas Distribution and BSR, *Department of Energy Methane Hydrate Research Meeting, Georgia Tech University, Atlanta, Georgia*, *USA*, January 25-29, 2010 (oral presentation).

Gu G., S., Chatterjee, G.J., Hirasaki, W.G., Chapman, B., Dugan, G., Bhatnagar, C., Zelt, G.R., Dickens and P., Jaiswal, 2-D simulation on hydrate accumulation in different heterogeneous lithology structures, *Gordon Research Conference on Natural Gas Hydrate Systems, Waterville, Maine*, *USA*, June 6-11, 2010 (poster).

Task 7: Analysis of Production Strategy

Phirani, J., Pitchumani, R., & Mohanty, K. K., "Transport Properties of Hydrate Bearing Formations from Pore-Scale Modeling," SPE 124882, presented at the SPE ATCE, New Orleans, LA, Oct. 4-7, 2009.

Phirani, J., Pitchumani, R., & Mohanty, K. K., "History Matching of Hydrate Formation and Dissociation Experiments in Porous Media," SPE 118900, Proceedings of the SPE Reservoir Simulation Symposium, Woodlands, TX, February 2-4, 2009.

Phirani, J. & Mohanty, K. K., "Kinetic Simulation of CO2 Flooding of Methane Hydrates," SPE 134178, Proceedings of SPE ATCE, Florence, Italy, September 19-22, 2010.

Phirani, J. & Mohanty, K. K., "Production Strategy for Marine Hydrate Reservoirs," 7th International Conference on Gas Hydrates, Edinburgh, UK, July 17-21, 2011.

Task 8: Seafloor and Borehole Stability

Daigle, H., Bangs, N., Dugan, B., 2011, Transient pressures, hydraulic fracturing, and gas migration at southern Hydrate Ridge: Geophysical observations and flow modeling, 7th International Conference on Gas Hydrates, Edinburgh, Scotland (18 July 2011).

Daigle, H., Dugan, B., 2010, Free gas in the regional hydrate stability zone: Implications for hydrate distribution and fracturing behavior, American Geophysical Union Fall Meeting, San Francisco, CA (17 December 2010).

Daigle, H., 2010, Poromechanical feedbacks in methane hydrate systems: Insights from 1-D models, Seminar for Juanes Research Group, Department of Civil and Environmental Engineering, Massachusetts Institute of Technology, Cambridge, MA (1 October 2010).

Daigle, H., Dugan, B., 2010, Lithologically partitioned hydrates in advective systems, Gordon Research Conference on Natural Gas Hydrates, Waterville, ME (9 June 2010).

Daigle, H., Dugan, B., 2010, Origins of fracture-hosted methane hydrates, Chevron technical talk, Houston, TX (11 March 2010).

Daigle, H., Dugan, B., 2010, Fracture genesis and fracture filling in methane hydrate systems, DOE/NETL Methane Hydrate Workshop, Atlanta, GA (26 January 2010).

Daigle, H., Dugan, B., 2009, Fracture genesis and fracture filling in methane hydrate systems, American Geophysical Union Fall Meeting, San Francisco, CA (17 December 2009).

Daigle, H., Dugan, B., 2009, Fracture genesis in methane hydrate systems, Rice University Department of Earth Science seminar, Houston, TX (17 November 2009).

Daigle, H., Dugan, B., 2009, Extending NMR data for permeability estimation in fine-grained sediments, Society of Petrophysicists and Well Log Analysts 50th Annual Logging Symposium, The Woodlands, TX (23 June 2009).

Daigle, H., Dugan, B., 2008, Extending nuclear magnetic resonance data for permeability estimation in fine-grained sediments, American Geophysical Union Fall Meeting, San Francisco, CA (18 December 2008).

Dugan, B., 2011, A Review of Overpressure, Flow Focusing, and Slope Failure, 5th International Symposium on Submarine Mass Movements and Their Consequences, Kyoto, Japan (24-26 October 2011).

Dugan, B., 2010, Continuum Models of Large-Scale Phenomena Associated with Hydrate-Bearing Sediments, Gordon Research Conference: Natural Gas Hydrate Systems, Waterville, ME (6-11 June 2010).

Dugan, B., 2010, Physical properties studies: flow, fractures, and failures, DOE/NETL Methane Hydrate Workshop, Atlanta, GA (26 January 2010).

Dugan, B., 2008, Geologic Accumulation of Hydrates in Marine Sediments, Lunch and Learn Seminar at Shell International Exploration and Production Inc. (July 2008).

Dugan, B., 2007, Detection and Production of Methane Hydrate – Task 8: Seafloor and Borehole Stability, DOE-NETL Gas Hydrate Merit Review, Golden, CO (September, 2007).

Dugan, B. and ODP Leg 174A and IODP Expedition 308 Scientists, 2008, ODP/IODP Geohazard Drilling on Passive Margins, IODP Geohazards Workshop, Portland, OR (August 2007).

Dugan, B., 2007, Detection and Production of Methane Hydrate Phase 2 (Geomechanics and Fluid Flow Contributions), DOE Hydrates Kick-Off Meeting, Morgantown, WV (January 2007).

Hustoft, S., Dugan, B., Mienert, J., 2008, Integrated Hydrological Flow-Modeling and 3D Seismic Analysis of the Nyegga Pockmark-Field at the Mid-Norwegian Constrain Times of Methane Leakage, Subsurface Sediment Remobilization and Fluid Flow in Sedimentary Basins Conference (The Geological Society), 21-22 October 2008, London, England.

Scholz, N.A., Riedel, M., Spence, G.D., Hyndman, R.D., James, T., Naegeli, K., Dugan, B., Pohlman, J., Hamilton, T., 2011, Do dissociating gas hydrates play a role in triggering submarine slope failures? A case study from the northern Cascadia margin, 7th International Conference on Gas Hydrates, Edinburgh, Scotland (17-21 July 2011).

Scholz, N., Riedel, M., Spence, G., Dugan, B., Daigle, H., Hyndman, R.D., James, T.S., Naegeli, K., 2010. Slope failure of continental frontal ridges offshore Vancouver Island, British Columbia. 2010 Fall Meeting, American Geophysical Union, San Francisco, CA (13 December 2010).

COST PLAN / STATUS

DOE Grants R15620, RO15621, RO15622
02/19/2012

COST PLAN / STATUS							
Phase	**Phase 1**	**Phase 2**	**Phase 3**	**Phase 4**	**Deobligation**	**Phase 5**	**Project Total**
Baseline period	10/06-6/07	7/07-6/08	7/08-6/09	Totals 7/01/09-7/16/10		7/17/10 – 7/16/11	
Baseline Cost Plan Allocation							
Federal Share	$ 3,624	$320,010	$ 331,135	$ 356,049	$ (109,098)	$259,335	$ 1,161,055
Non-Federal Share	$ 1,004	$114,613	$ 107,630	$ 110,489	$ 23,415	$114,363	$ 471,514
Total Planned	$ 4,628	$434,623	$ 438,765	$ 466,538	$ (85,683)	$373,698	$ 1,632,569
Cumulative Baseline Cost	$ 4,628	$439,251	$ 878,016	$ 1,344,554	$ 1,258,871	$1,632,569	
Actual Incurred Cost							
Federal Share	$ 3,082	$295,415	$ 249,125	$ 354,098		$259,335	$ 1,161,055
Non-Federal Share	$ 1,091	$117,053	$ 96,346	$ 155,580		$143,428	$513,498
Total Incurred	$ 4,173	$412,468	$ 345,471	$ 509,678		$402,763	$1,674,553
Cumulative Costs	$ 4,173	$416,641	$ 762,112	$ 1,271,790		$1,674,553	
Variance (plan-actual)							
Federal Share	$ 542	$ 24,595	$ 82,010	$ 1,951	$ (109,098)	$0	$0
Non-Federal Share	$ (87)	$ (2,440)	$ 11,284	$ (45,091)	$ 23,415	$(29,065)	$(41,984)
Total Variance	$ 455	$ 22,155	$ 93,294	$ (43,140)	$ (85,683)	$(29,065)	$(41,984)
Cumulative Variance	$ 455	$ 22,610	$ 115,904	$ 72,764	$ (12,919)	$(41,984)	

Milestone Plan/Status

Task	Milestone: Status and Results	Date	Status
5. Carbon inputs and outputs to gas hydrate systems	5.1a Measure iodine in sediments We have measured iodine concentrations in pore waters and sediments from 4 gas hydrate systems. We are revising the models so that will include iodine.	12/07	Done (except writing)
	5.1b Constrain C_{org} inputs from iodine We have measured the content and isotopic composition of organic carbon and carbonate in sediment from cores of several gas hydrate systems. We have incorporated the results into our current model for ODP Site 1230.	10/08	Presently modeling in collaboration with Task 6; to be completed by Dec 2011
	5.2a Construct metal profiles in sediments We have measured metal contents in pore water and sediment from cores of two gas hydrate systems along the Peru Margin and in the Sea of Japan. The Sea of Japan work has been published (Snyder et al., 2007).	12/09	Presently modeling
	5.2b Modeling/integrating profiles We have incorporated the results into numerical models. We have written three articles discussing the use of the SMT as a proxy for methane loss through AOM (Dickens and Snyder, FITI, 2009; Bhatnagar et al., 2011; Chatterjee et al., 2011). We are currently working a fourth paper.	12/10	Done (and continuing to model)
	5.3. Amount of carbon in hydrate systems and its role in natural carbon cycling. The recipient shall develop a model to study the role of hydrate/free gas on global carbon cycling due to variation of factors	9/11	We have written two papers regarding this idea (Dickens, Clim. Past., 2011; Gu et al., 2011).

	including seafloor temperature and organic carbon content in geological history especially during Paleocene/Eocene Thermal Maximum (PETM).		1 paper in progress.

6. Numerical models for quantification of hydrate and free gas accumulations	6.1 Model development. The recipient shall develop finite difference models for the accumulation of gas hydrate and free gas in natural sediment sequences on geologically relevant time scales.	9/07	Done
	6.2: Conditions for existence of gas hydrate The recipient shall summarize, quantitatively, the conditions for the absence, presence, and distribution of gas hydrates and free gas in 1-D systems by expressing the conditions in terms of dimensionless groups that combine thermodynamic, biological and lithologic transformation, and transport parameters.	3/07	Done
	6.3 Compositional effect on BSR Original The recipient shall add to the numerical model, developed under this task, multi-hydrocarbon capability specifically to investigate how existence of multi-hydrocarbon components might affect Bottom Simulating Reflectors (BSRs). Revised The recipient shall present results via numerical tools, developed under this task, on multi-hydrocarbon existence, specifically to investigate how multi-hydrocarbon existence might affect Bottom Simulating Reflectors (BSRs).	7/07 (new: 6/11)	Simple case done; Manuscript to be submitted soon
	6.4: Amplitude Attenuation features due to hydrate/free gas distribution. Original The recipient shall simulate preferential	Simulation of the original hypothe	Original hypothesis seems inappropriate, so will write a technical report, but give up peer-review papers on this

	formation of gas hydrate in coarse-grained, porous sediment in 2-D by linking fluid flux to the permeability distribution. Revised The recipient shall simulate amplitude attenuation features such as gas chimney structure. This subtask will be up to the progress in Subtask 6.7.	sis is finished . 9/11	task. The technical report on original hypothesis is ready to submit.
	6.5: Processes leading to overpressure The recipient shall quantify, by simulation and summarize by combination of responsible dimensionless groups, the conditions leading to overpressure to the point of sediment failure.	3/08 (new: 6/11)	1D written and published; 2D near completion and need to write results (Collaborating with task 8)
	6.6 Concentrated hydrate and free gas The recipient shall, using 2-D models, simulate lateral migration and concentration of gas hydrate and free gas in structural and stratigraphic traps.	3/08 (new: 3/12)	2 manuscripts published (*Daigle et al*. JGR 2010; *Chatterjee et al.,* ICGH 2011)
	6.7 Focused free gas, heat and salinity Revised The recipient shall quantify, using 1-D and 2-D model simulations and comparisons to available observations, the factors controlling the process of localized upward migration of free gas along faults and lateral transfer to dipping strata that can lead to possible accumulations of concentrated hydrate and structures such as gas chimney. Original The recipient shall quantify, using 1-D and 2-D model simulations and comparisons to available observations, the factors controlling the process of localized upward migration of free gas along faults and lateral transfer to dipping strata that can lead to chaotic zones and possible accumulations of concentrated hydrate.	9/09 (new: 3/12)	2 manuscripts published (*Daigle et al*., GRL 2010; *Daigle et al*., G^3 2011) 2D salinity model to be completed by 12/2011; to be published by 3/12; (*Chatterjee et al*., 2012)
	6.8a Sulfate profile as indicator of methane flux	7/07	Done, and published

	The recipient shall compute, for systems where data on the sulfate profile is available, the oxidation of methane by sulfate and shall indicate the perceived level of effect on gas hydrate accumulation and the data's value as an indicator of methane flux.		
	6.8b Carbon cycling across SMT above marine gas hydrate systems. The recipient shall compute, for systems where data on the sulfate, bicarbonate (DIC), calcium, carbon isotope profiles are available, the reduction of sulfate by methane and by particulate organic carbon and shall indicate the perceived level of effect on gas hydrate accumulation and the depth to the SMT as an indicator of methane flux.	6/10	Done, and published (*Chatterjee et al.*, JGR 2011) 1 manuscript in preparation (*Chatterjee et al.*, 2011)
	6.9 Application of models to interpretation of case studies. The models developed in Task 6 will be applied to case studies in the interpretation of each of the other tasks.	6/11 (new 9/11)	Started and working 2D system, manuscripts should be submitted by 03/12
7. Analysis of production strategy	7.1a Pore scale model development and Hydrate code comparison For this milestone, we will develop pore-scale models of hydrate accumulation by simulation. Our hydrate code will be used to solve a set of problems formulated by the Code Comparison Study group. Our results will be compared with those of other hydrate codes.	1/08	6/08 Code comparison is 100% complete
	7.1b Petrophysical and thermophysical properties of hydrate sediments from pore-scale model For this milestone, we will assume the pore-scale models of hydrate accumulation developed in the last milestone and estimate transport properties as a function of hydrate and gas saturations.	1/09	6/09 This task is complete

	7.2a Modeling of several production strategies to recover gas from marine hydrates Several production strategies would be modeled using the transport property correlations developed in the previous milestone. Optimal strategies will be identified.	6/10	12/11 This task is complete. We evaluated 1. Depressurization vs. warm water injection 2. Vertical wells vs. horizontal wells 3. Position of injection and production wells. We found that in unconfined reservoir, depressurization does not work; warm water injection is needed. Horizontal wells were more effective than vertical wells. Injection wells placed close to bottom aquifers and production wells close to the top of the hydrate deposit were effective.
	7.2b Effect of marine reservoir heterogeneities on production of methane Reservoir heterogeneity anticipated in marine environments (known or determined through other tasks) would be incorporated. Appropriate hydrate distributions, either constrained from experimental data or mechanistic simulations (Task 5) would be used. Sensitivity of gas production to the heterogeneities would be calculated.	6/11	Completed
8. Seafloor and borehole stability	8.1a Collection of data We have collected the published data and are working it into a data base. We are also working on a review paper summarizing the state of the art settings. This will include laboratory experiments, field data, published results, and unpublished data.	05/08	Completed

	8.1c Complete database We are organizing the data from task 8.1a into a format that can be searched and used by researchers trying to understand mechanical behavior of hydrate-bearing sediment. We will also identify key gaps in the database for focusing future hydrate research endeavors. We have started exchanging these data with the modeling components of this project.	6/10	Done
	8.2a Link database with models We have started passing data along to the modeling groups so they can use sediment properties from hydrate provinces as they simulate hydrate accumulation and production.	9/11	Completed 12/11.
	8.2b Add sediment stability to models Standard stability calculations have been implemented in a standard basin model. Now that it is functional we will work with the hydrate accumulation model to add a stability calculation to the 2-D models.	6/10	Done 12/11
	8.2c Conditions for (in)stability After implementing the stability model in the hydrate accumulation code, we can explore the conditions (e.g., hydrate dissociation, sea-level fall) that could drive slope failure and hydrate/methane release or lead to borehole failures during production.	9/11	Completed 12/11
9 Geophysical imaging of hydrate and free gas	9.1 Preliminary processing and inversion of seismic data. Perform conventional seismic reflection processing, velocity analysis, travel time tomography, and other analyses as deemed appropriate and necessary.	08/08 – 08/09	Completed
	9.2: Final 1-D elastic and 2-D acoustic waveform inversion.	08/09 – 08/10	Completed

	Apply 1-D elastic and 2D acoustic inversions on data obtained from subtask 9.1 to derive determine high-resolution elastic and acoustic properties.		
	9.3: Rock physics modeling. Apply rock physics models to the developed seismic models to estimate hydrate saturation and lithology through application of well log data in conjunction with data from subtask 9.2. For this subtask we shall seek to collaborate with research being conducted under separately funded DOE-NETL projects (DE-FC26-05NT42663 with Stanford University, "Seismic-Scale Rock Physics of Methane Hydrate" and others as applicable).	08/10 – 08/11	Completed

National Energy Technology Laboratory

626 Cochrans Mill Road
P.O. Box 10940
Pittsburgh, PA 15236-0940

3610 Collins Ferry Road
P.O. Box 880
Morgantown, WV 26507-0880

One West Third Street, Suite 1400
Tulsa, OK 74103-3519

1450 Queen Avenue SW
Albany, OR 97321-2198

539 Duckering Bldg./UAF Campus
P.O. Box 750172
Fairbanks, AK 99775-0172

Visit the NETL website at:
www.netl.doe.gov

Customer Service:
1-800-553-7681